Streambed Instabilities and Nature of Turbulence around Bridge Piers in a Dredged Channel

A Thesis Submitted

In partial fulfillment of the requirement for the degree of

Doctor of Philosophy

Submitted by

Abhijit Dilip Lade

(176104013)

DEPARTMENT OF CIVIL ENGINEERING

INDIAN INSTITUTE OF TECHNOLOGY GUWAHATI

GUWAHATI – 781039, ASSAM, INDIA

June, 2020

Declaration

I, Abhijit Dilip Lade, declare that this thesis, "Streambed Instabilities and Nature of Turbulence around Bridge Piers in a Dredged Channel" and the work presented in it is my own. I confirm that:

- The work contained in this thesis is original and has been done by myself and under the general supervision of my supervisor.
- The work reported herein has not been submitted to any other Institute for any degree or diploma.
- Wherever I reported material from other sources, I have duly cited and acknowledged their respective authors and sources.
- I also affirm that no part of the thesis is plagiarized to the best of my knowledge.
- I take complete responsibility for the results and inferences reported in the thesis.

Date: Abhijit Dilip Lade

Department of Civil Engineering
Indian Institute of Technology Guwahati
Guwahati – 781039, Assam, India.

Dr. Bimlesh Kumar
Professor
0361-2582420
bimk@iitg.ernet.in

CERTIFICATE

This is to certify that this thesis entitled "Streambed Instabilities and Nature of Turbulence around Bridge Piers in a Dredged Channel" submitted by Abhijit Dilip Lade, in partial fulfillment of the requirements for the award of the degree of Doctor of Philosophy, to the Indian Institute of Technology Guwahati, Assam, India, is a record of the bonafide research work carried out by her under my guidance and supervision at the Department of Civil Engineering, Indian Institute of Technology Guwahati, Assam, India. To the best of my knowledge, no part of the work reported in this thesis has been presented for the award of any degree at any other institution.

Date:

Place: IIT Guwahati

(Dr. Bimlesh Kumar)

Publications

JOURNALS

- Abhijit D. Lade and Bimlesh Kumar, "Streambed instabilities around a bridge pier in a dredged channel." **River Research and Applications**, 2020.
- Abhijit D. Lade, Vishal Deshpande, and Bimlesh Kumar, "Study of flow turbulence around a circular bridge pier in sand-mined stream channel." **Proceedings of the Institution of Civil Engineers - Water Management**, 1900041, 2019.
- Abhijit D. Lade, Anja Mihailović, Dragutin T. Mihailović, and Bimlesh Kumar, "Randomness in flow turbulence around a bridge pier in a sand mined channel." **Physica A: Statistical Mechanics and its Applications**, 535, 122426, 2019.
- Abhijit D. Lade, Vishal Deshpande, and Bimlesh Kumar, and Giuseppe Oliveto, "On the morphodynamic alterations around bridge piers under the influence of instream mining." **Water**, 11(8), 1676, 2019.
- Abhijit D. Lade, Jyotirmoy Barman, and Bimlesh Kumar, "High-order moments of streamwise velocity fluctuations around a cylinder in dredged mobile bed channel." Water Management (Under Review)

CONFERENCES

- Abhijit D. Lade and Bimlesh Kumar, "Can close proximity mining activities compromise the stability of bridge piers." **24th Hydro 2019 International Conference (Hydraulics, Water Resources and Coastal Engineering)**, Osmania University, Hyderabad, India, December 18-20, 2019.
- Abhijit D. Lade, Jyotismita Taye, and Bimlesh Kumar, "Influence of mining activities on the hydromorphology around bridge piers." **24th Hydro 2019 International Conference (Hydraulics, Water Resources and Coastal Engineering)**, Osmania University, Hyderabad, India, December 18-20, 2019.

- Abhijit D. Lade, Jyotismita Taye, and Bimlesh Kumar, “Effect of sand mining on the nature of turbulence around circular bridge piers.” **14th International Symposium on River Sedimentation**, Chengdu, China, September 16-19, 2019.
- Abhijit D. Lade, Jyotismita Taye, and Bimlesh Kumar, “A critical review of the physical effects of sand mining on hydraulic structures.” **6th National Conference on Coastal, Harbour and Ocean Engineering**, CWPRS, Pune, India, September 26-28, 2018.

Acknowledgements

The journey of my thesis was definitely a unique learning experience, and it would not have been possible without the support and contribution of several people.

First and foremost, I am thankful to my supervisor Dr. Bimlesh Kumar, for giving me the opportunity to work with him and his relentless support and commitment. He is an exceptional human being and was always there to guide. He is a mentor in a true sense, and I look up to him in many ways. He imbibed that research is a never ending process, and I will continue to work with him in the future.

I express my sincere thanks to the members of my doctoral committee: Dr. Suresh Kartha (Chairman), Dr. Rishikesh Bharti, and Dr. Vanayak Kulkarni for their insightful comments, encouragement, and valuable time through this research. I am thankful to the Department of Civil Engineering, IIT Guwahati, for providing me the required resources and a fruitful work environment.

I also thank Dr. Bandita Barman, Dr. Vishal Deshpande, Dr. Rutuja Chavan, and Dr. Anurag Sharma for their valuable inputs. Working with Jyotismita and Jyotirmoy at the laboratory was surely an experience I will cherish. I am also grateful to Bazal Da for extending his relentless support in the laboratory.

I would take this opportunity to acknowledge the support and hard work of my parents. I thank all my family members for their support. I especially want to thank my wife, Rashmi, for encouraging me throughout this journey. I admire her selfless efforts, patience, and it would not have been possible without her support. I also thank my brother Anurag and all my friends Abhinav, Debashish, Swarup, Parag, Sumit, Aditya, Rishabh, Chetan, Abhishek, Apoorva, and Paramita for being alongside me in this journey.

Abstract

Extraction of sand from streambed has catastrophic repercussions on aquatic animalia habitat, surface water quality, and environment. Sand mining in an active alluvial channel can compromise the streambed stability of the hydraulic structures nearby. The complex nature of flow approaching and interacting with the bridge piers after passing over a mining pit and the streambed response around the piers is not fully understood. Gravity flow experiments were performed in a sand bed channel to investigate the effects of a mining pit on the hydromorphology around bridge piers.

Significant alterations in the nature of turbulence around a circular pier, oblong pier, and two circular piers in tandem were observed in a sand mined channel. Mean velocity profiles, Reynolds stresses, kinetic energy fluxes, and turbulence scales were analyzed at critical locations along the channel bed as well as in the proximity of the pier. At the approach location where flow had passed over the pit and was approaching the pier, substantial increments in the near-bed velocities, bed shear stress, and Reynolds stresses were observed. Dredging of the pit increased the strength of the horseshoe vortex in the scour hole region, and amplification of the instantaneous bed shear beneath the turbulent horseshoe vortex zone was observed as compared to no-pit case. Pit excavation also amplified the shedding frequency of trailing vortices at the rear of the pier.

These effects were instrumental in the alteration of local scour as well as erosion and deposition patterns around bridge piers. Severe transverse erosion at the pier base, as well as lowering of channel bed upstream of the pier was observed because of channel dredging. Streambed instability was a function of the distance between the pit and pier, as well as flow Reynolds number. Streambed instability was analyzed based on two non-dimensional parameters, namely, pier exposure factor and normalized upstream incision depth. The maximum values of both these parameters were observed when the mining pit was dredged closest to the pier. We also observed growth in streambed instability with an increase in flow Reynolds number.

Contents

List of Figures

List of Tables

Notations

d_{50}	Median particle size
σ_g	Geometric standard deviation
d	Pier diameter
Re	Reynolds number
Fr	Froude number
R^*	Shear Reynolds number
L_u	Adjustment length beyond which flow uniformity is attained
h	Flow depth
u, v, w	Instantaneous velocities in the streamwise (X), lateral (Y), and vertical (Z) directions
u', v', w'	Velocity fluctuations in the streamwise (X), lateral (Y), and vertical (Z) directions
$\bar{u}, \bar{v}, \bar{w}$	Average velocities in the streamwise (X), lateral (Y), and vertical (Z) directions
Q	Flow discharge
u_*	Shear velocity
κ	Von karman constant
Δz	Depth of the virtual bed level,
z_0	Depth of zero velocity level
τ_0	Average bed shear stress
τ_c	Critical bed shear stress
τ_b	Instantaneous bed shear stress
ρ	Mass density of water
$-\rho\overline{u'w'}$	Reynolds shear stress in streamwise direction
$-\rho\overline{v'w'}$	Reynolds shear stress in lateral direction
σ_u	Streamwise turbulence intensity
σ_w	Vertical turbulence intensity
F_{TKE_u}	Streamwise flux of the turbulent kinetic energy

F_{TKE_w}	Vertical flux of the turbulent kinetic energy
H	Hyperbolic hole size
$\lambda_{i,H}$	Detection function
T	Time period of velocity time series
$S_{i,H}$	Fractional contribution to Reynolds shear stress
$P_{i,H}$	Occurrence probability
K	Turbulent kinetic energy
ν_T	Turbulent viscosity
l	Mixing length
λ_T	Taylor micro-scale
ν	Kinematic viscosity of water
ε	Turbulent kinetic energy dissipation rate
S_{uu}	Spectral density function
k_w	Wave number
E_T	Eulerian time scale
E_L	Eulerian length scale
$R(t)$	Autocorrelation function
S_t	Strouhal number
ω	Frequency of vortex shedding
L_{ch}	Characteristic dimension
L	Distance between pit and the pier
δ	Boundary layer thickness
$\langle(u'^{+})^{2p}\rangle^{\frac{1}{p}}$	Higher-order moments of velocity fluctuations
$(u'^{+})^{2p}P(u'^{+})$	Pre-multiplied probability density functions
E	Exposure Factor
d_{sc}	Maximum frontal scour depth
d_{inc}	Incision depth at the pier upstream
$\psi_{a,b}$	Wavelet function
V_c	Speed of spatial evolution of the scour

Chapter **1**

Introduction

1.1 Background

The direct mechanical removal of sand from rivers and streams (or riverbed mining) has become a sizeable source of coarse and fine aggregates in most parts of the world. Aggregates extracted from rivers are beneficial for any construction use as they are granulated and clean and can be extracted easily (Kondolf, 1994). Aggregates found in rivers are actually sediments carried by the river, which are deposited on floodplains and riverbeds as bed loads. In the case of an incising river reach, sediment mining always has an adverse impact since it induces erosion to the bed and banks of the river. In the case of an aggrading river reach, controlled sediment mining from the riverbed and its floodplain is good practice for maintaining flood capacity and channel stability. However, because of ineffective regulatory control and the commercialization of sediments, large-scale uncontrolled and unplanned sediment mining from rivers is now a major cause of concern.

Currently, the annual extraction of sand and gravel, which is around 32-50 billion tones, has even surpassed fossil fuel (Torres et al., 2017) since 2010. Owing to the ever-increasing demand and severe imbalance between the demand and supply, illegal dredging of rivers is a common sight in almost 70 countries, including India, China, Cambodia, Vietnam, Kenya, etc. (Bendixen et al., 2019).

Channel dredging significantly alters the hydro-morphology of the fluvial system in the form of enhanced sediment carrying capacity in downstream, channel bed lowering, bank erosion, etc. A mining pit excavated in an alluvial channel has the potential to alter the turbulence around bridge piers, which consequently affects the streambed stability around the piers. In this chapter, various aspects of river mining, such as types of mining and their effects on the fluvial system, etc. are discussed.

1.2 Types of Alluvial Channel Mining

Sand and gravels are extracted from an active channel in three ways, namely dry pit mining, wet pit mining, and bar skimming (Kondolf, 1994; Langer, 2003), as shown in Figures 1.1 and 1.2.

- Wet-pit mining: In the case of wet-pit mining, the sand and gravels are excavated below the water table or directly from a perennial stream itself, using mechanized excavators and draglines.
- Dry-pit mining: It involves mechanized dredging dry ephemeral channel beds using excavators and bulldozers etc. The headcuts from dry pits are likely to propagate in the upstream direction.
- Bar-skimming: The top layer of sand and gravel bar deposits is scrapped of without dredging below the summer water level. The thickness of the top layer, which is scrapped, may vary. This method generally requires the surface irregularities be smoothed out and that the extracted material be limited to what could be taken above an imaginary line sloping upwards and away from the water from a specified level above the river's water surface at the time of extraction (typically 0.3 - 0.6 m).

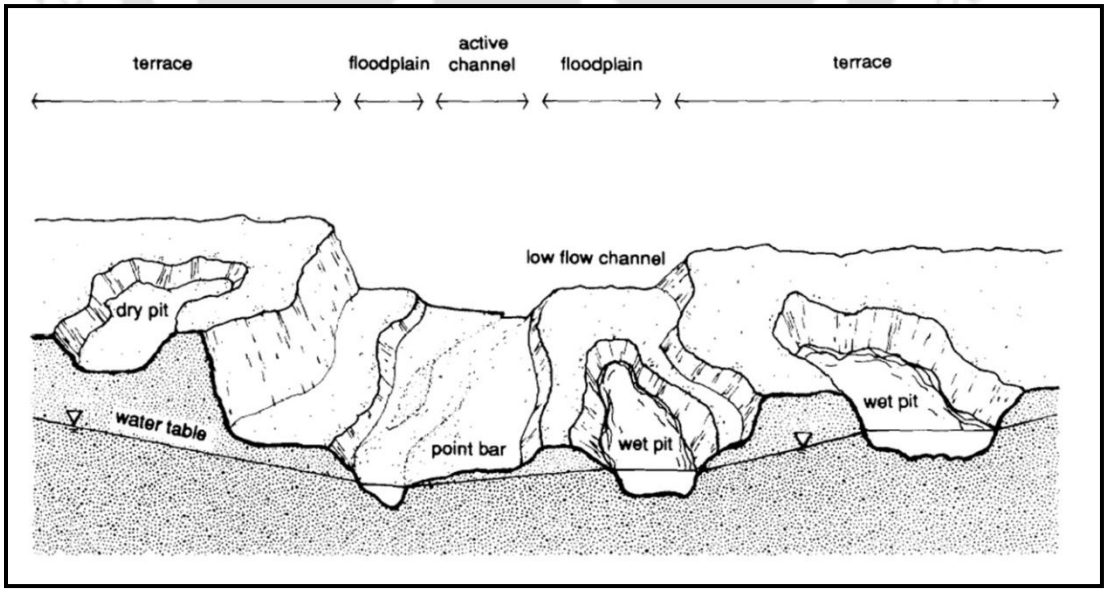

Figure 1.1 Various types of mining in alluvial channel relation to river channel morphology and alluvial water table (Kondolf, 1994).

Figure 1.2 (a) Wet-pit mining in Sungai Kulim, Penang, Malaysia (Langer, 2003) (b) Dry-pit mining in Bhramaputra River near Saraighat bridge, Guwahati, Assam, India (photographed by the author, 2018) (c) Bar-skimming in Sungai Kulim, Penang, Malaysia (Langer, 2003).

1.3 Effects of Channel Mining Activities

Sediment mining produces a large variety of physical, ecological, and environmental effects. Excavation of the mining pit in a river bed affects the flow characteristics and disrupts the sediment flow continuity of the river (Collins & Dunne, 1989; Kondolf, 1994; Rinaldi et al., 2005). The effects of mining operations are summarized in Table 1.1.

1.3.1 Morphological impacts on fluvial system

River systems are dynamic in nature and can be classified into three zones: rugged headwaters characterized by erosion and sediment production, a middle zone of sediment transport, and a downstream zone of sediment deposition below sea level. The bedload transport rate varies spatially and temporally in a fluvial system as it depends upon the

supply from the catchment and transmitting power of the river. When the transport rate is altered, river morphology adjusts accordingly. Mining in an active channel of the river system alters the equilibrium of the streambed, which results in bed erosion. A mining pit acts as a trap to the sediments carried by the flow initially, and a knickpoint is created. As the water deposits the sediments in the pit, the downstream flow has the capacity to carry sediments but don't have sediments. Therefore, the flow erodes the downstream of the pit and causes incision. The knickpoint also migrates in the upstream direction and causes erosion in upstream of the pit. This process is called as headcutting of knickpoint migration, and it can translate many kilometers upstream, as shown in Figure 1.3 (Collins & Dunne, 1989; Kondolf, 1994).

The actual channel dredging operations involve enlargement or the widening of the channel. This can change the stream width, gradient, and depth of the channel, Deepening of the channel leads to bank instabilities and can cause bank erosion (Kondolf, 1994; Rinaldi et al., 2005; Wishart et al., 2008). The widening and deepening of stream channels alter the flow pattern and velocities of the stream (Crunkilton, 1982). Channel dredging primarily affects velocities in two ways. Due to the steep gradient, the velocities sharply increase while entering the dredged zones. After entering the mining pit, velocities are reduced as the cross-sectional area is greater. Bedload transport and suspended sediments will increase on account of the bank erosion caused by dredging operations. Channel bed is lowered, and bed slope increases in the upstream of the mining zone. In-stream mining can also affect the channel pattern in some cases. Surian & Rinaldi (2003) observed changes in channel pattern from breaded to wandering in a few Italian rivers. The morphological adjustments which occur on account of channel mining activities are incredibly rapid immediately after the mining activities and become asymptotic in the later stages on a temporal scale. The predominant adjustment in morphology in the form of channel narrowing is shown by braided rivers, while adjusted mainly through bed-level lowering (Surian & Rinaldi, 2003).

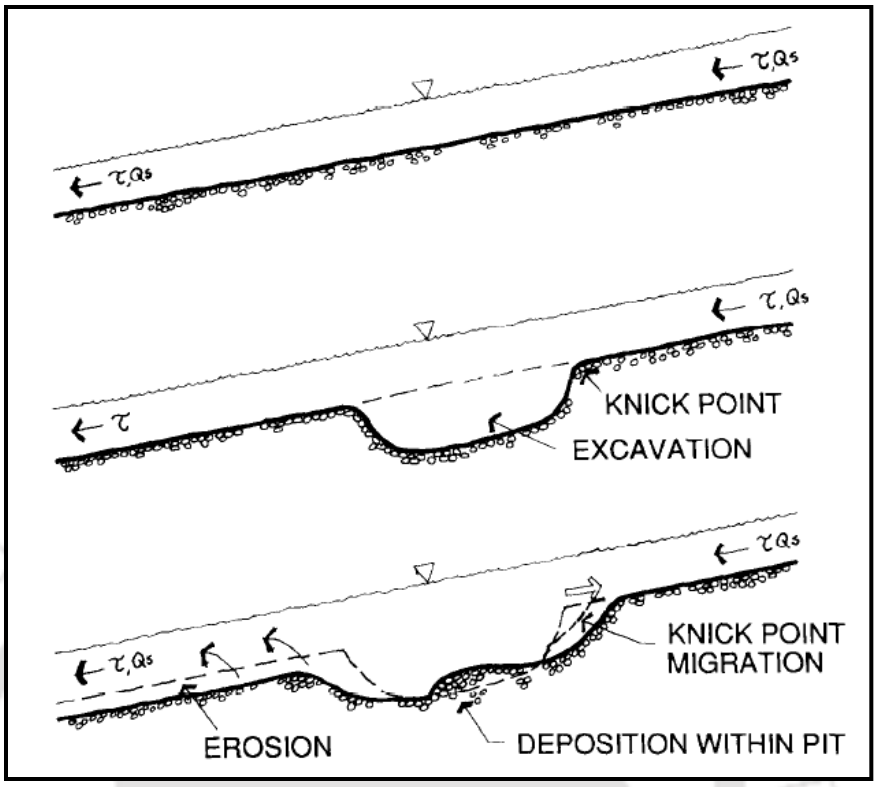

Figure 1.3 Incision produced by instream gravel mining. (a) The initial, pre-extraction condition, in which the river's sediment load (Qs) and the force available to transport sediment, the shear stress (τ), are continuous through the reach. (b) The excavation creates a knickpoint on its upstream end and traps sediment, interrupting the transport of sediment through the reach. Downstream, the river still has the capacity to transport sediment (τ) but has no sediment load. (c) The knickpoint migrates upstream and hungry water erodes the bed downstream, causing incision upstream and downstream (Kondolf, 1994).

1.3.2 Ecological, environmental, and water quality impacts

When the floodplain aquifer discharges into a stream, groundwater levels can be lowered as a result of channel degradation. Lowering of the water table would reduce aquifer storage capacity. Studies conducted at Narnaul Block, which is a part of Mahendergarh district in southwestern Haryana, the groundwater table is dropping at a rate of 1.0 m/year. The average depth of the water table in Narnaul Block has declined from 18.4 m in 1975 to 55.2 m in 2009 (Tejpal et al., 2014). In case the river is recharging the

groundwater, excessive mining will reduce the thickness of the natural filter materials (sediments) through which the groundwater is recharged. The pollutants due to mining, such as the washing of mining materials, wastes disposal, diesel, and vehicular oil lubricants, and other human activities, may pollute the groundwater. Studies conducted at Youngsan River, a river located in the south-west of the Korean Peninsula, have shown that there is a considerable rise in levels of suspended solids downstream of mining pits (Kim, 2005). Sediment deficit, caused by mining within an estuary or in the upstream river channel, can increase tidal penetration into the estuary, tidal range, and peak tidal discharges (Erskine, 1990).

Morphological alterations arising from the in-stream mining operations or floodplain mining operation can have a severe impact on key water quality parameters such as dissolved oxygen, turbidity, light, and temperature. Excavation of rivers and floodplains increase the concentration as well as discharge of suspended and dissolved solids, which increases the turbidity levels at the dredging location and in the downstream flows (Cordone & Kelley, 1961; Stern, 1978). The increase in turbidity may last for a short term on account of washing operations. However, it can also prolong for a very long period of time in the events of headcutting and bank erosion. Hamilton (1961) reported a rise of almost 3000 ppm in the turbidity levels due to gravel washing operations in the rivers of Scotland, up to 2000 m downstream. Another problem associated with mining is the resuspension of organic and inorganic matter within the river bed. The resuspension of organic matter reduces the dissolved oxygen level in the stream and affects the aquatic habitat (Cordone & Kelley, 1961; Crunkilton, 1982). The toxic materials, such as pesticides coming from the agricultural fields, may also get resuspended (Crunkilton, 1982). Rise in turbidity levels of the stream on account of mining operations has several secondary implications, such as a decrease in the penetration of sunlight. Lack of light penetration hampers the photosynthesis of aquatic plants (Crunkilton, 1982). Rivier & Seguier (1985) noted a reduction of about 50 – 70 % in the chlorophyll levels in Dore River in France due to gravel mining. Mining leads to channel modifications such as wider and shallower channels, which increases the stream temperatures (Kondolf, 1997). Other factors associated with mining operations such as removal of bank and riparian vegetation also contribute to the rise of stream temperatures. Another reason for the

temperature rise is the flow of connected ponds in the floodplain into the main stream due to mining (Kanehl & Lyons, 1992).

Plant communities are directly decreased due to channel dredging (Shields Jr & Nunnally, 1984). High turbidity levels, lower light penetration, increased suspended solids in a mining-affected channel cause reduction in the density and metabolism of plants, including algae (Rivier & Seguier, 1985). Increased deposition of sand and silt, which occurs due to the disruption of streambed can cause a reduction in macrophyte communities. A reduction of more than 50 % in the Diatom population in the River Dore, France, occurred due to gravel mining (Rivier & Seguier, 1985).

River mining activities can directly remove the invertebrates from the channel and decrease their population. Dredging activities can also reduce the invertebrate population indirectly through the destruction of habitat and sedimentation (Maurer et al., 1981; Thomas, 1985). In-stream channel dredging operations reduce both density and biomass of the invertebrates several kilometers downstream of the dredging zone (McKenzie et al., 2020; Owens et al., 2005). Rivier & Seguier (1985) observed a 62-96% reduction in invertebrate biomass in River Ouveze, France. The removal of coarse particulate organic matter will affect shredders and collectors, and likewise, the removal of detritus will affect detritivorous invertebrates. Invertebrates that inhibit woody debris either emigrate or perish due to mining. The increased stream temperatures after in-stream mining operations also affect the emergence periods of aquatic invertebrates, and this, in turn, may alter reproduction (Maurer et al., 1981). The removal of organic matter removes the food sources and diversity of substrates available to the benthic invertebrates (McKenzie et al., 2020).

River Mining leads to channel instabilities resulting in a direct loss of wildlife habitat, loss of shade, and cover to the channel (Kondolf, 1994). In-stream mining destroys in-channel alluvial features like riffles and pools important for enhancing habitats and their diversity. Bed coarsening and removal of gravel suitably sized for spawning are of particular concern on rivers supporting salmonids (salmon and trout). Moreover, dredging river shallows removes the substratum for submerged and emerged macrophytes (Turner

& Erskine, 1997). Water-table lowering can result in widespread loss of riparian vegetation, which in turn causes loss of wildlife habitats, destruction of local flora and fauna, and loss of shade and cover to the channel. The abandonment of active floodplain by incision causes a loss of wet areas and related habitats. The operation of mining can increase suspended sediment transport downstream, affecting benthic invertebrates and fish populations (Erskine, 1990; Turner & Erskine, 1997). Dredging rivers impounded by weirs can increase water depths to the extent allowing the development of persistent thermal and oxygen stratification of the water column during summertime. In-stream mining reduces the loading of coarse woody debris in the channel, which is important as cover for fish. Extraction typically results in a wider, shallower streambed, leading to increased water temperatures, modification of pool-riffle distribution, alteration of inter-gravel flow paths, and thus degradation of salmonid habitat (Kondolf, 1994).

A report published by British Geological Survey (Weeks et al., 2003) based on studies conducted on river mining in the Rio Minho and Yallahs rivers, Jamaica, suggested that the greatest change in faunal assemblage occurs in the immediate vicinity and immediately downstream of sand and gravel mining localities and that biological recovery from these activities is slow following the catastrophic removal of the streambed resulting in massive habitat loss and very low diversity of the benthic fauna. Consequently, it is anticipated that the decolonization of these disturbed habitats is slow, resulting in areas of lowered biodiversity. Environmental impact assessment (EIA) of three important rivers in the southwestern coast of India, namely the Chalakudy, Periyar, and Muvattupuzha rivers, was conducted by Sreebha & Padmalal (2011). They reported about 11 million tonnes of sand being mined every year (about 8.5 million tonnes from instream mining and sand and 2.5 million tonnes from floodplain mining) for booming residential construction and other infrastructural facilities in Kochi city. Their study pointed out sand mining and allied processing activities affect not only the river ecosystem but also degrades the biophysical environment within the floodplain area.

Table 1.1 Effects of channel mining activities

Category	Prominent effects of River mining
Morphological Effects	• Enlargement or widening of stream channels • Channel deepening which makes the river banks unstable and causes bank erosion • Alteration in flow patterns of the river • Increase in bedload transport and suspended sediments • Influence on runoff patterns, increased erosion, bank destabilization • Lowering of downstream bed levels • Progressing bed degradation upstream or headcutting • Undermining of bridge piers, pipelines etc.
Ecological, environmental and water quality impacts	• Decline in the alluvial water table • Rise in turbidity levels in mining zone and downstream reaches • Resuspension of organic material causing decrease in dissolved oxygen concentrations • Reduction in light penetration due to increased turbidity levels • Reduction in natural filter media and groundwater pollution due to mining waste • Reduction in vegetation and increased stream temperatures • Reduction in aquatic plant population such as algae, diatoms, macrophytes, etc. • Reduction in aquatic invertebrate population • Reduction in fish population (both running water and still water species)

1.4 Effect of Sand Mining on Bridge Piers

The geomorphic impacts of in-stream mining activities such as channel incision and bed-level lowering can lead to undermining of bridges and other structures such as buried pipelines. Case studies report incision as deep as 6 – 10 m at bridge piers on account of in-stream mining (Kondolf & Swanson, 1993; Kondolf, 1994, 1997). The local scour, which occurs in the first few years after the bridge construction, should be taken into account before analyzing the effect of in-stream mining. The streambed around the bridge piers remains relatively stable after the equilibrium local scour is reached, after which the effects of in-stream mining can be observed.

In-stream mining-induced channel incision caused exposure of aqueducts, gas pipelines, and other utilities buried in the streambed and also exposed the footings of a major highway bridge on the San Luis Rey River. The A7 motorway bridge collapsed in 1971 because of undercutting at the foundation on account of extensive gravel mining in the vicinity in the 1960s and 1970s (Rovira et al., 2005). Evidence of incision as deep as 3.0 m around the bridge confirmed the role of mining activities in the bridge failure. As a result of extensive in-stream gravel mining at the upstream and downstream reaches of the Highway 32 bridge over Stony Creek, California, undermining of abutments and piers was observed, as shown in Figure 1.4 (Kondolf, 1997). Erosion around municipal water intakes occurred due to mining activities in Russia (Marcus, 1992).

The average annual yield of bedload sediments from all the rivers in California is about 13 million metric tons. However, according to an estimate from the gravel extractors, the annual extraction of sand and gravels from these rivers was about 22.8 million tons. Thus, instream operators extract almost twice the sediment yield in an average year, which creates a severe imbalance in sediment equilibrium. Avila (2006) studied the streambed condition around five major bridges on the San Benito River in California. Within a few years of mining operations, a degradation of 3.0 m at Cienega Road Bridge and 5.0 m at San Juan Road Bridge was observed by Avila (2006). The channel bed-level lowering and lateral erosion of channel caused due to mining activities caused damage to almost all the bridges on the San Benito River, including exposure of pile foundations.

The failure and collapse of the Hintze Ribeiro Bridge in Portugal claimed the lives of 59 people in 2001. According to the authorities, the failure as a result of the uncontrolled illegal sand mining activities in the proximity of the bridge for over two decades (Sousa et al., 2013). Sousa et al. (2013) detected movement of the structure of the order 20 mm yr^{-1} using Multi-Temporal Interferometric techniques, prior to its collapse.

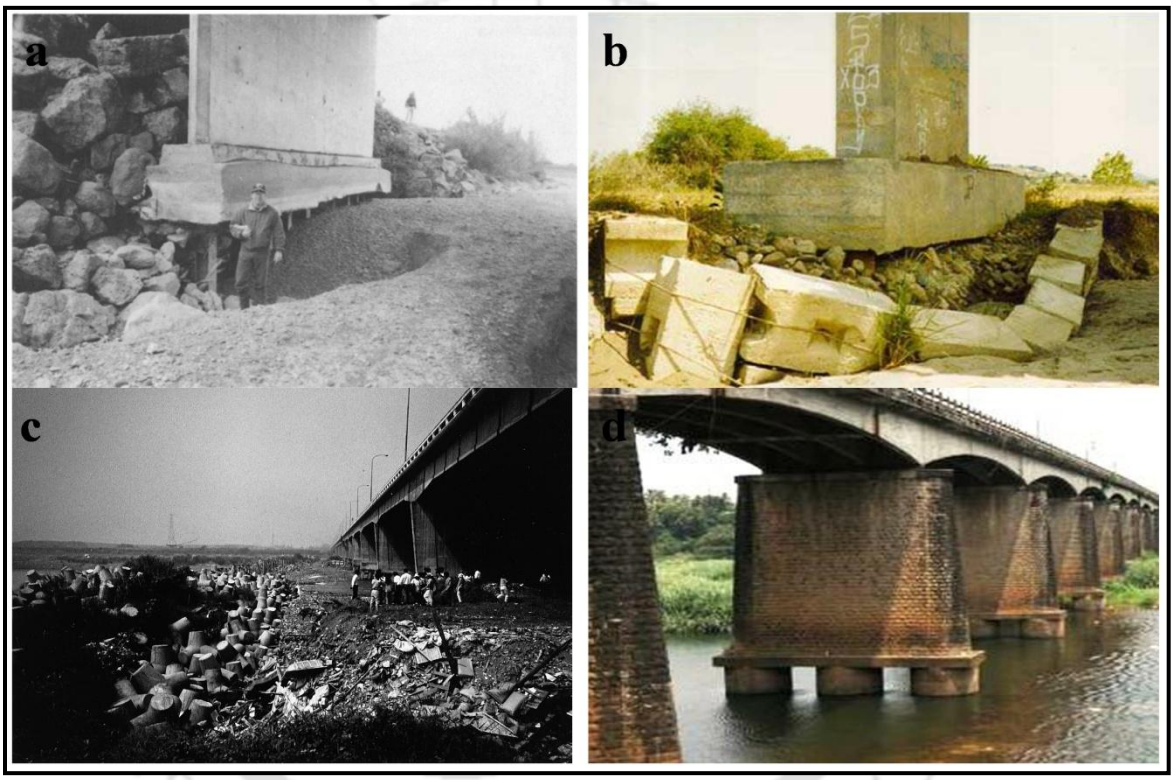

Figure 1.4 (a) Undermining of Highway 32 Bridge, over Stony creek, near Orland, California due to incision up to 5 meters (Kondolf, 1994) (b) Undermining and failure of scour protection work around pier 5 of Cienega Road Bridge (Avila, 2006) (c) Undercutting and grade control efforts along the downstream side of the Kaoping Bridge over the Kaoping River, Taiwan, to control incision caused by massive gravel mining downstream (Kondolf, 1997) (d) Exposed foundations of Periyar Bridge in Tamil Nadu, India after intensive sand mining activities in the proximity (image downloaded from https://timesofindia.indiatimes.com).

1.5 Mining Scenario in India

River Mining is the largest source of sand to meet the requirements of the rapidly booming construction industry in India. Despite the legal framework for sustainable mining practices, the industry gets most of its sand by dredging the river beds and banks without much consideration of the guidelines.

The Central Government introduced Sustainable Sand Mining Guidelines 2016 and stressed on use of technology to monitor controlled river sand mining, Stressing on reduction in consumption of sand, and focusing on alternative sources.

According to the policy on Sediment Management in India, '*Sand and gravel shall not be extracted within 200 to 500 meters from any crucial hydraulic structure such as pumping station, water intakes, and bridges. For carrying out mining in proximity to any bridge and/or embankment, appropriate safety zone should be worked out on case to case basis, taking into account the structural parameters, locational aspects, flow rate etc. and no mining should be carried out in the safety zone so worked out*' (Ministry of Environment, Forest and Climate Change, 2016). In spite of these directives in place, the contractors excavate river bed near the bridges to reduce the carriage costs.

1.6 Present State of the Art

Presently, comprehensive scientific studies on the effect of mining on scouring and flow characteristics around hydraulic structures are not documented in the literature. Some preliminary numerical and experimental studies on the stream bed instability abound bridge pier due to mining can be found. However, several experimental, numerical as well as field studies have been conducted in the last two decades on the effect of mining pit on the channel hydromorphology. A review of these studies is presented in the following section.

Collins & Dunne (1989) studied on gravel transport, gravel harvesting, and channel bed degradation in rivers draining the southern Olympic Mountains, Washington, USA. They conducted sediment mass balance analysis for the three rivers, namely Humptulips,

Wynoochee, and Satsop. They analyzed data from nine gauging stations over a period of 55 years and found river bed degradation of about 0.03m/yr. Their study confirmed that annual bedload sediment flow decreases after gavel mining activities. Based on their survey of data for three decades, they reported that the quantum of gravel mining exceeded the yearly replenishment rates for all three decades.

Collins & Dunne (1990) studied several documented cases of in-stream gravel mining in river basin across the United States and New Zealand. The authors comprehensively complied the aspects of gravel mining, such as the geomorphic effects and general management approach to mining in the river basin. They documented several effects of in-stream gravel mining such as bed degradation due to the lack of sediments from the upstream, undermining of bridge supports and pipelines, depletion of gravel bed and exposure of substrate bedrock, rapid bank erosion, and increase in flood conveyance capacity. The geomorphologic alterations could extend several kilometers from the site of mining operations. According to the authors, a thorough understanding of key aspects of river basin is necessary for accurate prediction of the effects of gravel mining. These aspects include the mechanism of sediment transport and deposition as well as the interaction of morphology with the transport and deposition within the river basin.

Lee et al. (1993) stated the example of Tan-Shui River in Taiwan, where the bed elevation of the downstream reach close to the river mouth was lowered by 30-40 m below sea level. They conducted a series of experiments to investigate the migration and shape of rectangular mining pit of different dimensions under the action of different flow conditions. Experiments were conducted for non-equilibrium conditions of sediment flow. They observed migration of mining pit towards the downstream direction. They detected two distinct periods within the temporal scale of migration, namely convective period and diffusion period. The migration speed was constant for both the periods and directly proportional to the transport capacity. Regression equations for the description of migration speed and the pit geometry were developed from the experimental data. These equations predicted the geometric properties and migration speed of a rectangular mining pit.

Yeh & Tung (1993) studied the uncertainties within the pit-migration model proposed by Lee et al. (1993). The model proposed by Lee et al. (1993) provided an estimation of parameters such as migration speeds, shape, and the maximum depth of the pit, based on experimental data. Yeh & Tung (1993) assessed the uncertainty associated with the model using three methods, namely Harr point estimate (PE) method, First-Order Variance Estimation (FOVE) Method, and Latin Hypercubic Sampling (LHS) method. The study suggested the Harr's PE method returned higher values of mean and standard deviation than the other two methods. However, the FOVE and LHS methods provided grater information in context to the stochastic input parameters. According to the authors, more information can be derived out of a model by analyzing its uncertainty, such as contribution of individual input parameters towards the output uncertainty.

Gill (1994) treated the mining phenomenon as a pit in an open channel flow environment and investigated the characteristics of the pit. The author assumed a quasi-steady condition, regular geometrical shape mining pit spanning the full width of the river, and the initial depth of the mining pit was sufficiently smaller than flow depth. The author formulated the problem by using one dimensional St. Venant equations, along with the equilibrium bedload transport equation. The effect of the suspended load was neglected. An approximate theoretical solution was worked out for single trapezoidal and two trapezoidal pits with appropriate initial and boundary conditions. The solutions reported partial filling of mining pit and downstream propagation with time.

Sear & Archer (1998) reviewed the geomorphological effects of mining in several gravel-bed rivers in northeast England, including the Wooler Water in Northumberland, UK. The study indicates drastic vertical instability behavior and planform shifts as a result of 50 years of gravel mining. A massive 9.0 m incision in the river channels for almost 3.5 km was identified. The study provides key understandings in the way active channels respond to gravel extraction in terms of planform changes. The evolution of laterally active wandering planform river into a single-threaded, sinuous channel was reported. The study also showed that the severity of mining operations remarkably depends upon the flow strength, perimeter erodibility, and relative supply of sediments.

Yanmaz & Cicekdag (2000) studied the instability on stream bed around a bridge pier due to channel mining. They developed a one-dimensional model for the study of morphological changes around a bridge pier on the rectangular channel under a quasi-steady flow condition. The morphological changes normally take place in a very long time period during which the temporal changes in flow conditions may be negligible. Therefore the model was based on the assumption that the temporal variations of flow depth and velocity may be ignored during a long morphological time scale. The model is applicable only to a case where the channel mining rate is much greater than the sediment transport capacity of the river. The bank erosion and suspended load were ignored. The Einstein-Brown formula was used for the bedload transport computations of coarse-grained soils. The method is applicable to low flow conditions, class-A flow, through bridge openings. With the application of the model, they observed that the removal of non-cohesive bed material from rivers creates local hydraulic discontinuities at the section of removal. As such, the authors observed that the degradation of stream bed occurs in the downstream reaches of the mining zone. The authors also stated that the extraction of bed materials in large quantities for a longer duration would affect the foundation stability near the bridge pier and other supplementary training facilities. Superposition of the pronounced degradation due to channel mining with the localized scour due to the bridge constriction, local scour around bridge piers and abutments, and lateral degradation decrease the overall bridge foundation stability. Therefore, strict regulations were suggested within the scope of the development of regional watershed management practices to avoid excessive channel mining in close vicinity of hydraulic structures.

Neyshabouri et al. (2002) conducted experiments in a laboratory flume and field channel to study the characteristics of mining pit progression. For the laboratory tests, several dimensions of a rectangular pit were studied to obtain a range of length/width ratios. The authors analyzed the migration speed of the mining pit in both the convection period and the diffusion period. The convection period was defined by the authors as the time required for the upstream edge of the pit to travel to the downstream edge. The diffusion period is the time from the end of the convection period until the end of the migration of the pit. The migration speed was found to be a function of the length/width ratio of the

pit. Also, the speed of migration was greater in the convection period than the diffusion period. The authors also studied the behavior of the rectangular pit excavated in a field channel. The results showed remarkable similarities to the laboratory experiments.

Cao & Pender (2004) developed a theoretical background for one and two-dimensional numerical modeling of alluvial rivers subjected to interactive sediment mining and feeding in the context of shallow water hydrodynamics. The results showed upstream bed degradation from the extraction zone and some aggradation on downstream zones. The location of transition from degradation to aggradation shifted further downstream with an increase in the magnitude of extraction. The free surface was also affected on account of mining. The free surface elevation at upstream of the extraction zone was lowered significantly. However, mining showed a negligible effect on the free surface elevation in the downstream of the extraction zone. The numerical models also presented the changes in the sediment concentrations triggered by mining. The sediment concentrations were significantly reduced within the extraction zone.

Nilipour et al. (2004) conducted a physical model study of a gravel mining pit excavated in the Rhone River in the Rarogne Region. A scale ratio of 1:45 was adopted for the physical model tests. The scaling of bedload sediment in the physical model was based on total roughness by grain size and bedform type. This scaling approach resulted in a 0.2 mm diameter uniform sand particles to be used in the model. Velocity measurements were recorded using 4 UVP (Ultrasonic Velocity Profiler) transducers having 2 MHz frequency. The bed geometry was also recorded using the UVP. The results indicated migration of the pit in the downstream as well as downstream bed degradation. They also observed an increase in the migration speed, bed shear stress, and extent of downstream bed degradation with increasing flow discharge. Based on these results of the physical model tests, the authors recommended safety provisions for the engineering structures present downstream of the mining zone in Rhone River.

Shourian & Neshabouri (2004) studied the migration and geomorphic characteristics of a mining pit based on SSIIM (Sediment Simulation in Intakes with Multiblock option) model simulations. The model applied transient Navier-Stokes equations and $\kappa - \varepsilon$

turbulence model. The model considered bed both load as well as suspended load. The suspended load calculations were performed using the convection-diffusion equation for the sediment concentration, and for bedload, Van Rijn's formula was adopted. Three different cases were simulated, with the initial location of the mining pit varied from the center of the channel to the edge of the channel. The authors observed that as the pit was excavated closer to the center of the channel, the migration speed, as well as upstream degradation, occurs faster. As the initial condition of the pit comes closer to the channel center, the final pit depth is reached earlier, which indicates a faster diffusion rate.

Rinaldi et al. (2005) reviewed a number of documented case studies from various countries, including case studies on five rivers in Italy and Southern Poland. From the case studies and various reviews, they reported severe river bed degradation and channel modification. The authors mentioned that in-stream sediment mining-induced propagation of upstream and downstream river bed degradation. They reported that when the in-stream mining operations coincide with other human interventions and activities, severe geomorphic adjustments occur within the fluvial system. Some of these adjustments include deep river downcutting, changes in the patterns of the riverbed, and even a transformation of the alluvial riverbed into bedrock. The type, severity, and extent of the geomorphic alterations mainly depend upon the quantum of sediment extraction in comparison to annual replenishment rates. The authors also identified management outlooks of sediment mining and proposed the grant of mining permissions based on sufficient analysis of fluvial geomorphology and hydraulics at the basin level. The study insisted on the identification of possible sites for sediment extraction based on detailed analysis, including maximum allowable extraction rates, possible effects of mining activities, and continuous monitoring of the river basin. The authors strongly recommended that mining activities should be allowed only in aggrading rivers, on account of its detrimental effects.

Rovira et al. (2005) studied various effects of intensive gravel mining after historical gravel mining during the period of 1956-1987 in the lower Tordera River, Spain, which was mined at a rate 14 times higher than the replenishment rates. The authors used the sediment budget approach by means of sediment transport measurement for assessing and

managing the present and future sediment deficits in the excessively mined river. They observed that two mining pits were still present in the river profile even after 15 years of ceasing mining activities. The average incision of 1.5 m along the riverbed occurred due to mining. After nearly two decades of the prohibition of in-stream mining, the riverbed showed an annual aggregation rate of 3.6 mm. The authors found that the estimated time for the Tordera River to recover its pre-extraction bed level would be around 420 years.

Ikhsan et al. (2009) did a study on the Progo River, which originated at Mt. Merapi, one of the most active volcanoes in the world. They found that sediment mining was very intensive at lower Progo River as a result of which river bed degradation occurred in this area. They conducted sediment budget analysis and also gave a concept of sustainable sediment mining by installing ground sill on the river bed. They simulated a mathematical model for one-dimensional bed deformation using the Saint Venant equations equation. They found that bed deformation between groundsill was very fast, and bed slope became milder with time.

Chen & Liu (2009) investigated the impact of sand and gravel mining on river bed changes and flood zone coverage of the Rio Salado, Salt River, Arizona, by using one dimensional HEC-RAS and two-dimensional CCHE2D model and compared their result with field observation. The hydrodynamic modeling was executed for a 500-year flood event using both HEC-RAS and two-dimensional CCHE2D model. The study reported different results from both models. HEC-RAS simulation showed severe head cutting at upstream of the mining pit, while CCHE2D simulation indicated downstream degradation of the riverbed. The authors commented that in the case of hydrodynamic simulation, HEC-RAS produces similar results as CCHE2D, but CCHE2D model gave more robust simulation in terms of flood zone coverage, non-uniform sediment sorting, and geomorphologic channel changes.

Chen et al. (2010) conducted a sensitivity analysis of non-equilibrium adaptation parameters for modeling mining pit migration. They used CCHE2D, a depth-averaged two-dimensional hydrodynamic and non-equilibrium sediment transport model to simulate the flume experiment conducted by Lee et al. (1993) and found non-equilibrium

adaptive length and coefficient. They were unable to give any empirical relationship of non-equilibrium adaptive length and coefficient. Still, their results showed that equilibrium and near-equilibrium schemes were not suitable for the calculation of mining pit migration.

Martín-Vide et al. (2010) stated that the approaches that Lee et al. (1993), Gill (1994) described, is a static approach where the pit in the initial bed was tracked afterward in time and space. So the duration of the mining pit must be small compare to the time of river bed changes. But these authors considered the condition in which gravel mining last for several years. They presented two methods, sediment budget approach and linear diffusion model. For sediment budget approach they applied mass balance model for bed load transport, which stated that the difference between incoming and outgoing gravel equals the change in volume within the reach. For diffusion model of bed profile evaluation they used Saint Venant equations, Exner equation for sediment conservation with an additional sink term. This model was an equilibrium sediment transport model. Bed load discharge was made equal to the transport capacity using bed load equation such as Meyer-Peter and Muller (MPM 1948). Diffusion equation was developed analytically assuming constant channel width and uniform bed material. In this study authors aimed to provide a methodology that can be used to quantify the effects of gravel mining in terms of river bed degradation using the diffusion coefficient. Their results matched with field data from Gallego River, Spain.

Azar et al. (2011) conducted flume experiments with different dimensions of a rectangular mining pit subjected to steady flow conditions. The authors expressed the non-dimensional functional relationship of migration speed with the depth of the pit, length of the pit, inflow shear velocity, the density of sediments, mean particle size of sediments, and convection period. It was observed that migration speed increases with a decrease in the depth of the pit. As compared to length and breadth, the migration speed was more sensitive to the pit depth. The migration speed was constant for both the convection period and the diffusion period. The authors used the experimental data and the functional relationship developed using Buckingham's π to present an empirical

equation of migration speed as a function of shear velocity, depth of pit, and length of the pit.

Brestolani et al. (2015) investigated the morphological changes due to large scale gravel mining occurred during 2003-2004 in the Orco River, located in the Piemonte region. They used CNR-IRPI experimental methodology based on multi-years LiDAR surveys realized in the years 2003, 2004, 2006, and 2007 to document mining and morphological response of the river to mining. They observed that incision propagates both upstream and downstream of the mining pit. The incision was about 2.0 – 3.0 m deep and propagated 3000 m downstream and 2000 m upstream of the mining pit. A hydro-morphological one-dimensional model BASEMENT was used to reproduce morphological changes that happened after the gravel extraction in the period 2004-2006, and the results obtained were quite satisfactory. The authors suggested a collective approach of high resolution and high-quality river surveys coupled with numerical modeling of the hydro-morphodynamics to study the response of rivers to in-stream mining activities.

Jang et al. (2015) studied the migration of a rectangular mining pit having 1.0 m length and 0.1 m depth in a uniform sand bed channel. The authors observed headcutting erosion in the upstream zone of the pit. After a sufficient period, filling of pit occurred by the incoming sediments eroded from the bed, and migration of pit was observed. The authors conducted two-dimensional numerical modeling to compare the numerical and experimental results. The cubic interpolated pseudo-particle method was adopted to realize the channel alterations. The numerical experiments showed initial headcutting erosion, which migrates upstream, similar to experimental results. As the headcut migrated upstream, there was a partial filling of the pit. The wedge of sediment deposit migrated downstream, and headcut erosion ceased. The system achieved a new state of quasi-equilibrium after the filling of the pit. The numerical model performed satisfactorily in capturing the morphological evolution of the pit. The migration speed was found to decrease with increasing shear velocity. Also, the depth of the mining pit decreases with an increase in migration speed. The numerical model slightly overestimated the migration speeds as compared to experimental results. To better

analyze the disturbed channel morphology, sediment was replenished from the upstream. The numerical model indicated that the migration speed is proportional to sediment inflow.

Samadi & Azizian (2015) simulated morphodynamics of mining operations in Sarbaz River near Rask city in Iran using CCHE2D model. The actual mining pit in the river, excavated using hydraulic excavators, was about 3.0 m deep, 20.0 m wide, and 32.0 m long. Different values of Mannings roughness coefficient for the left bank, right bank, and main canal were estimated for the river and used in the numerical model. Field measurements of longitudinal river profiles were recorded for a period of one month. The numerical model using the Ackers and White sediment transport function was able to satisfactorily simulate the propagation of the mining pit and resulting longitudinal profile of the riverbed.

Barman et al. (2017) conducted experiments to study the migration of a mining pit on the downstream side. A rectangular flume of 17.2 m long and 1 m width was used for these series of experiments. Channel bed was covered with a 21 cm thick uniform sand layer of particle size (d50) 0.418 mm and a standard deviation 1.17. A pit of 50 cm length and 10 cm depth in the whole width of the channel was made at 7.5 m from a downstream point. The experiments were performed by varying the Froude number keeping the flow conditions subcritical and without sediment overloading at the upstream side. The bed morphology was measured at various time intervals using SeaTek Ultrasonic Ranging System with 0.1 mm resolution. It was found that for all the experiments, sediment transport takes place as the Shield's stress is more than critical shear stress. It was also observed that the upstream end of the mining pit is moving towards downstream with time, and degradation of channel bed is more prominent in downstream of the mining pit. The migration of upstream end of the pit and downstream propagation of degradation increases with an increase in the flow velocity and Froude number for constant channel geometry and sediment properties. Also, when the removal of bed material is in excess of replacement by transported material from the upstream side, lowering of bed in the downstream has been observed.

Qi & Kuai (2017) studied the scour evolution by considering the effects of retrogressive erosion on total scour at the underwater structure. Flume experiments were conducted to study the factors of retrogressive and local scour by conducting drop tests wherein the bed level was suddenly dropped at downstream of the pier. Uniform quartz sand having d_{50} of 0.6 mm was used for the experiments. Their paper focused on the problem of the influence of trace-source scouring on the scour around the underwater structure caused by sand mining in the riverbed. They considered the effect as a coupling scour, which acts in addition to local scour due to flow contraction near the bridge pier. The scouring was studied once with retrogressive erosion and once without it. The results showed that in a particular location, the rate of retrogressive erosion is much higher than that of the local scour at the pier. The study also proposed a time-dependent calculation method for the coupling scour. The authors suggested that the mining pit contributes to the total scour in addition to local scour around the bridge pier.

Qi et al. (2017) conducted flume experiments to study the mitigation of pier scour Effect of Bottom Hurdle on Erosion Reduction of Bridge Pier in Sandcutting River Bed by installing sill in the river bed. For these experiments, an end sill is placed downstream of the pier. The flow turbulence structure was measured by Particle Image Velocimetry to study the correlation between sill scale, the redistribution of water flow, and the efficiency of pier scour mitigation. It has been found that the scour mitigation mechanism by bed sill decreases turbulence intensity, shear stress, and turbulence vorticity of water flow and also reduces the sediment transport capacity of water flow to prevent pier failure. Experimental results showed that under the same flow condition, the efficiency of pier scour mitigation varies with the height of the sill above the river bed and the distance between the sill and the pier. The authors suggested that the bottom ridge along the river width in the lower reaches of the bridge site can reduce the impact of sediment evolution on the pier erosion in the upper reaches of the bridge. At the same time, it can block the evolution of the downstream sediment recovery. The efficiency of the bottom ridge or end sill depends upon the height of the ridge, the relative distance between the pier and the ridge, and the intensity of the flow. They suggested that by optimizing the ridge, the near-bed turbulence can be decreased, and maximum efficiency of 30 % can be achieved in the reduction of sediment flushing due to the mining pit. The ridge should be kept

sufficiently deep and placed before the onset of source scour, i.e. before the excavation on the streambed.

Barman et al. (2018) conducted experimental studies to understand the hydrodynamics of a mining-affected channel. Trapezoidal pit was excavated in a flume having sand bed. Instantaneous velocity data was taken using an Acoustic Doppler velocimeter at various sections along the channel. It was observed that the mining pit propagated downstream with time. The study revealed that Reynolds shear stresses and turbulent intensities become higher in the mining region and downstream of it, as compared to the upstream section, which causes rapid movement of bed particles. The authors observed higher sediment transport capacity of the channel at the mining pit location, which caused channel bed lowering in its downstream side. The authors also studied the bursting events within the turbulence around the mining pit. They found that the sweep events and ejection events dominated the Reynolds shear in the near-bed region. These characteristics of turbulence around the pit were responsible for excess transport and erosion.

Chen et al. (2018) studied the effect of river dredging on the bearing capacity of the pile foundation of bridge using numerical and field investigations. The authors reported a severe loss of more than 25 % in the bearing capacity of soil below a single pile foundation. The decrease in bearing capacity increased with an increase in the depth of river mining. This could result in additional stresses in the foundation structure. However, sand mining did not affect the stresses in the upper structure adversely. Dynamic load tests on the pile foundation using vehicular loads suggested that the dynamic displacement of the pier subjected to river mining was considerably greater than the one free from mining. River mining posed serious concerns to the safety of bridge piers on account of decreased bearing capacities and excessive dynamic displacements.

Haghnazar & Saneie (2019) conducted steady flow erodible bed flume experiments with two mining pits. They studied the transport characteristics and morphological evolution of mining pits for various distances between the pits for better mining management. They observed that the rate of filling and migration rate decreases with an

increase in the distance between the two pits. However, the migration velocity of the upstream pit is independent of the distance between the pits. When the distance between the pits was14 times the flow depth, the desirable effect was seen in the filling of the downstream pit. However, when this distance was greater than times the flow depth, the infilling volume of the downstream pit was reduced significantly. Based on the experimental results, the authors proposed the mining pits should be dredged in the center portion of the channel, and the distance between them should be less than or equal to 8 times the flow depth. This configuration would achieve better filling and migration of pits.

Peng et al. (2019) conducted numerical modeling of a large barrow pit lower Mississippi River having a volume of 1.46 million m^3. The authors used a CCHE2D two-dimensional depth-averaged hydrodynamic and sediment transport model. The post-dredging river morphology was obtained from field bathymetry surveys. Curvilinear and orthogonal meshes were used in the study, which divided the study domain into 50 x 355 grids. Error analysis between the calculated and measured data was done using three methods, namely bias analysis, geometric mean error analysis (AGD), and square root analysis (RMS). The performance of the numerical model was found satisfactory in predicting the average bed-level changes `post-mining operations, as long as the significant model input parameters such as non-equilibrium adaption coefficient are calibrated appropriately. The authors reported that the model tends to overestimate the fillings rate if a large adaption coefficient is adopted.

1.7 Need for Research

River mining is a prominent source of course and fine aggregates in India. In the last few decades, the construction industry in our country has seen rapid augmentation resulting in a rise in the demand for construction raw materials, including aggregates. The apex court has acknowledged the fact of serious unrestricted upstream, in-stream, and flood plain mining activities in the river beds of Ganga, Narmada, Yamuna, Tangri, Markanda, Ghaggar, Krishnavati River basin, Dohan River basin, etc.

Local scour refers to the removal of sediment from the immediate vicinity of bridge piers or abutments. Field observations suggest that due to the mining pit, there is severe degradation as well as lowering of channel bed and pit migration in the downstream side. This phenomenon can drastically alter the local scouring around bridge piers present in the downstream side, which can lead to undermining and failure of such hydraulic structures. Therefore it is of utmost importance to study these effects on the morphodynamics in the vicinity of bridge piers present in downstream of such mining pits.

As per the mandate of the Ministry of Water Resources, Government of India, mining of sand is proposed at an optimum level for removing excessive sediment deposit in rivers. However, unscientific sand mining depletes the mineral at rates at which the river system cannot replenish it. The ministry has acknowledged the fact that excessive mining undermines the ability of riverbeds and riverbanks to support the infrastructure built on them, such as bridges, electricity poles, and buildings, because it weakens the structural integrity of the sand, making this an issue of national importance.

Mining affects the morphology of the river, causing progressive downstream channel incision. This effect alters the sediment transport characteristics of the stream and can lead to undermining and failure of bridges on downstream of the mining pit due to pronounced local scour. Several cases of such bridge undermining and failures have been reported in countries like Turkey, Jarama River in Central Spain, Drome River in Southeast France, Wooler Water in Northeast England, Wisłoka River, in Southern Poland etc. In our country, looking at the quantum of unrestricted mining on major rivers like Ganga, Yamuna, Narmada etc., the safety of hundreds of bridges built across these rivers is in jeopardy.

From the review of the present literature, it can be strongly ascertained that mining of sand in rivers cause upstream and downstream incision of the channel bed. This postulate has been affirmed by various field studies as well as numerical and experimental model studies. Also, few available studies confirm that the mining pit leads to a retrogressive scour coupled to the local scour around the bridge pier and can affect its stability. But

thorough understanding of this physical process is lacking as comprehensive studies are not documented in the literature. Additional laboratory and field investigations are required to precisely understand the effects and impact of mining pit on hydrodynamics and morphology around bridge piers.

The proposed research work will contribute to the present knowledge by providing answers to the following questions:

- What are the effects of river mining on the total scouring pattern and morphology around bridge piers in the downstream side?
- What are the effects of river mining on the hydrodynamics of the flow around bridge piers?

The findings of the project shall be helpful for hydraulic engineers to understand the scour phenomenon bridge piers in mining-induced alluvial channels so that appropriate protective measures can be proposed. It will also provide an engineering base to frame policies regarding mining in river bed upstream of bridges in our country.

1.8 Objectives

The process of aggravation of local scour around bridges due to mining is complicated, and a precise understanding of this process is not yet formulated as detailed scientific studies are lacking. This project aims at filling this gap in the presently available literature. An experimental program is being proposed, which will include a model of a circular pier placed in a sand bed laboratory flume with upstream mining pits of various shapes. The following are the objectives.

1. **Effect of a mining pit on the structure of turbulence around a bridge pier**
    - To study the effect of a mining pit on the mean flow structure around a bridge pier using turbulent velocity measurements at critical locations.
    - To examine the effect of mining pit on the turbulent flow characteristics around a bridge pier.
2. **Effect of a mining pit on geomorphic characteristics around a bridge pier**

- To study cross-section and longitudinal section of scour hole around a pier with and without mining pit.
- To study the effect of a mining pit on the morphological characteristics around a bridge pier such as upstream bed level, downstream dune formation, etc.
- To study the effect of a mining pit on the evolution speed of scour depth on the basis of multi-scale statistical celerity of scour depth with and without mining pit.
- To examine the effect of distance between the mining pit and bridge pier on morphological instabilities around a pier.

1.9 Organization of Thesis

Chapter 1 provides a brief introduction to river mining in the context of fluvial hydro-morphology. Various aspects of river mining, such as types, effects, etc. are discussed. The problem of undermining of bridge piers due to mining activities is discussed in detail, based on the current literature. Finally, the objectives of the study are outlined.

Chapter 2 describes the experimental methodology applied to the study. It includes the experimental design, experimental program as well as data collection methods. The details of the instrumentation are also provided.

Chapter 3 deals with the effects of a mining pit on the hydrodynamics around bridge piers. Turbulence parameters around critical locations around a circular pier, oblong pier as well as two circular piers in tandem are explored, under the influence of a mining pit.

Chapter 4 deals with the streambed instabilities around a circular pier caused due to a mining pit. The effects of pit shape and distance between the pit and pier on the streambed instability parameters are also evaluated. The evolution celerity of the local scour hole in a dredged channel is also analyzed using wavelets.

Chapter 5 presents the major conclusions of the study, in context to the hydro-morphological alterations around bridge piers caused due to mining. A few recommendations regarding the policy of sand mining practices near bridges are outlined based on the findings. Finally, a few suggestions for future research on the concurrent aspects are provided.

Chapter **2**

Methodology

2.1 Overview

Experimental Research Methodology has been adopted to achieve the said objectives of the project. Gravity flow experiments were conducted in a laboratory flume, having an erodible bed to study the effects of a mining pit on the hydromorphology around the bridge pier. The details of the experimental setup are described in this chapter. The experimental procedures, data collection methods, as well as data processing techniques are also illustrated.

2.2 Experimental Setup

2.2.1 The Flume

Gravity flow experiments were conducted in a 17.1 m long rectangular flume with 1.0 m width and 0.72 m depth (Figure 2.1). Both sides of the flume were glass fabricated so that the flow inside it is visible to naked eyes. The flume had a recirculation arrangement of water so that steady flow conditions could be maintained throughout the period of the experiment. Recirculation was achieved by three centrifugal pumps having 7.35 kW power. A maximum steady flow discharge of about 0.060 m^3/s could be maintained in the flume using all three pumps. An underground sump having a storage capacity of about 70 m^3 capacity was used for water supply. The water was first pumped into an overhead tank using the three centrifugal pumps. A supply pipe having an internal diameter 200 mm supplied water from the overhead tank to the entrance chamber of the flume. A high precision butterfly valve was installed in the supply pipe to achieve precise discharge regulation. The entrance chamber was sufficiently large (2.8 m length, 1.5 m width, and 1.5 m depth) to achieve tranquility and eliminate any unsteady local fluctuations when the water flowed from the overhead tank. As the water flowed from the chamber into the flume, cross-aligned wooden baffle walls were provided for the smooth entry of flow into

the flume. The first 2.0 m length of the channel was non-porous, and a gravel layer was laid at the channel bed. The remaining 15.2 m of the flume was laid with a sand bed. An overflow tailgate was installed at the downstream end of the flume to regulate the low depth. After flowing out of the flume, the flow passed into a collecting tank installed with a rectangular notch at the end. The water flowed through the notch and went back to the underground sump tank through open canals, and recirculation continued. A bedload tank was attached at the end of the flume, which collected the bedload sediments. The sill level of the bedload tank was flushed with the sand bed level.

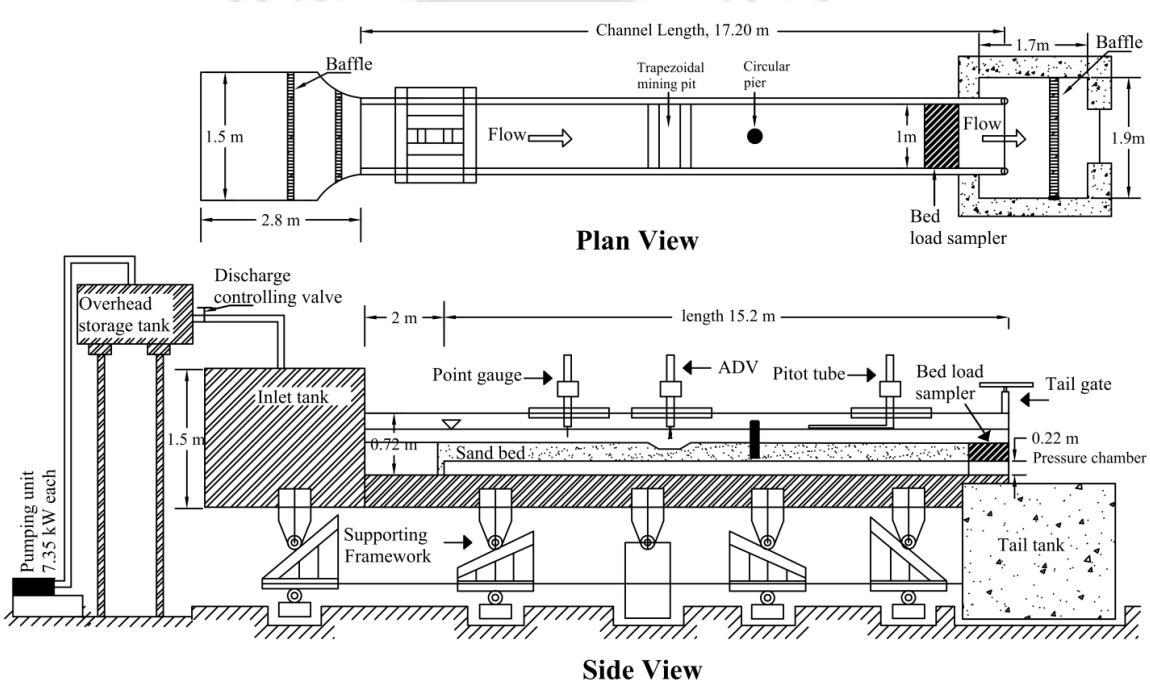

Figure 2.1 Schematic drawing of the experimental setup

2.2.2 Channel bed material

River sand having a 1.1 mm median particle diameter (d_{50}) was used for the experiments. The particle size distribution curve of the sand is plotted in Figure 2.2. The particle size distribution of the sand was uniform as the geometric standard deviation was less than 1.4 (Marsh et al., 2004). The dry angle of repose of the sand was 31.1°. The critical shear velocity $\left(u_{*cr} = \sqrt{\frac{\tau_{0cr}}{\rho}}\right)$ and the critical bed shear stress (τ_{0cr}) was calculated as 0.0262 m/s and 0.686 N/m², from the Shield's curve.

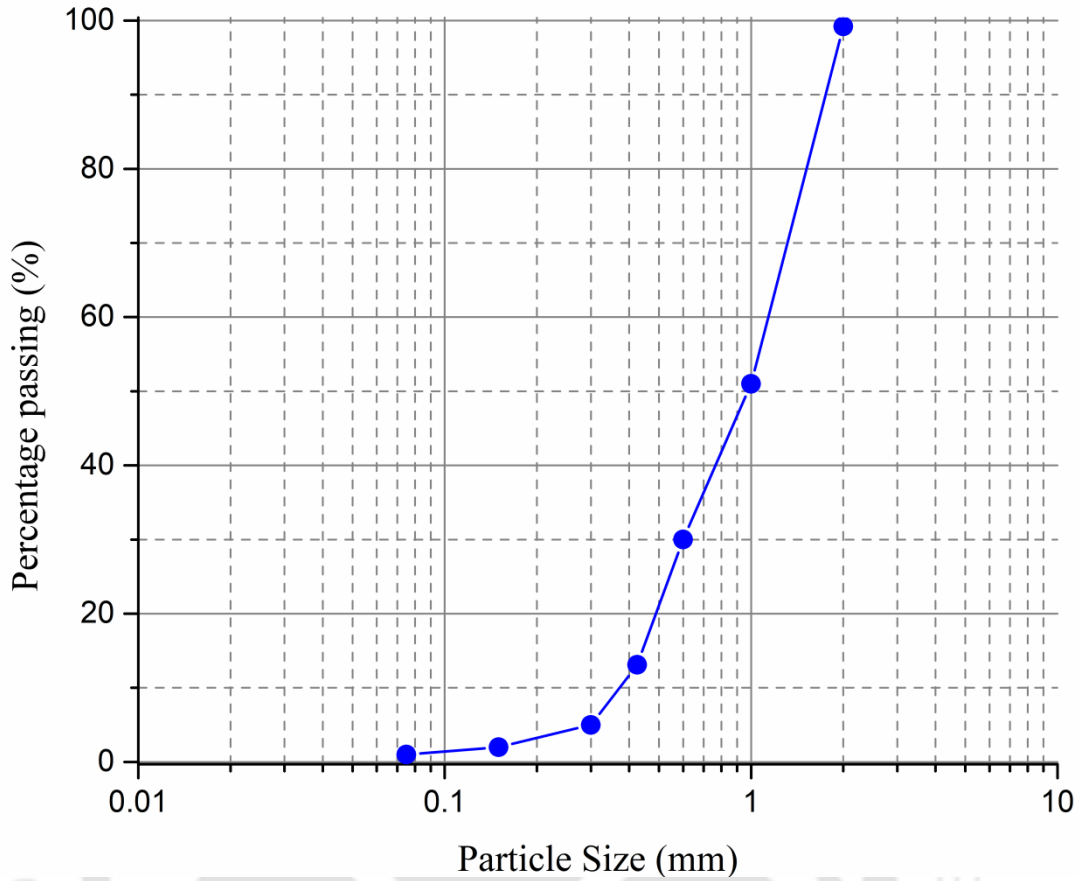

Figure 2.2 Particle size distribution curve

2.2.3 Flow discharge measurement

The flow discharge was measured using a rectangular notch (Figure 2.3) fitted at the end of the collecting tank. The width of the notch (L_n) was 0.5 m. The rectangular notch was calibrated, and the coefficient of discharge (C_d) was found to be 0.82. The steady flow discharge for the experiments was calculated using the following equation.

$$Q = \frac{2}{3} C_d \sqrt{2g} L_n H_n^{\frac{3}{2}} \quad (2.1)$$

where g is the acceleration due to gravity, and H_n is the head over the notch.

2.2.4 Flow depth and bed level measurement

A digital point gauge (Mitutoyo Corp®) having a least count of 0.01 mm was used for the measurement of flow depth with respect to the bed level. The digital point gauge

displayed the level on a liquid crystal display (LCD) with respect to a preset zero level. It was mounted on a movable trolley, which could be traversed easily along the length of the channel. At a particular longitudinal position along the channel length, the point gauge could also be moved in a transverse direction along the flume width. Before the start of the experiment, the initial sand bed level was set to zero. The depth of water could be measured with respect to the channel bed level at various locations. At the end of the experiment, the bed deformation occurred, and the morphological changes around the bridge pier were recorded using the digital point gauge. A snapshot of the digital point gauge being utilized to record the bed level within the local scour zone is shown in Figure 2.4.

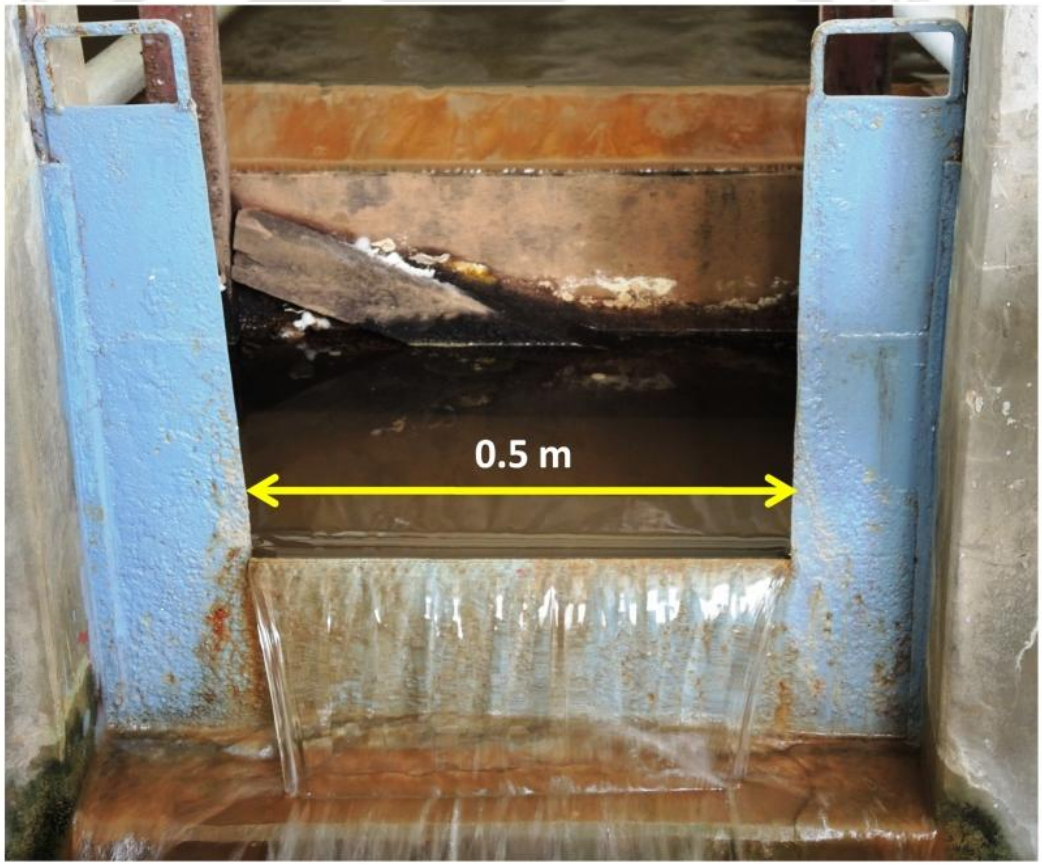

Figure 2.3 Rectangular notch for discharge measurement

Figure 2.4 Digital point gauge

2.2.5 Velocity measurements

Three-dimensional velocities were recorded using a Nortek® Vectrino^{+} model Acoustic Doppler Velocimeter (ADV). The ADV uses the Doppler shift principle for velocity measurement. The probe has one transmitter and four receivers, as shown in Figure 2.5. The transmitter emits acoustic signals to a remote sampling volume located 50 mm away

from the transmitter tip. The sampling volume is cylindrical and having a 6 mm diameter and 2.5 – 9 mm in length. The length of the sampling volume can be changed according to requirements. The suspended particles moving along with the flow which have the flow velocities reflect the transmitted waves, and four receivers capture these waves. Based on the changes in the transmitted and received frequencies of the signals, ADV processes the velocities in three orthogonal directions.

Nortek® Vectrino^{+} is a downward-looking four-probe fixed stem model with an acoustic frequency of 10 MHz (Figure 2.6). It can sample instantaneous velocities at a maximum frequency of 200 Hz. The probe has a temperature sensor with a range of -4º C - 32ºC, with an accuracy of ±0.1º C.

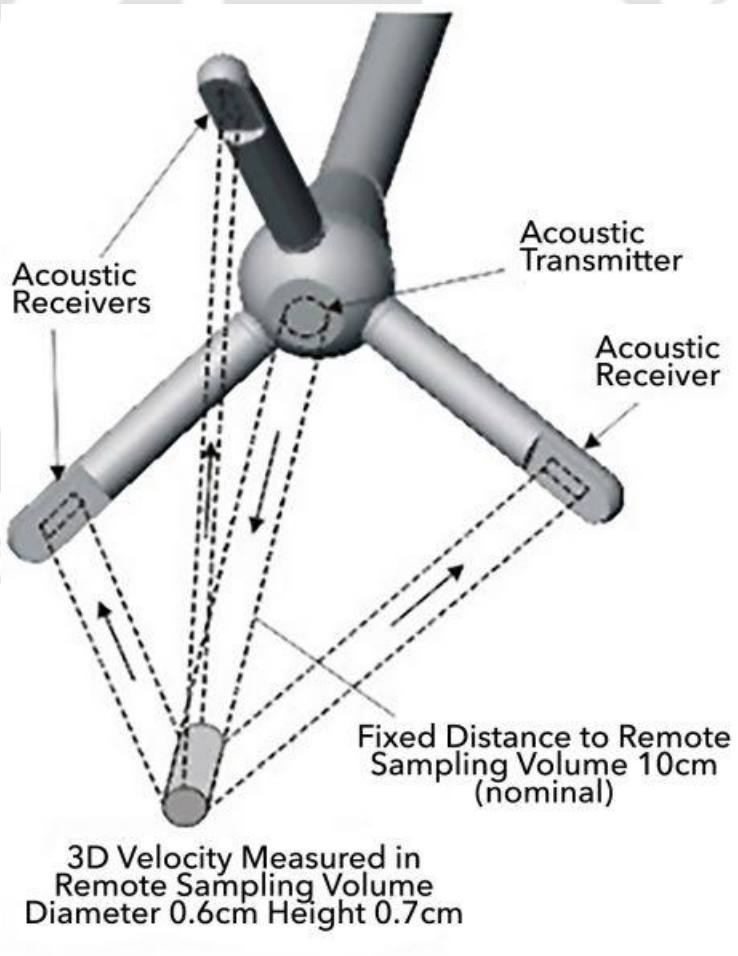

Figure 2.5 Transmitter and receiver probes of an ADV with a remote sampling volume (Image downloaded from https://www.sontek.com/argonaut-adv)

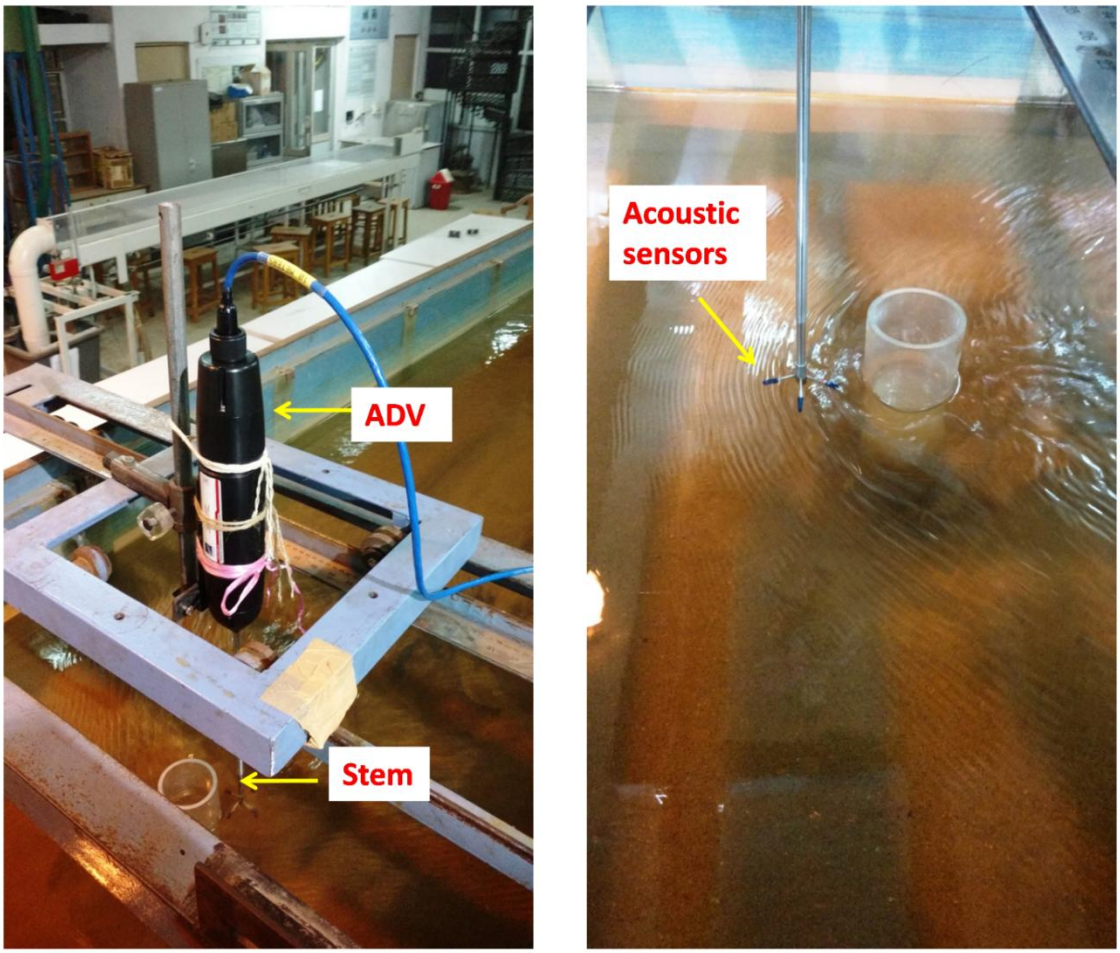

Figure 2.6 Snapshots of velocity measurements using Nortek® Vectrino^{+}

At a particular measurement point, instantaneous velocities in the streamwise (X), lateral (Y), and vertical (Z) directions can be represented by u, v, and w, respectively. Fluctuating elements associated with these instantaneous velocities can be represented by u', v', and w' respectively. The instantaneous velocities in X, Y, and Z directions can be decomposed as $u = \bar{u} + u'$, $v = \bar{v} + v'$, and $w = \bar{w} + w'$ respectively. The temporal average velocity components in X, Y, and Z directions are $\bar{u}$, $\bar{v}$, and $\bar{w}$ respectively. The velocity signals are recorded using Vectrino Plus software developed by Nortek®. The software records the instantaneous velocity, signal to noise ratio (SNR) in dB as well as correlation (%) as shown in Figure 2.7. Uncertainties involved in the velocity measurements are presented in Table 2.

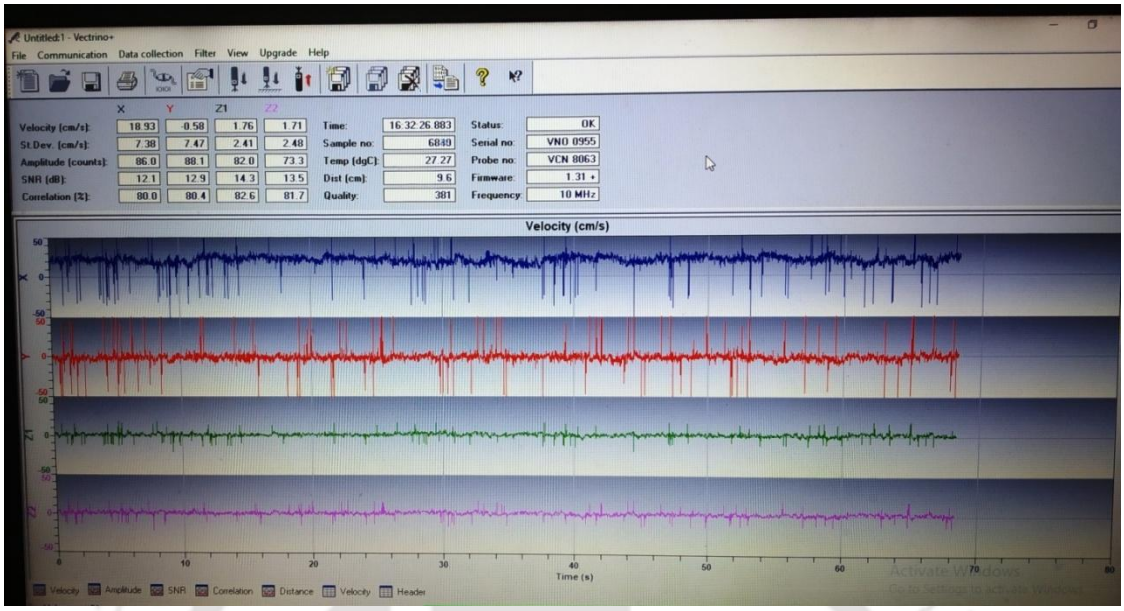

Figure 2.7 Snapshots of graphical user interface of Vectrino^{+} software during velocity data recording

Table 2.1 Uncertainty assessment of the recorded data

	u	v	w	$\left(\overline{u'u'}\right)^{0.5}$	$\left(\overline{v'v'}\right)^{0.5}$	$\left(\overline{w'w'}\right)^{0.5}$
Standard deviation	0.00358	0.00074	0.00098	0.00655	0.00090	0.00025
Uncertainty (%)	0.42	0.12	0.06	0.15	0.05	0.02

2.2.6 Ultrasonic Ranging System (URS)

A Seatek® Ultrasonic Ranging System (URS) was used in the study to record bed elevation time series upstream and downstream of a bridge pier at a high temporal resolution (0.5 s). The URS used eight transducers of 20 mm diameter, which were mounted on a fixed plate mounted on a trolley, as shown in Figure 2.8. The transducers could be placed at any location in the flume where bed elevation had to be measured continuously. The transducer transmits 5MHz ultrasonic pulses that travel through water and reflect back from the bed surface. The echo is received by the same transducer. The

distance is calculated based on the time lag between the transmitted pulse and the echo received. The URS system has an accuracy of ±0.2 mm.

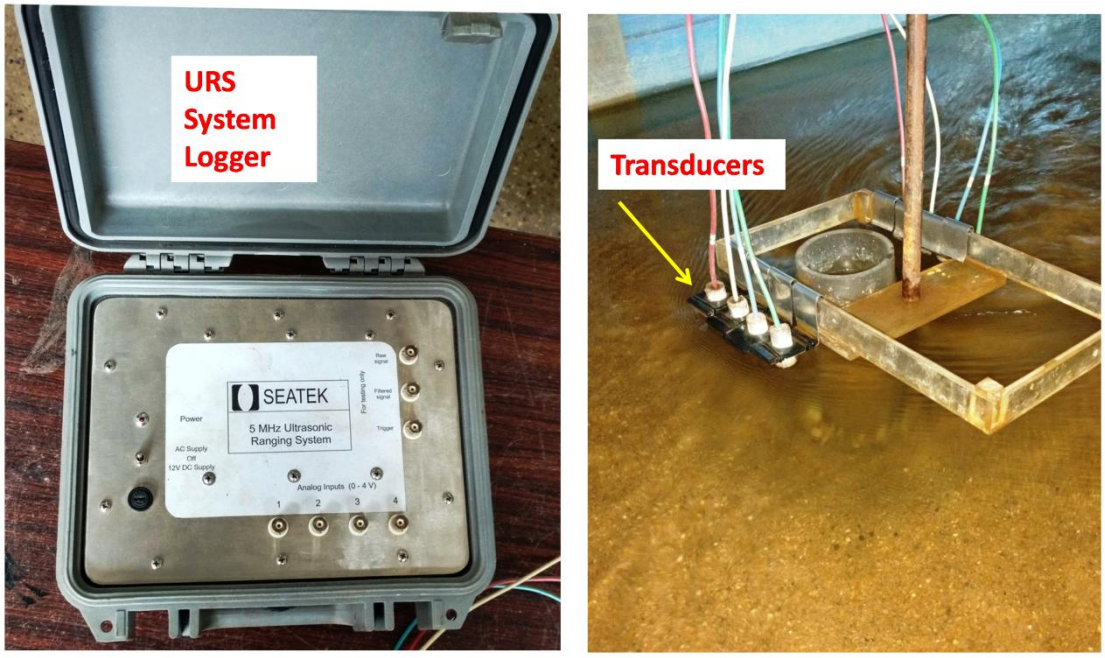

Figure 2.8 Snapshots of Seatek® Ultrasonic Ranging System

2.2.7 Bed preparation

Before the start of every experiment, a plain leveled sand bed was prepared. The sand was uniformly spread on 15.2 m length of the channel bed. A cutter in the form of a sharp metal plate was mounted on a trolley Figure 2.9 (Top). The edge of the cutter was placed 21 cm above the channel bottom. The trolley was moved about 0.3 m at a time, and the sand bed was leveled gradually. Every time the excess sand was carefully removed, and the trolley was moved further. Thus, a uniform leveled sand bed of 21 cm thickness was laid at the channel bottom, as shown in Figure 2.9 (Bottom).

After the end of every experiment, the water was carefully drained out of the channel, and the sand bed was allowed to dry naturally. The top layer of the sand bed was disturbed using trowels carefully. Once again, the above procedure of bed preparation was repeated for the next experiment.

Figure 2.9 Preparation of sand bed with metal cutter

2.3 Experimental Program

The experimental design comprised of excavating a mining pit upstream of a bridge pier model before initiation of the flow. A circular pier model of a 75 mm diameter made of acrylic material was embedded in a leveled sand bed. A mining pit was excavated carefully upstream of the pier. Three shapes of mining pits were tested, namely, rectangular, trapezoidal, and irregular. The depth of all the three mining pits was 100 mm, and the volume of excavation was 0.05 m^3 for all the shapes. The rectangular pit was 0.5 m long along the length of the flume and excavated along the entire width. The top and bottom width of the trapezoidal pit was 670 mm and 330 mm, respectively. The dimensions of the pit are shown in Figure 2.10. All three shapes were tested, keeping the 1.0 m distance between the pit and the pier. To study the effect of distance (L) between the pit and the pier on the hydromorphological alterations, tests of the rectangular pit were conducted for three different distances, namely 1.0 m, 2.0 m, and 3.0 m. The snapshots of the various experimental cases are shown in Figure 2.11 and 2.12.

Experiments were conducted at various flow discharges (Q). For comparative study, tests were also conducted without any mining pit. The details of the experimental program are presented in Table 2.2.

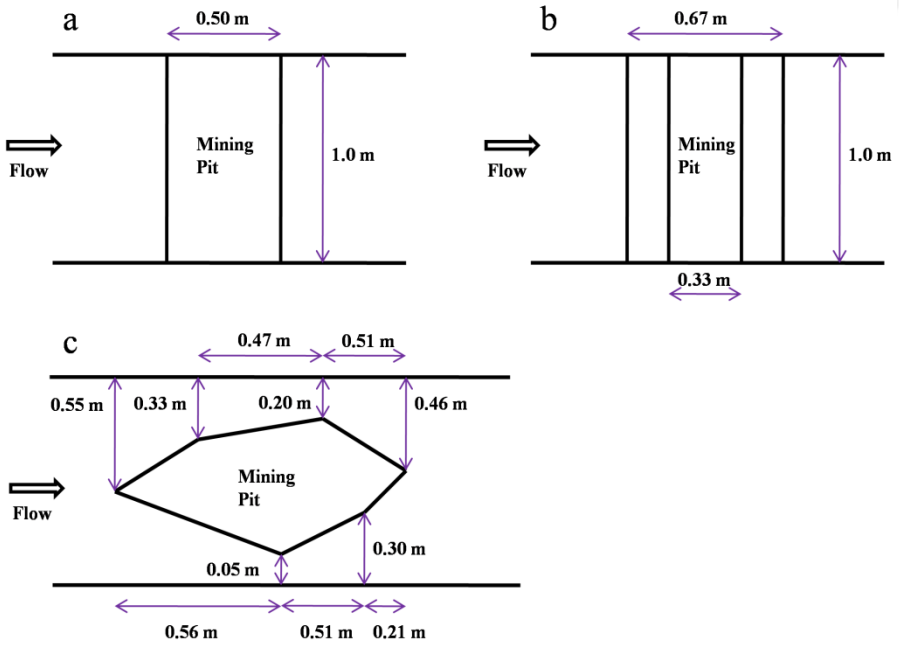

Figure 2.10 Plan view of (a) Rectangular pit (b) Trapezoidal pit and (c) Irregular pit

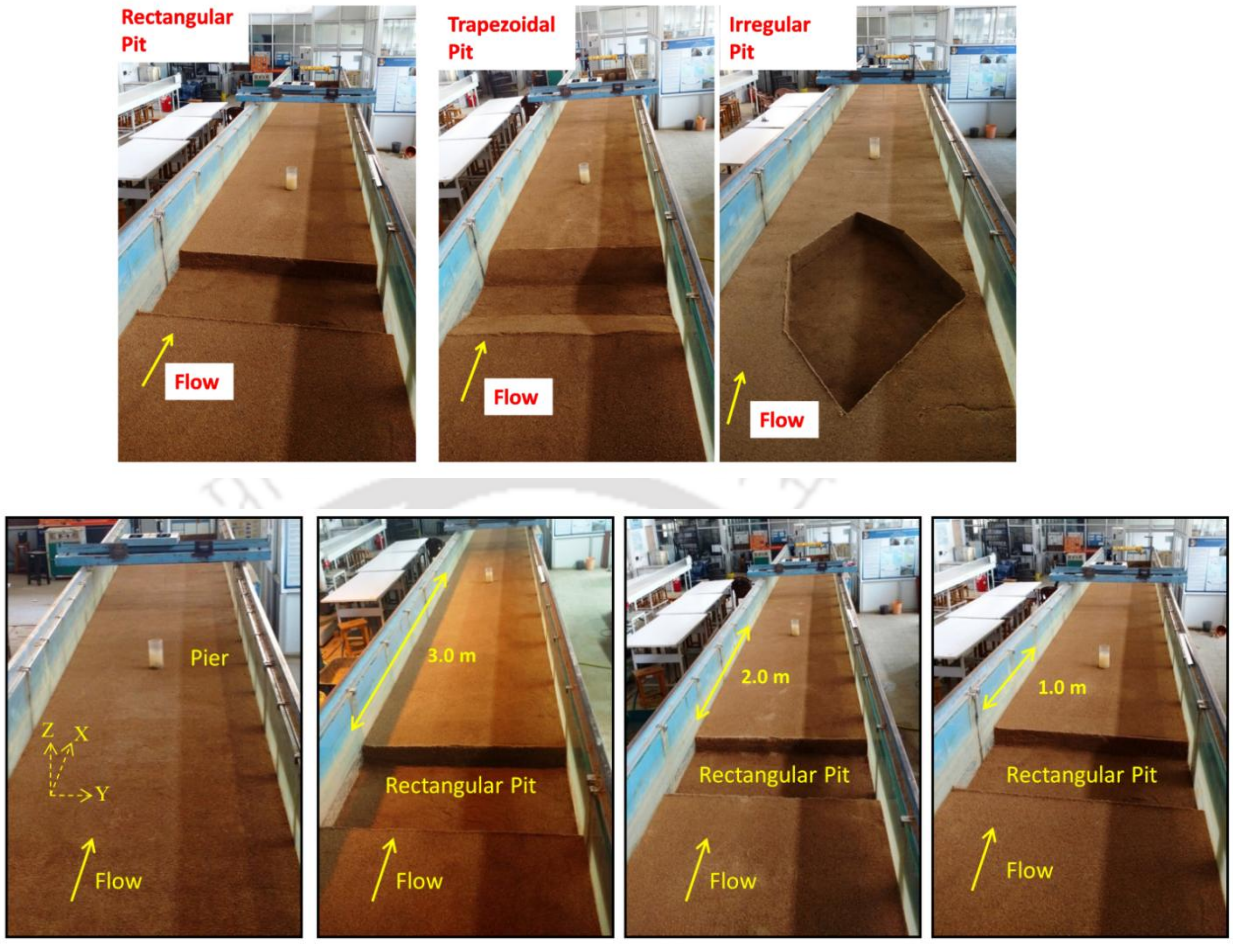

Figure 2.11 Snapshots of various experimental cases

Figure 2.12 Snapshots of pit migration and morphology around pier for all three pit shapes ar Q = 0.0567 m^3/s.

Table 2.2 Details of the experimental program

Case	Discharge (m^3/s)	Distance between pit and pier (L)	Depth-averaged approach flow velocity (m/s)	Froude Number Fr	Reynolds number Re	Shear Reynolds number R^*
No Pit [Set-1]	0.0382	-	0.382	0.467	35768	89.84
	0.0441		0.420	0.493	40951	92.06
	0.0472		0.429	0.485	43470	94.23
	0.0503		0.437	0.477	45949	96.35
	0.0567		0.473	0.498	51377	98.42
Rectangular Pit	0.0382	1.0 m [Set-2] 2.0 m [Set-3] 3.0 m [Set-4]	0.382	0.467	35768	89.84
	0.0441		0.420	0.493	40951	92.06
	0.0472		0.429	0.485	43470	94.23
	0.0503		0.437	0.477	45949	96.35
	0.0567		0.473	0.498	51377	98.42
Trapezoidal Pit[Set-5] Irregular Pit[Set-6]	0.0441	1.0 m	0.420	0.493	40951	92.06
	0.0472		0.429	0.485	43470	94.23
	0.0503		0.437	0.477	45949	96.35
	0.0567		0.473	0.498	51377	98.42

Chapter **3**

Turbulent Flow Characteristics around a Bridge Pier in a Dredged Channel

3.1 Introduction

In this section, the alterations in turbulent flow characteristics around a circular pier, an oblong pier, as well as two circular piers in tandem are studied, based on experimental results.

The turbulence generated due to the fluid-solid interactions around a cylinder becomes significant as it primarily affects the local scouring and deposition characteristics around the cylinder. Several researchers have experimentally studied the turbulent flow characteristics around the cylinder embedded in an erodible bed (Ahmed & Rajaratnam, 1998; Ataie-Ashtiani & Aslani-Kordkandi, 2013; Chiew, 1984; Dargahi, 1989; Das et al., 2013; Dey, 1995; Graf & Istiarto, 2002; Graf & Yulistiyanto, 1998; Guan et al., 2019; Izadinia et al., 2013; Keshavarzi et al., 2014; Kirkil et al., 2005, 2008; Kumar & Kothyari, 2012; Melville & Raudkivi, 1977; Muzzammil & Gangadhariah, 2003; Qadar, 1981; Unger & Hager, 2007).

When a free surface flow interacts with a circular cylinder embedded in the channel, stagnation occurs at the cylinder front. Therefore a negative pressure gradient is formed across the flow depth. Hence the mean flow is deflected downwards towards the cylinder base, and a vortex system is formed at the base of the cylinder, commonly known as the 'horseshoe vortex.' This horseshoe vortex system erodes the sediments at the pier base and transports them downstream (Ahmed & Rajaratnam, 1998; Dargahi, 1989; Das et al., 2013; Kirkil et al., 2008; Unger & Hager, 2007). As the fluid flows past the cylinder, wake vortices are shed at the cylinder downstream, which keep the sediments in suspension, and they are deposited behind the cylinder (Graf & Istiarto, 2002; Melville & Raudkivi, 1977). The down-flow in front of the cylinder, re-circulating horseshoe vortices at the cylinder base, and wake vortices shed behind the cylinder are identified as the principle elements of the flow around a cylinder (Figure 3.1).

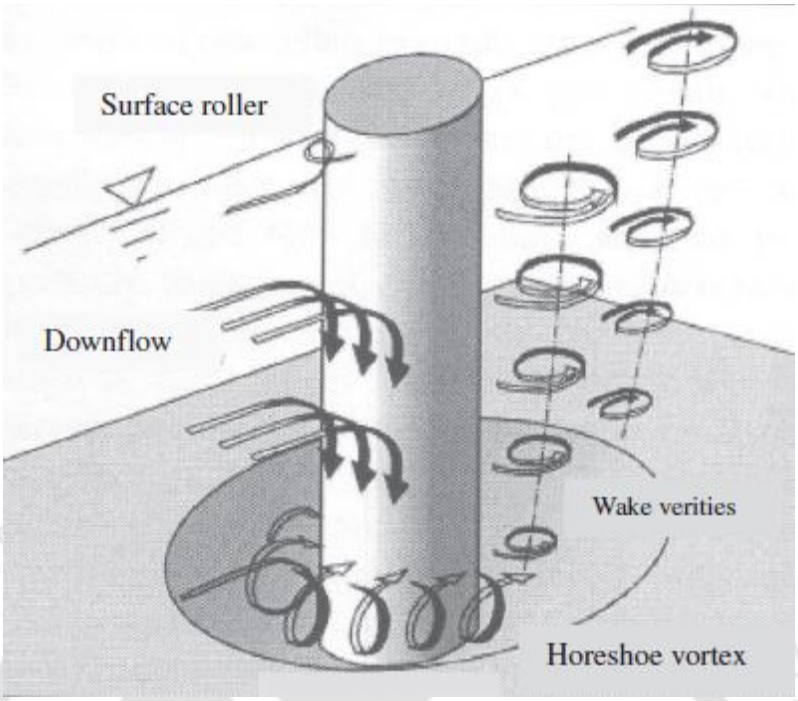

Figure 3.1 Flow and scour around a circular pier (Melville & Coleman, 2000)

Melville & Raudkivi (1977) studied the distribution of mean bed shear and turbulence intensity in a progressing scour hole and observed maximum bed shear stress in front of the pier during the initiation of local scour hole. Qadar (1981) found that the maximum scour depth is a function of sediment size and initial strength of the horseshoe vortex. Dey (1995) explored the three-dimensional velocity distribution in the scour hole region and detected the helical motion of flow around the cylinder. Ahmed & Rajaratnam (1998) analyzed the mean velocity profiles around the cylinder based on log law, defect law, and Clauser's scheme and also observed higher areas of bed shear stress amplification in the scour hole region. Graf & Istiarto (2002) observed stronger turbulent kinetic energy in the horseshoe vortex zone and behind the cylinder, compared to the approach flow. Muzzammil & Gangadhariah (2003) reported that the temporal mean size of the horseshoe vortex is independent of Reynolds number beyond 10^4 and only depends on the pier size. Dey & Raikar (2007) detected a core of high turbulence intensity and Reynolds stress in the scour hole region as compared to the downflow region. Kumar & Kothyari (2012) studied the mean turbulence parameters such as time-averaged velocity, turbulence intensity, and Reynolds shear stress in various radial planes around a cylinder. Das et al. (2013) reported that the circulation of horseshoe vortex is inversely

proportional to the flow shallowness and directly proportional to densimetric Froude number as well as Reynolds number. Quadrant analysis of Reynolds shear stress in front of the pier revealed that the horseshoe vortex zone is dominated by inward and outward interactions while the down-flow zone is dominated by sweep and ejection (Izadinia et al., 2013). Guan et al. (2019) studied the turbulence field around a cylinder in a developing scour hole and detected one primary vortex along with two distinct vortices in the local scour zone in front of the pier.

The effect of a mining pit on the flow characteristics around a bridge pier has not been explored previously. These effects are discussed in the following section.

3.2 Effect of a Mining Pit on Turbulent Flow Characteristics Around a Circular Pier

3.2.1 Experimental cases and data recording

For this study, two experimental cases were analyzed: (case 1) circular pier without any mining pit, and (case 2) with a trapezoidal mining pit 1.0 m upstream of the pier (Figure 3.2). For case 1, a circular pier of 75 mm diameter was inserted in the sand bed at 6.0 m from the downstream end of the channel. The pier diameter was kept smaller than 10 % of the width of the flume to eliminate the sidewall effects (Chiew & Melville, 1987). The flow was gradually supplied into the channel from the upstream entry until the required discharge was achieved with steady flow conditions. As soon as the flow was supplied to the channel, the local scouring was initiated. Local scouring is a time-dependent phenomenon, and hence the scour depth was recorded continuously using a Seatek® Ultrasonic ranging system (URS), which can record depth measurements at a temporal resolution of 0.50 seconds having a least count of 0.2 mm. Velocity measurements were taken once the equilibrium scour was achieved, i.e., the scour depth being recorded by the URS does not increase more than 1 mm in three hours (Kumar et al., 1999). Local scour reached equilibrium after about 18 hours. In the second case (case 2), a trapezoidal mining pit was excavated in the sand bed at the upstream side of the pier. The distance between the downstream edge of the mining pit and the pier was 1.0 m (Figure 3.2). Rest

of the flow conditions in the channel (i.e., discharge, flow depth, and flow velocity) were kept the same for both cases. Also, the ratio d/d_{50} was greater than 50 to ensure that the sediment size does not affect the scour depth (Chiew & Melville, 1987), where d is the pier diameter.

Various hydraulic parameters of the incoming flow upstream of the test zone for the experimental runs are provided in Table 3.1. The hydraulic conditions (discharge and flow depth) were maintained to attain fully turbulent flow under sub-critical conditions. Field measurements (Bathurst, 1985; Nikora & Smart, 1997) report a wide range of Froude's number for river flows (Fr = 0.1 – 0.8). In this context, we maintained moderate Froude number (Fr = 0.4 - 0.5). The flow was fully turbulent for the experimental cases, as the Reynolds number is greater than 10^4. Therefore, the viscous effects were limited to the laminar sub-layer in the near-bed region of the channel as well as the boundary layer around the circumference of the pier. Entrance length required to attain fully developed flow in the flume was calculated using the empirical equation proposed by (Zeng & Li, 2014):

$$L_u = 1.5 \frac{U}{\sqrt{-(u'w')_{max}}} h \tag{3.1}$$

where L_u is the adjustment length beyond which flow uniformity is attained, U is the average velocity, $-(u'w')_{max}$ is the maximum Reynolds stress in the flow, and h is the flow depth. Entrance length was found to be ~ 3.0 m; hence the experiment was conducted in the central portion of the channel to achieve fully developed flow conditions in the test zone.

Table 3.1 Hydraulic conditions of the experiments for the study of hydrodynamics around a circular pier

Case	Discharge (m^3/s)	Depth-averaged approach flow velocity (m/s)	Median particle size (mm)	Froude Number Fr	Reynolds number Re	Shear Reynolds number R^*
No Pit	0.0441	0.420	1.1	0.493	40951	92.06
With Pit	0.0441	0.420	1.1	0.493	40951	92.06

Recordings of the instantaneous velocities were done at six different locations as well as at the upstream and downstream edges of the pit to sufficiently capture the flow characteristics. Details of these locations are shown in Figure 3.2. Location 1 was at the pit center (1.16 m upstream of the pier center); location 2 was 0.5 m upstream of the pier center and represented a location where the flow passed over the mining pit and was approaching towards the pier. Locations 3, 4, 5, and 6 were in close proximity to the pier, and they were inside the radius of the scour hole.

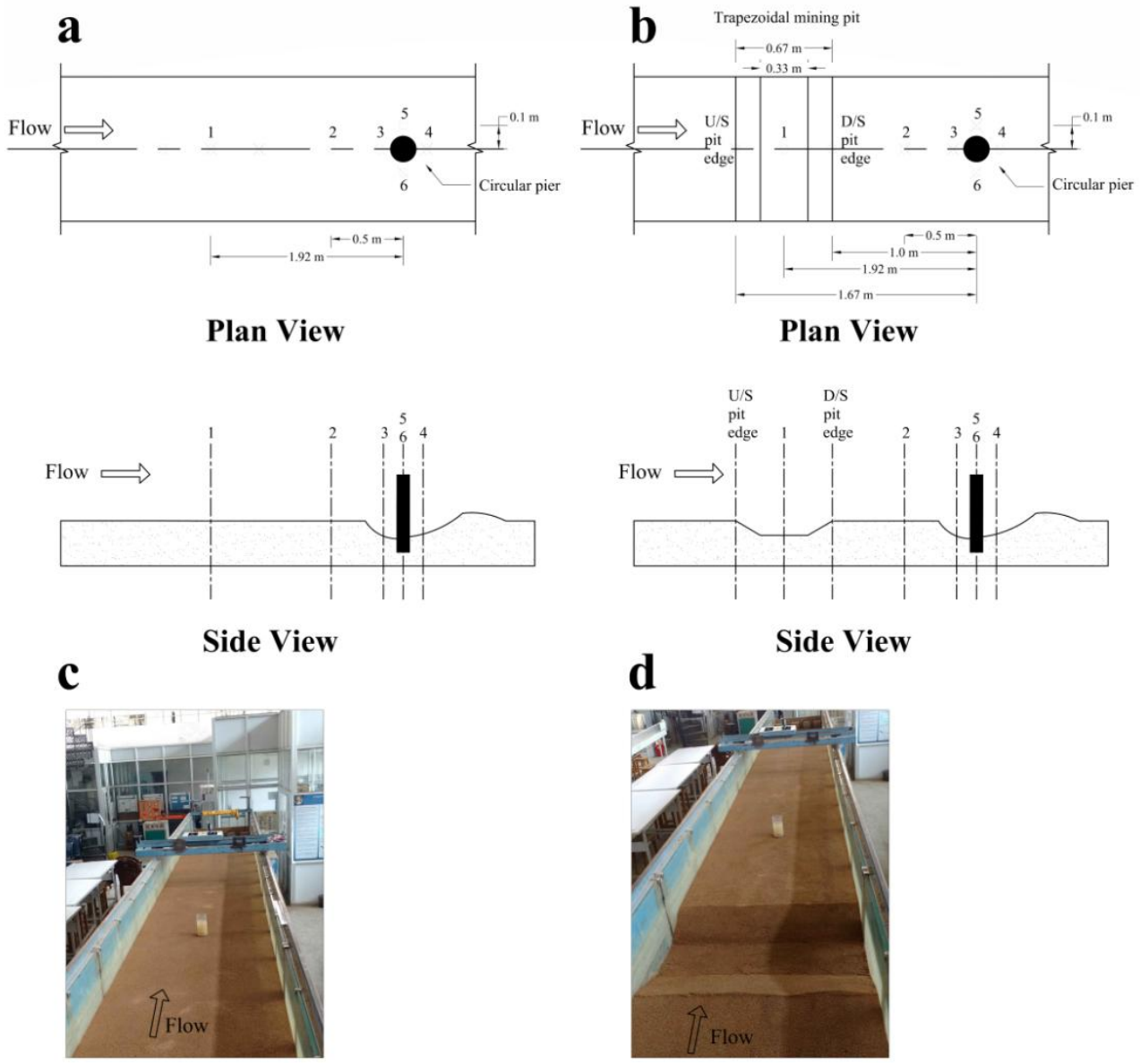

Figure 3.2 Details of data recording locations for (a) Case 1 – Without pit, (b) Case 2 – With pit; Snapshots of test cases (c) Case 1 – Without pit, (d) Case 2 – With pit.

Location 3 and 4 were at 0.1 m to the front and rear side of the pier, respectively, whereas locations 5 and 6 were 0.1 m to the left and right side of the pier, respectively. For both the experimental cases, the commencement of the velocity recording was done after the desired steady flow conditions (flow discharge and depth) as well as equilibrium scour was attained in the channel.

Velocity data captured using an ADV may sometimes be contaminated with spikes as the phase shift between transmitted and received signals may lie beyond the preset range, or there may be some interference of previous signals reflected from complex boundaries. Decontamination of the velocity data was actualized with the help of the acceleration threshold method (Goring & Nikora, 2002). By trial and error sequences, the appropriate value of the acceleration threshold was adopted between a range of 1 to 1.5 (Deshpande & Kumar, 2016). Decontamination was carried out in a manner to achieve -5/3 slope of velocity power spectra in the inertial sub-range. The power spectra for unfiltered as well as filtered signals are shown in Figure 3.3. Turbulence statistics for both cases (i.e., without mining pit and with mining pit) are presented here for experiments with discharge value Q = 0.0441 m^3/s.

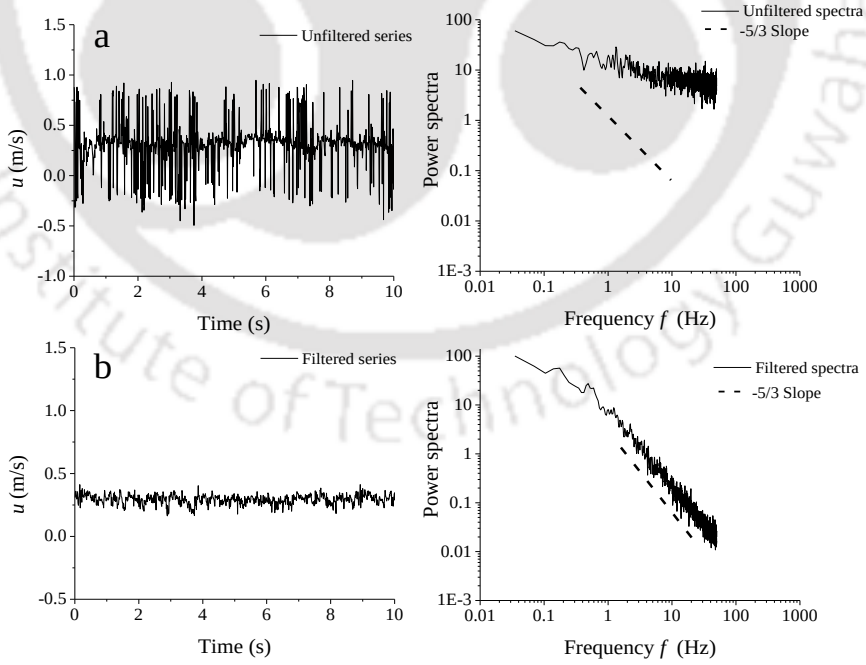

Figure 3.3 Velocity time series and power spectra for (a) Unfiltered series (b) Filtered series.

3.2.2 Mean streamwise velocity profiles

Time-averaged velocities were calculated by

$$\bar{u} = \frac{1}{n}\sum_{i=1}^{n} u_i \; ; \; \bar{w} = \frac{1}{n}\sum_{i=1}^{n} w_i \tag{3.2}$$

where, n represents the number of samples. Figure 3.4 provides the profiles of mean streamwise velocities at Locations 1-6.

At measurement Location-1, which is at the pit center, the velocity profile in the case of a mining pit deviates as compared to the no-pit condition. As the incoming flow enters the pit, it is subjected to a sudden rise in hydrostatic pressure due to which flow separation occurs. Reversal of mean streamwise velocity can be observed in the bottom boundary region (z/h ~ 0.2) at the pit center (Location-1). The flow erodes the downstream edge of the pit and flows towards the pier. This results in increased flow depth at the downstream edge of the pit and a substantial drop in the mean velocities, as compared to without pit condition [Figure 3.4(a)]. Velocity profiles at the upstream and downstream edges show deviation from the logarithmic profile. As this flow moves past the pit towards the pier, the initial bed level is recovered, and therefore the flow is subjected to a negative pressure gradient. Hence, the flow is spatially accelerated as it moves towards the pier. Therefore the mean velocities of the flow approaching towards the pier (Location-2) are found to be slightly higher as compared to without pit case. About a 10% rise in the near-bed streamwise velocities is observed at this location (Figure 3.4b).

Locations 3, 4, 5, and 6 lies within the scour hole, and they are in proximity to the pier. In front of the pier (Location-3), flow interacts with the pier and moves vertically downward due to stagnation. Flow reversal occurs at the pier base inside the scour hole (below z/h ~ 0.15), which can be observed in Figure 3.4(c). This indicates the presence of a horseshoe vortex at the pier base. The average magnitude of negative velocities in this reversal zone is about 15% greater in the presence of a mining pit. The strength of the horseshoe vortex depends upon the magnitude of reversal flow velocities (Chiew & Melville, 1987); thus, a stronger horseshoe vortex is formed in the presence of a mining pit. Therefore, mining operations can cause greater scour depth as it is primarily a function of the strength of horseshoe vortex.

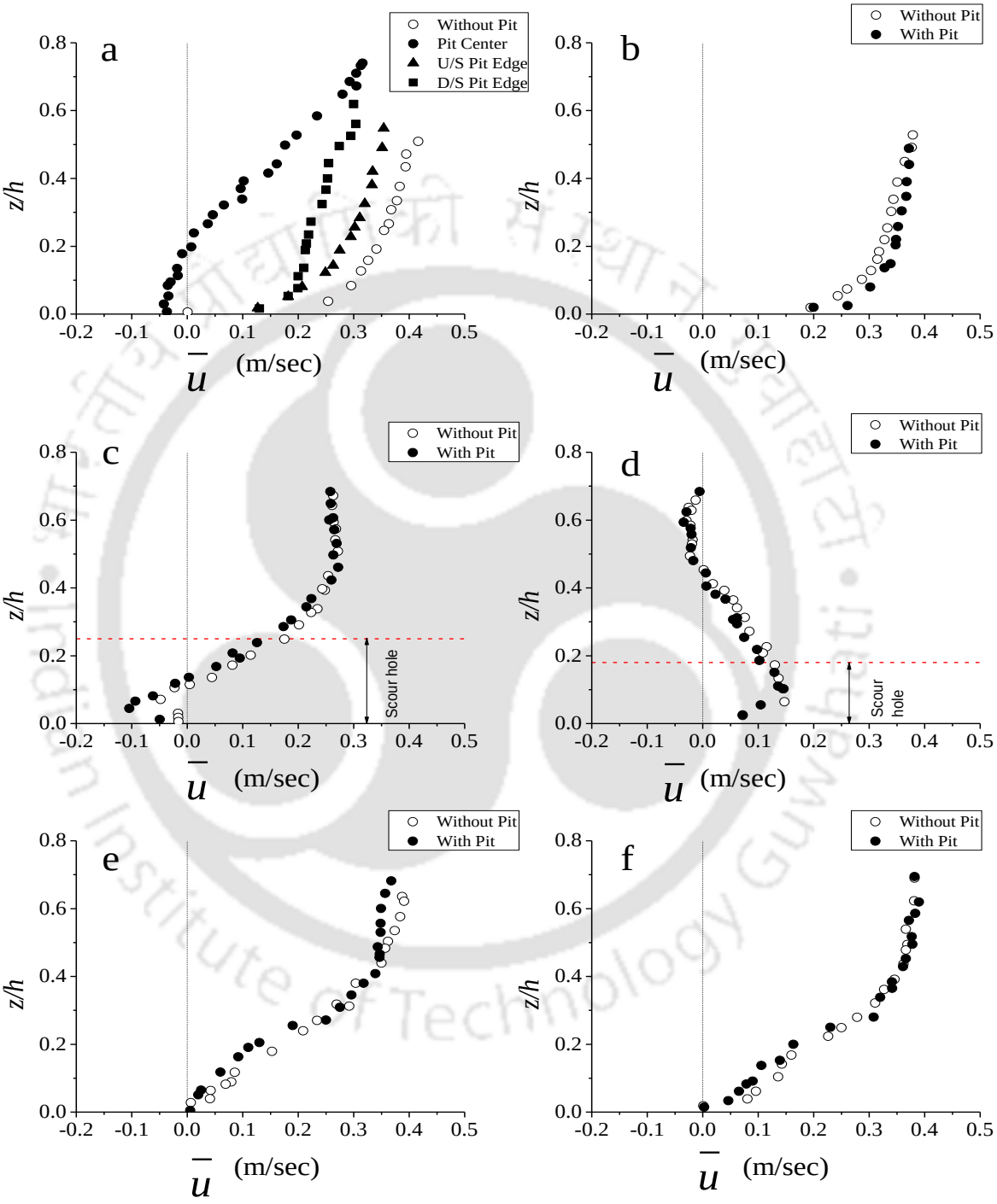

Figure 3.4 Mean streamwise velocity profiles at (a) Location-1, (b) Location-2, (c) Location-3, (d) Location-4, (e) Location-5, and (f) Location-6 around a circular cylinder.

As the flow moves past the pier, wake vortices are shed at the rear side of the pier (Location-4). Therefore, the velocity profile at the rear side of the pier is negative from z/*h* ~ 0.7 to *z*/*h* ~ 0.5 for both cases [Figure 3.4(d)]. Below this depth, flow reattachment occurs, and positive mean velocities are observed. The velocity profiles at this location are nearly similar for both cases, with a slight decrease in the velocities below *z*/*h* ~ 0.5, in the presence of a pit. The mean streamwise velocity profiles at the front and rear side of the pier (Location-3 and Location-4, respectively) are in agreement with the previous studies (Graf & Istiarto, 2002; Kumar & Kothyari, 2012). At Locations 5 and 6, velocity profiles are positive throughout the depth in the no-pit condition. At these locations, velocity profiles in the case of a mining pit are similar to those obtained for the no-pit case, with a slight decrease (~ 4%) in the average magnitude.

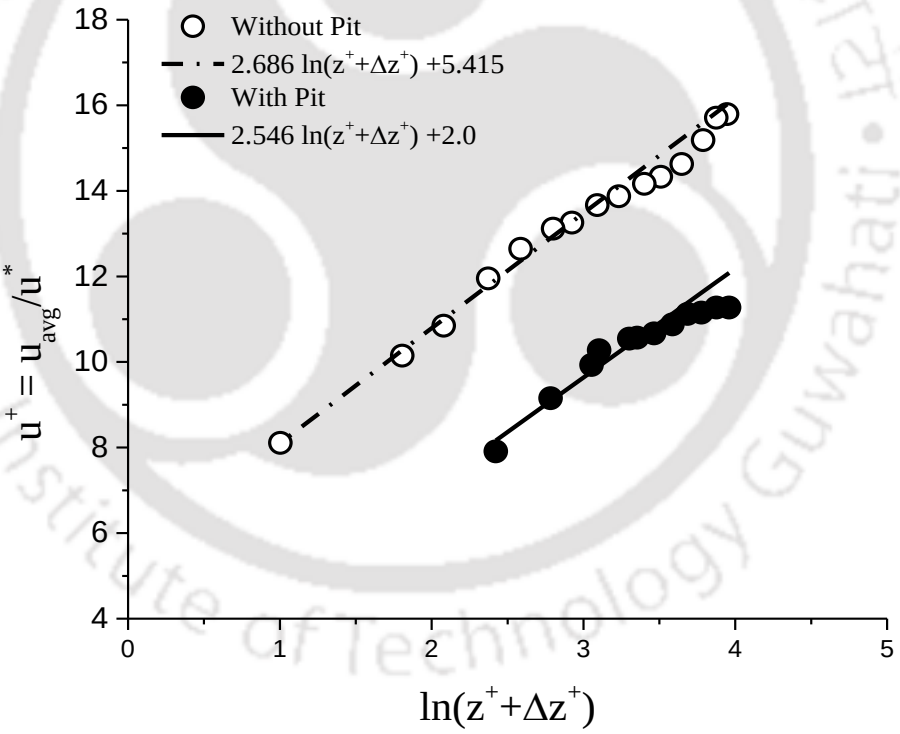

Figure 3.5 Modified log-law for the velocity profiles at the approaching flow (Location-2) towards a circular pier.

In accordance with the study carried out by Deshpande & Kumar (2016), the execution of modified log law in the inner layer (z/h < 0.2) for velocity profiles of the flow approaching the pier (Location-2) is presented (Figure 3.5). A non-dimensional expression for the log-law can be given as:

$$\frac{u}{u_*} = \frac{1}{\kappa} ln\left(\frac{z^+ + \Delta z^+}{\xi^+}\right) \tag{3.3}$$

where $z^+ = z/d_{50}$, $\Delta z^+ = \Delta z/d_{50}$, Δz is the depth of the virtual bed level, $\xi^+ = z_0/d_{50}$, z_0 is the zero velocity level, and κ is the Von Karman's constant on Karman's constant. The values of von Karman's constant, depth of virtual bed level, and zero velocity level were found to be 0.37, 1 mm, and 0.15 mm, respectively, for the no-pit condition and 0.39, 10 mm, and 0.5 mm, respectively, in case of a mining pit. The value of κ is found to be less than the universal value, i.e., 0.41 for both cases, which is in conformance with the previous literature on the flows over mobile beds (Deshpande & Kumar, 2016; Dey et al., 2012).

3.2.3 Bed shear stress

Bed shear stress is instrumental in governing the erosion downstream of a mining pit. It can be represented in the form of shear velocity: u_* which is $\sqrt{\tau_0/\rho}$ (τ_0 is the bed shear stress and ρ is the mass density of water). The evaluation of bed shear stress through the turbulent kinetic energy (*TKE*) method is based on the proportionality of the *TKE* to the bed shear stress (Soulsby & Dyer, 1981; Stapleton & Huntley, 1995).

$$\begin{aligned} &\tau_0 = C_1 * TKE\ ; \\ &TKE = \frac{1}{2}\,\rho\left(\overline{u'u'} + \overline{v'v'} + \overline{w'w'}\right) \end{aligned} \tag{3.4}$$

where, *TKE* is the turbulent kinetic energy, while u', v', and w' are the fluctuating components of the velocity in the streamwise, lateral, and vertical directions, respectively. The value of C1 has been adopted as 0.19 by various researchers (Stapleton & Huntley, 1995; Thompson et al., 2003) for a variety of flows. The *TKE* method has

been used for the estimation of the bed shear stress in the present study since it is persistent and robust. The values of bed shear stresses are presented in Table 3.2.

Table 3.2 Bed shear stresses computed around the circular pier using the *TKE* method

Location	Shear Velocity (m/s)		Bed shear stress (N/m²)	
	No Pit	With Pit	No Pit	With Pit
Location 1	0.014	0.024	0.21	0.59
Location 2	0.026	0.033	0.70	1.11
Location 3	0.023	0.030	0.53	1.01
Location 4	0.034	0.046	1.22	2.14
Location 5	0.025	0.027	0.62	0.73
Location 6	0.028	0.029	0.78	0.84

It can be observed from Table 3.2 that the bed shear stress at all the locations was higher in the case of a mining pit. When the flow passed over the pit, the bed upstream of the pier (Location-2) was subjected to ~ 26% higher bed shear as compared to the no-pit condition. Bed shear stresses in the scour hole (locations 3, 4, 5, and 6) were also higher in the case of a mining pit. Thus, it is evident that the flow exerts greater shear on the streambed after passing over a pit.

3.2.4 Reynolds shear stress (RSS)

Reynolds shear stresses (RSS) are exerted on the *X*-*Y* plane (parallel to the flow direction) due to the momentum transport across the depth across this plane. Streamwise Reynolds shear stress and lateral Reynolds shear stress are evaluated as $-\rho\overline{u'w'}$ and $-\rho\overline{v'w'}$ respectively. The variations of streamwise RSS with non-dimensional flow depth (z/h) at Locations 1 – 6 are presented in Figure 3.6.

At Location-1 [Figure 3.6(a)] for without pit case, the RSS increases from a measurement height of z/h ~ 0.7 to z/h ~ 0.2, below which damping in the streamwise RSS values is observed. When the flow approaches the pit (with-pit case), the streamwise RSS at the upstream edge of the pit is similar to without pit case. However, when the flow enters the

pit, streamwise RSS magnitudes are very high at the pit center [Figure 3.6(a)] as compared to without pit case indicating excess transport of momentum along with the depth.

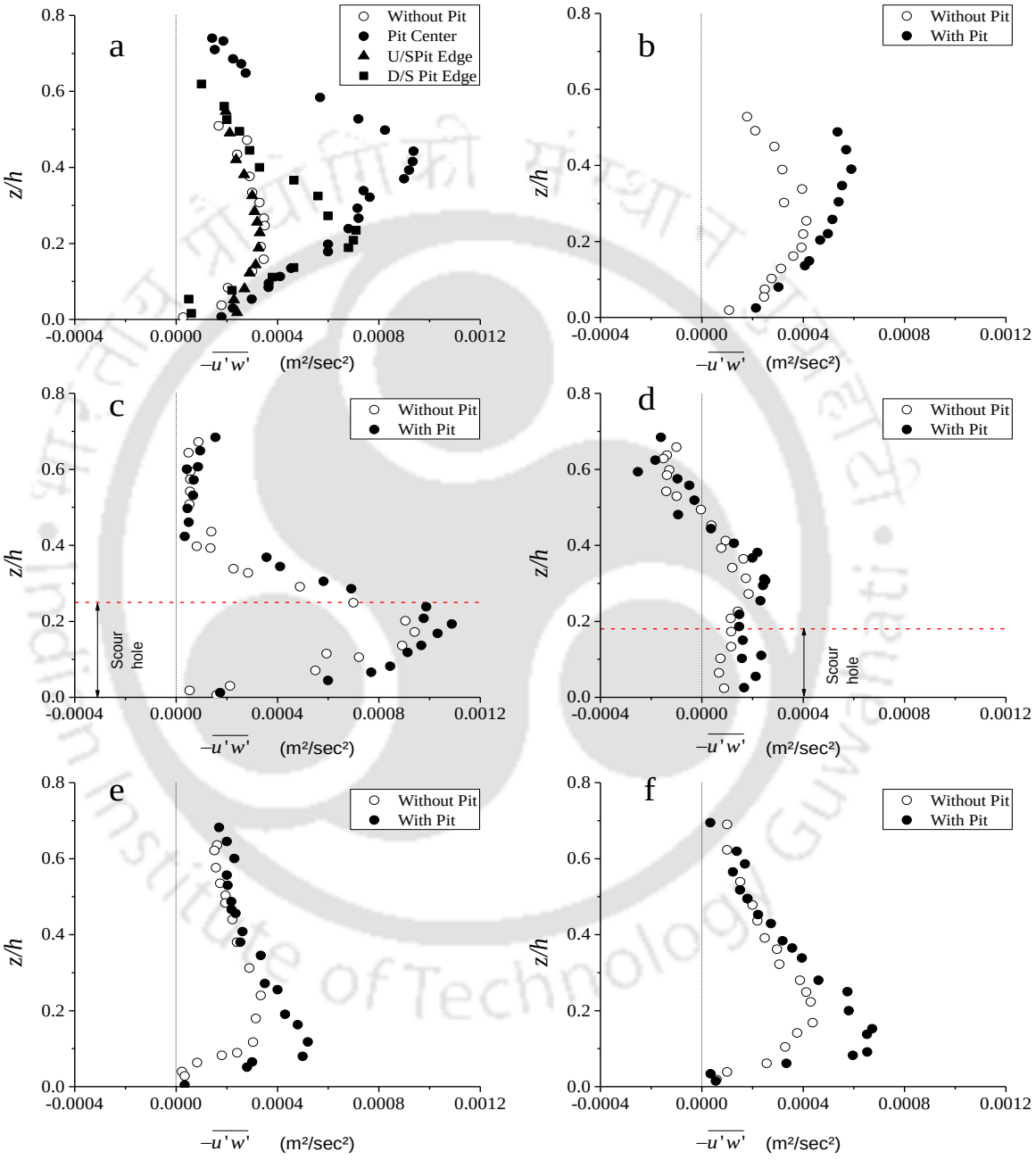

Figure 3.6 Streamwise Reynolds shear stress profiles at (a) Location-1, (b) Location-2, (c) Location-3, (d) Location-4, (e) Location-5, and (f) Location-6 around the circular pier.

Also, damping of the RSS profile at the pit center is observed at z/h ~ 0.4. Thus, excavating a mining pit can be viewed as a source of turbulence to the flow which is approaching the pier. At the downstream edge of the pit, the magnitude of the streamwise RSS values also shows a significant rise. After passing over the pit, as the flow moves towards the pier (Location-2), the damping of RSS is observed at z/h ~ 0.4, which is higher than that observed for without pit case (z/h ~ 0.2). Also, there is about a 30% increase in the magnitude of maximum RSS at this location. Hence, excavation of a pit results in higher turbulent shear stresses in the flow downstream of the pit.

At the front side of the pier (Location-3), streamwise RSS is very low in the down-flow zone between z/h ~ 0.7 to z/h ~ 0.4, while higher stresses are concentrated inside the scour hole at the pier base [Figure 3.6(b)]. In the presence of a mining pit, the RSS profile in front of the pier is similar to the no-pit case, with a nearly 10% rise in RSS magnitudes inside the scour hole. At the rear side of the pier (Location-4), the streamwise RSS profile is negative in the separation zone (z/h ~ 0.7 to z/h ~ 0.5), below which the profile is positive and nearly constant for the no-pit case [Figure 3.6(d)]. This indicates the dominance of inward and outward interactions in the separation zone at the rear side of the pier, contrary to the straight flows. At this location, the RSS profile in the presence of a mining pit is also similar to the no-pit case, with a slight (~ 10%) rise in the near-bed region. At the left and right sides of the pier (Locations 5 and 6, respectively), RSS profiles for both cases are similar, with a ~15% rise in the magnitudes of maximum RSS because of the presence of a mining pit.

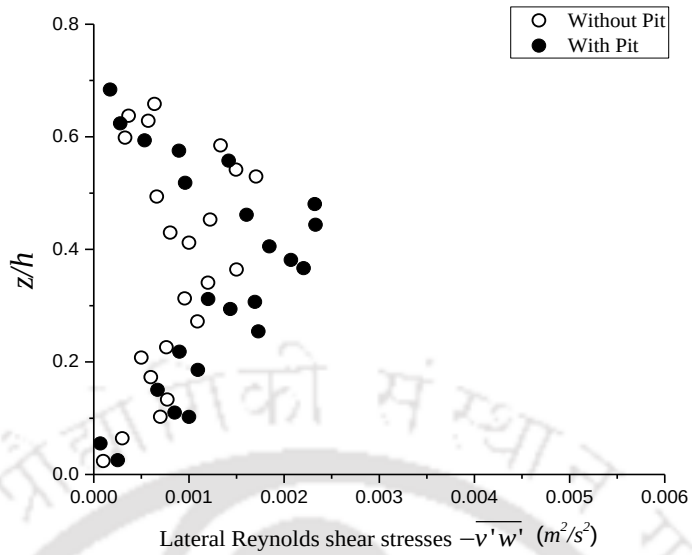

Figure 3.7 Lateral Reynolds shear stress profile at the rear side of the circular pier (Location-4).

At the rear side of the pier, the lateral velocity fluctuations become dominant because of vortex shedding. Therefore lateral RSS are more significant than the streamwise RSS (Figure 3.7). The peak values of lateral RSS are observed in the zone of flow reattachment (z/h ~ 0.45). A rise of about 20% is observed in the lateral RSS values in the presence of an upstream mining pit. Thus, the interaction of the flow with the pier after passing over a pit causes excess lateral turbulent stresses behind the pier.

3.2.5 Reynolds normal stress (RNS)

Reynolds normal stress (RNS) is defined as the root mean square of the second moment of velocity fluctuations, given by the expression: $\sigma = (\overline{u'_i u'_i})^{0.5}$, where u'_i is the fluctuating component of velocity in i^{th} direction. It is also known as turbulent intensity, as it represents the magnitude of fluctuations. Distribution of Streamwise turbulent intensity (σ_u) and vertical turbulent intensity (σ_w) along with depth at sections 1 - 4 is shown in Figure 3.8.

$$\sigma_u = (\overline{u'u'})^{0.5}$$
$$\sigma_w = \left(\overline{w'w'}\right)^{0.5} \quad (3.5)$$

Due to the excavation of a pit, a high streamwise turbulence intensity zone [Figure 3.8(a)] occurs in the upper flow layer (z/h ~ 0.4 – 0.7) at the pit center (Location-1) as compared to the without pit case in which the zone is in the near-bed region (z/h ~ 0.1). Vertical turbulence intensities [Figure 3.8(b)] throughout the measurement depth at the pit center are significantly higher due to the presence of a mining pit at this location. After passing over the pit, flow approaching the pier (Location-2) has 15% higher σ_u in the near-bed region [Figure 3.8(c)], whereas σ_w is higher throughout the depth as compared to the without-pit case [Figure 3.8(d)].

In front of the pier [Figures 3.8(e) and 3.8(f)], σ_u magnitudes are higher in the down-flow zone in the presence of a pit. Inside the scour hole at the pier base, σ_u magnitudes have decreased while σ_w magnitudes have increased in the presence of a pit. at the rear side of the pier [Figures 3.8(g) and 3.8(h)], the profiles of σ_u and σ_w are similar for both cases, with about a 10% increase in magnitudes as compared to their corresponding values for the without pit case. The turbulence intensity profiles observed at the front and rear sides of the pier are similar to the previous studies (Graf & Istiarto, 2002; Kumar & Kothyari, 2012).

Thus, flow passing through a dredged pit has greater turbulence intensities, and interaction of such flow with a pier causes greater turbulence intensities, especially in the down-flow zone at the pier front as well as at the rear side of the pier.

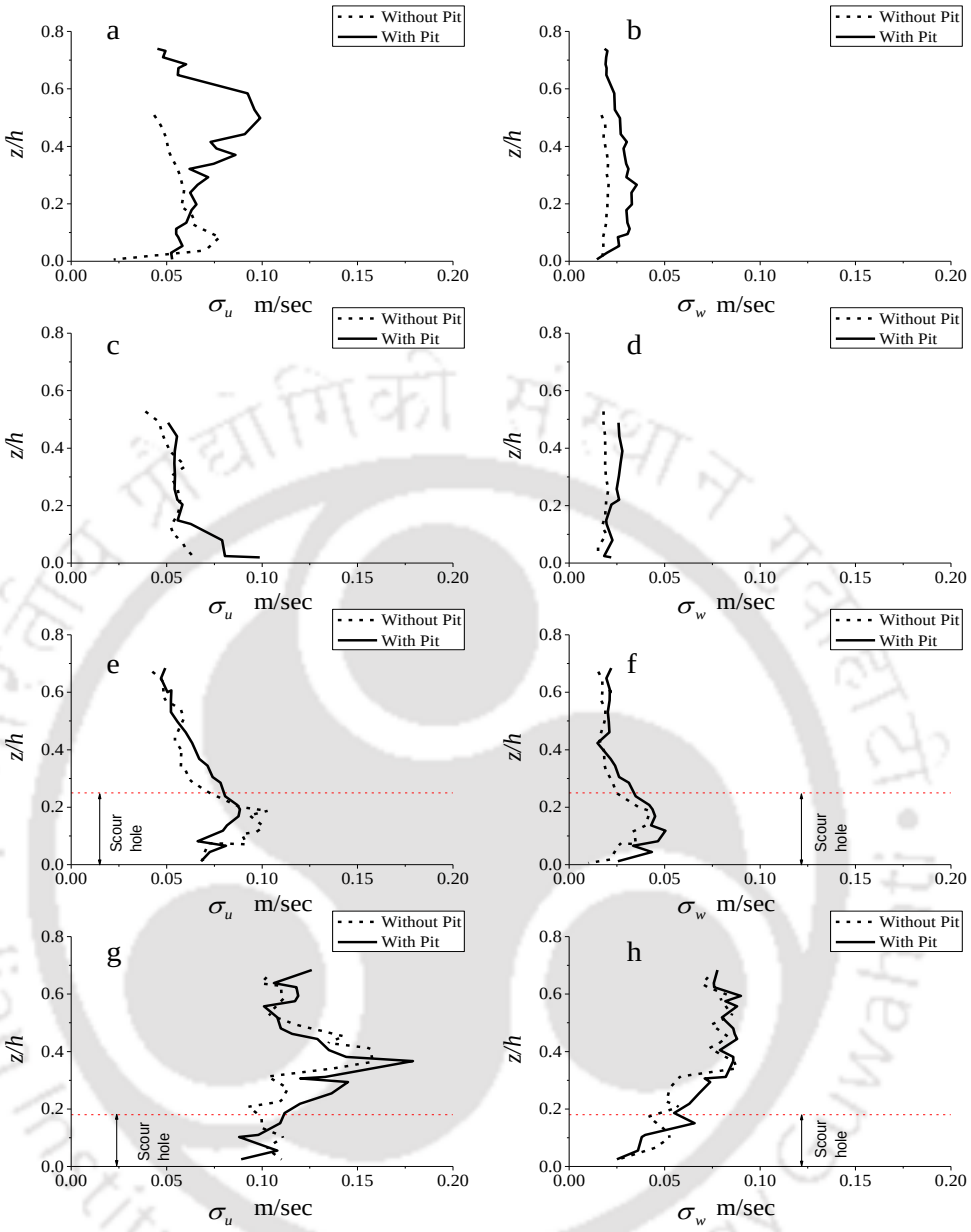

Figure 3.8 Streamwise turbulence intensity profiles at (a) Location-1, (c) Location-2, (e) Location-3 and (g) Location-4, and vertical turbulence intensity profiles at (b) Location-1, (d) Location-2, (f) Location-3 and (h) Location-4 around the circular pier.

3.2.6 Turbulent kinetic energy, turbulent viscosity and mixing length of the approach flow

Nature of turbulence of the incoming flow towards the pier past a mining pit (Location-2) is analyzed in this section on the basis of previous empirical equations for straight flows.

Turbulent kinetic energy (*TKE*) has been calculated by Equation 3.6 for both cases at Location-2 (Figure 3.9). Nezu and Nakagawa (1993) provided a semi-theoretical equation for turbulent energy distribution along with the depth as:

$$\frac{TKE}{{u_*}^2} = D_K exp(-2C_K\, z/h) \tag{3.6}$$

Where D_K and C_K were obtained as 4.72 and 1, respectively, from the flume experiments by Nezu and Nakagawa (1993). The average turbulent energy is about 15% greater when the flow passes over the pit. The experimental data fairly follows Equation 3.6 for both cases.

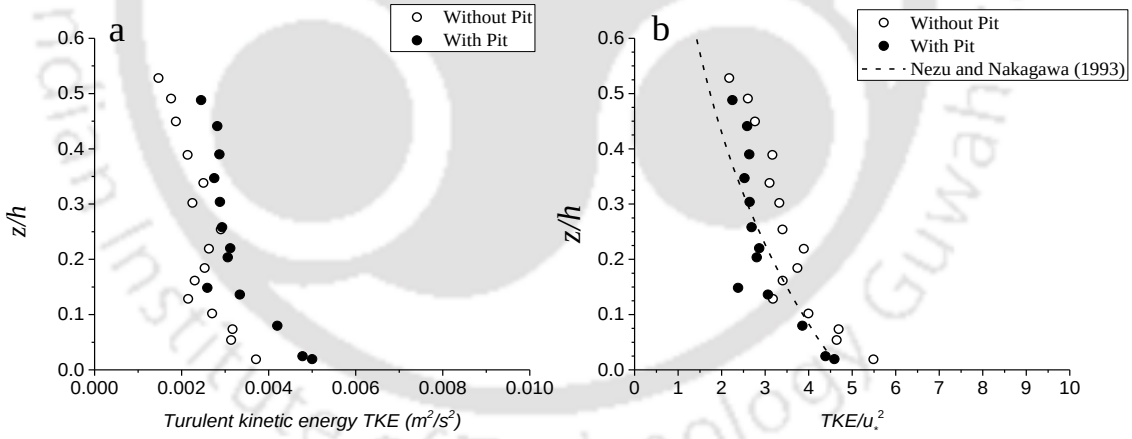

Figure 3.9 Distribution of (a) Turbulent kinetic energy, and (b) Normalized turbulent kinetic energy along with the depth at Location-2 for the circular pier.

The turbulent viscosity (ν_T) is significant in terms of Reynolds stresses and is given by Equation 3.7. Nezu and Nakagawa (1993) provided a semi-theoretical equation for turbulent viscosity based on the log-law (Equation 3.8). The variation of normalized turbulent viscosity at Location-2 along the flow depth is given in Figure 3.10.

$$\nu_T = \frac{\overline{-u'w'}}{(dU/dz)} \tag{3.7}$$

$$\nu_T = \kappa u_* z(1 - z/h) \tag{3.8}$$

It can be observed that turbulent viscosity for both cases is similar in the inner layer (below z/h ~ 0.2). However, the turbulent viscosity is greater in the outer layer (above z/h ~ 0.2) in the presence of a pit. The experimental data is comparable to the values calculated by Equation 3.7. But in the upper flow zone (above z/h ~ 0.2), especially in the presence of a pit, the viscosity values are greater as compared to the semi-theoretical equation. This deviation may be due to the excess momentum transport due in the flow after passing over the pit.

Mixing length (l) is calculated by Equation 3.9 as it is the average distance which an eddy travels before changing its momentum in the surrounding fluid. The experimental data at Location-2 is compared with Equation 3.10 given by Nezu and Nakagawa (1993) and presented in Figure 3.11.

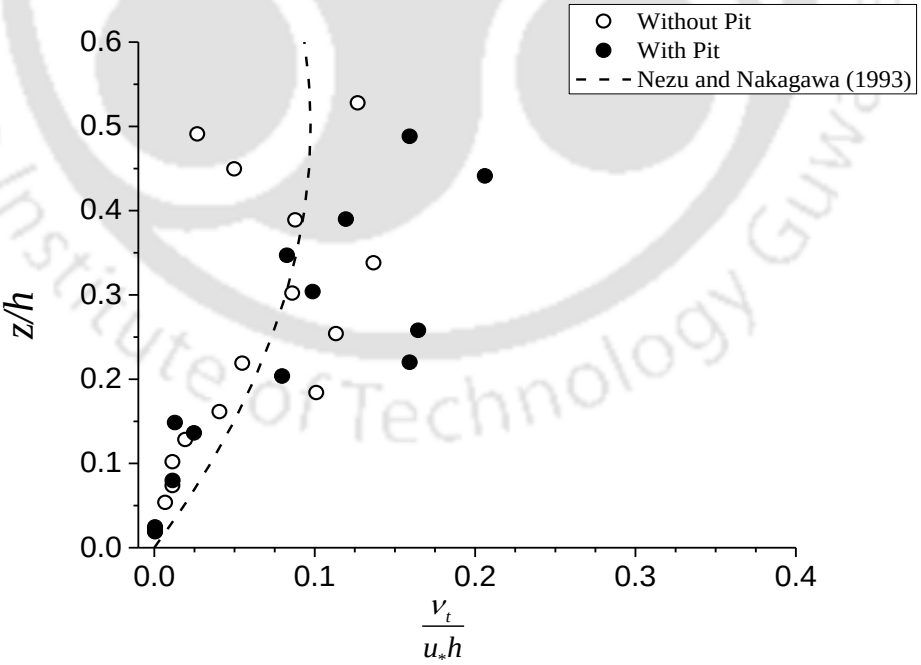

Figure 3.10 Distribution of normalized eddy viscosity along with the depth at Location-2 of the circular pier

$$l = \frac{\left(\overline{-u'w'}\right)^{0.5}}{(dU/dz)} \tag{3.9}$$

$$\frac{l}{h} = \frac{\kappa z}{h(1 - z/h)^{0.5}} \tag{3.10}$$

The experimental data reasonably follows Equation in the inner layer (below z/h ~ 0.2) for both cases. Dispersion is observed in the experimental data above z/h ~ 0.2, and higher values of mixing lengths are observed in the presence of a mining pit.

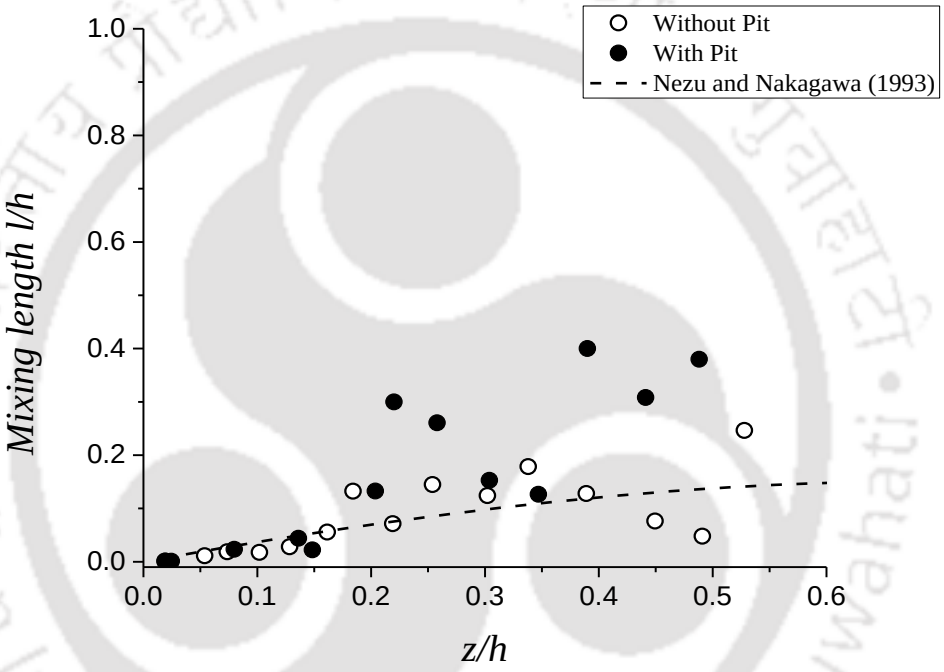

Figure 3.11 Distribution of normalized mixing length along with the depth at Location-2 of a circular pier

3.2.7 Turbulent kinetic energy flux

Flux of the turbulent kinetic energy in the streamwise (F_{TKEu}) and vertical (F_{TKEw}) directions can be represented by the following equations (Krogstad & Antonia, 1999; Raupach, 1981):

$$F_{TKE_u} = \frac{3}{4}\frac{\left(\overline{u'^3} + \overline{u'w'^2}\right)}{{u_*}^3} \tag{3.11}$$

$$F_{TKE_w} = \frac{3}{4}\frac{\left(\overline{w'^3} + \overline{w'u'^2}\right)}{{u_*}^3} \tag{3.12}$$

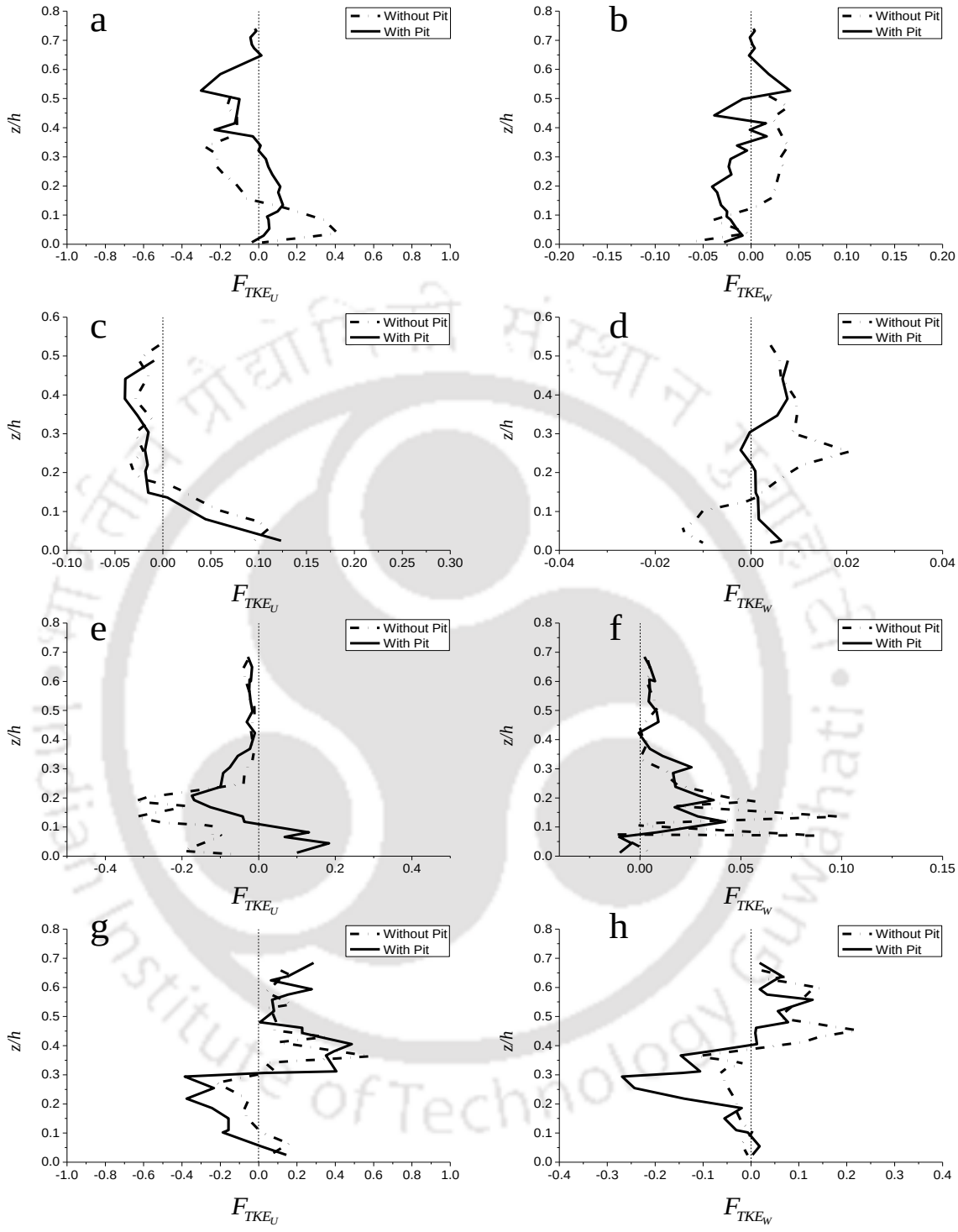

Figure 3.12 Distributions of the streamwise *TKE* flux at (a) Location 1, (c) Location 2, (e) Location 3, (g) Location 4, and vertical *TKE* flux at (b) Location 1, (d) Location 2, (f) Location 3, and (h) Location 4 around the circular pier.

Distributions of the turbulent kinetic energy fluxes along z/h at Locations 1-4 are shown in Figure 3.12. At Locations 1 and 2 [Figures 3.12(a) and 3.12(b)] for without pit case, the F_{TKEu} starts with a small positive value near the bed and becomes negative for the rest of the depth from $z/h \sim 0.15$, while F_{TKEw} starts with a minuscule negative value close to the bed and then changes its sign from $z/h \sim 0.12$, which is conforming to the previous literature (Deshpande & Kumar, 2016). In the presence of a pit, the streamwise *TKE* flux at the pit center (Location-1) is positive, i.e., in the streamwise direction from bed surface up to $z/h \sim 0.35$ and then becomes opposite to the flow direction for the rest of the measurement depth [Figure 3.12(a)].

It can be observed from Figure 3.12(b) that at Location-1, pit excavation causes the vertical *TKE* flux (F_{TKEw}) to travel in the downward direction from bed surface up to a height $z/h \sim 0.5$, and then in the upward direction above it. At Location-2 [Figures 3.12(c) and 3.12(d)], F_{TKEu} in the presence of a pit is nearly similar to the without pit case, except that it crosses from positive to negative at $z/h \sim 0.11$. Whereas, F_{TKEw} starts from a small positive value close to the bed and remains nearly constant for the entire measurement depth.

At the pier front (Location-3) for the without pit case [Figure 3.12(e)], the F_{TKEu} starts from a small negative value near the bed, and its magnitude increases rapidly up to $z/h \sim 0.2$, and then the value is nearly constant above this depth. The F_{TKEw} at this location for the without-pit case [Figure 3.12(f)] is positive in the horseshoe vortex zone at the base of the pier, and the magnitude increases slightly up to $z/h \sim 0.15$, and the values are nearly constant above it. This indicates that at the front side of the pier, the streamwise *TKE* flux is opposite to the flow direction for the entire depth and is concentrated in the scour hole region (from bottom boundary up to $z/h \sim 0.25$). Here, vertical turbulent kinetic energy flux is in the upward direction for the entire depth, but it is concentrated only at the pier base inside the scour hole (from bed surface up to $z/h \sim 0.25$). At this location, pit excavation causes the streamwise *TKE* flux [Figure 3.12(e)] to travel in the flow direction in the horseshoe vortex zone (up to $z/h \sim 0.1$), and above this depth, it travels opposite to the flow direction with lower negative magnitudes than the without pit case. Also, the

vertical *TKE* flux is in the downward direction in the near-bed region ($0 < z/h < 0.08$), and above it, the flux is in the upward direction [Figure 3.12(f)].

At the rear side of the pier (Location-4) for the without pit case, F_{TKEu} [Figure 3.12(g)] values have small positive magnitudes very near to the bed surface inside the scour hole (up to $z/h \sim 0.1$). Above $z/h \sim 0.1$, F_{TKEu} becomes negative up to the depth $z/h \sim 0.3$, and beyond this depth, it changes its sign to positive. On the other hand, F_{TKEw} at this location [Figure 3.12(h)] is negative in the near-bed region up to the depth $z/h \sim 0.4$, and above this depth, it is positive for without pit case. For the case of a mining pit, the profiles of F_{TKEu} and F_{TKEw} at this location (Location-4) are similar to those obtained for the without pit case with some difference in the magnitudes. The streamwise *TKE* flux has higher negative values (opposite to the flow direction) in the near-bed zone up to a depth $z/h \sim 0.3$, while vertical *TKE* flux also has higher negative values in the near-bed zone up to a depth $z/h \sim 0.4$, as compared to the without pit case.

3.2.8 Quadrant analysis

At any point in the flow, the velocity fluctuations u' and w' can be plotted on a $u'w'$ plane with four quadrants (lu & Willmarth, 1973). These four quadrants represent four different types of bursting events, namely: (1) Outward interactions$(u' > 0,\ w' > 0)$; (2) Ejections $(u' < 0,\ w' > 0)$; (3) Inward interactions $(u' < 0,\ w' < 0)$, and (4) Sweeps $((u' > 0,\ w' < 0)$. The total Reynolds shear stress at a point is the summation of all four types of bursting events. Further, a hyperbolic hole region (H) is introduced on the $u'w'$ the plane, given by: $|u'w'| = H(\overline{u'u'})^{0.5}(\overline{w'w'})^{0.5}$. The difference between strong and weak events can be understood using smaller values of H while larger values of H are used to estimate the contribution of only stronger events among all four types of bursting events to the total *RSS* production. At any point, the contribution from a quadrant i to the total *RSS* outside the hyperbolic hole region can be given by :

$$\langle u'w' \rangle_{i,H} = \lim_{T\to\infty} \frac{1}{T} \int_0^T u'(t)w'(t)\lambda_{i,H}(z,t)dt \tag{3.13}$$

Where $\lambda_{i,H}(z,t)$ is called a detection function defined as:

$$\lambda_{i,H}(z,t) = 1, \text{ if } u'w' \text{ is in quadrant } i \text{ and if } |u'w'| \geq H(\overline{u'u'})^{0.5}(\overline{w'w'})^{0.5}$$
$$\lambda_{i,H}(z,t) = 0, \text{otherwise} \tag{3.14}$$

The relative contribution by each type of the event to the total RSS production can then be estimated by:

$$S_{i,H} = \frac{\langle u'w' \rangle_{i,H}}{\overline{u'w'}} \tag{3.15}$$

This implies that for i = 2 and 4 (ejection and sweep events), the value of the fractional contribution $S_{i,H}$ shall be positive, while it shall be negative for i = 1 and 3 (outward and inward interactions). Also, the summation of $S_{i,H}$ for all four types of bursting events shall be 1. The contribution of bursting events for the hole size H = 0 along with the depth at sections 1, 2, 3, and 4 have been quantified in Figure 3.13.

The probability of occurrence $P_{i,H}$ of the bursting events can be calculated by:

$$P_{i,H} = \frac{\langle u'w' \rangle_{i,H}}{\sum[\langle u'w' \rangle_{1,H} + \langle u'w' \rangle_{2,H} + \langle u'w' \rangle_{3,H} + \langle u'w' \rangle_{4,H}]} \tag{3.16}$$

Occurrence probability plots of the bursting events along with the depth at Locations 1, 2, 3, and 4 are presented in Figure 3.14.

At Locations 1 and 2 [Figure 3.13(a) and 3.13(c); Figure 3.14(a) and 3.14(c)] in the absence of a mining pit, contribution towards the *RSS* production is dominated by the ejection and sweep events, as well as the frequency of these events is higher throughout the depth, which is in agreement with the findings made by (Nakagawa & Nezu, 1977). At the pit center [Figure 3.13(b)], input from the ejection and sweep events is higher than inward and outward ejection events. However, the frequency of occurrence of these events is altered. In the case when a mining pit is present [Figure 3.14(b)], the probability of occurrence of ejection events rises by ~ 15% in the flow layer from bed surface up to z/h ~ 0.3.

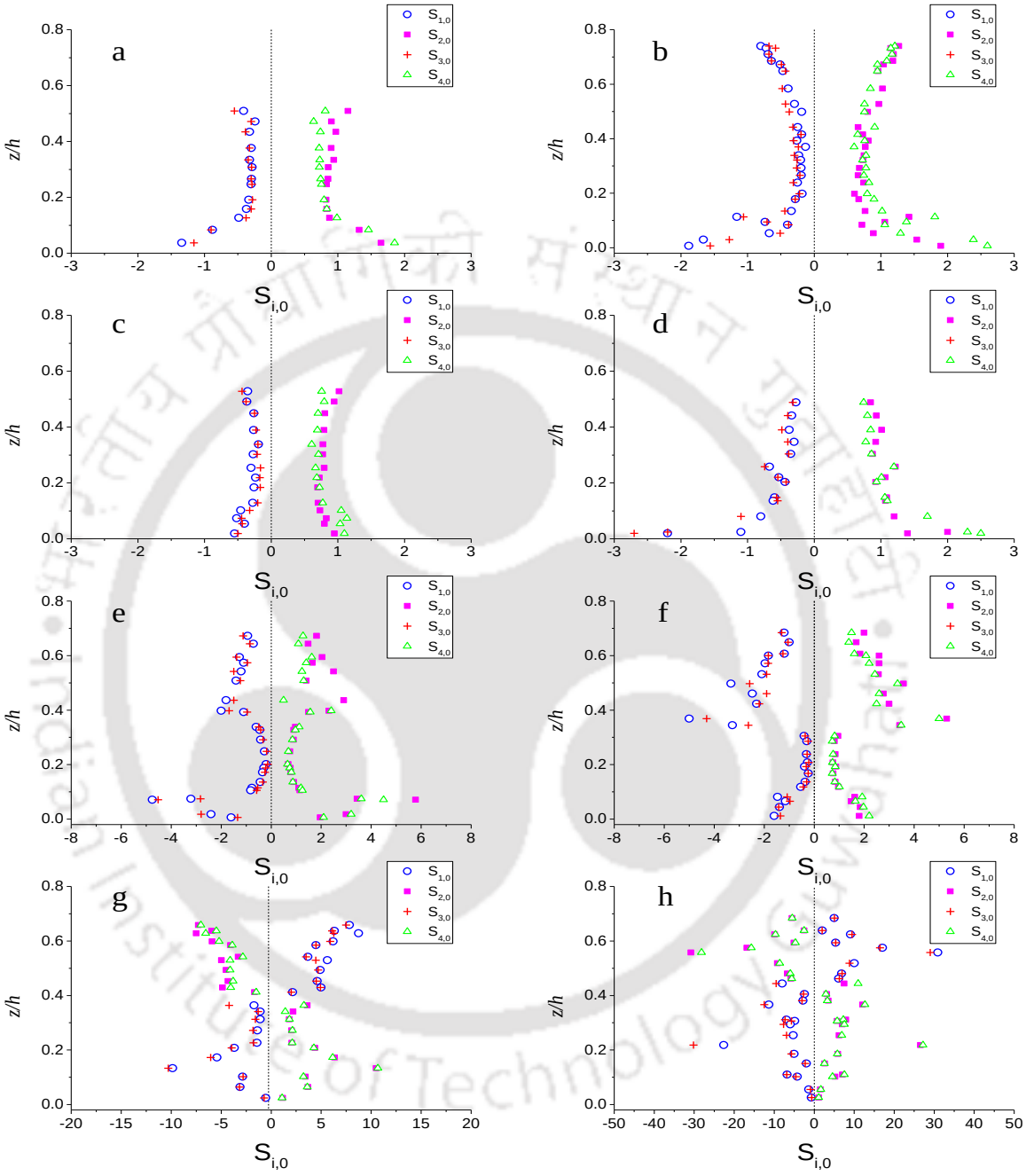

Figure 3.13 Fractional contributions of Reynolds shear stress $S_{i,H}$ at (a) Location 1 (Without pit), (b) Location 1 (with pit), (c) Location 2 (Without pit), (d) Location 2 (with pit), (e) Location 3 (Without pit), (f) Location 3 (with pit), (g) Location 4 (Without pit), and (f) Location 4 (with pit) for hole size H = 0 around the circular pier.

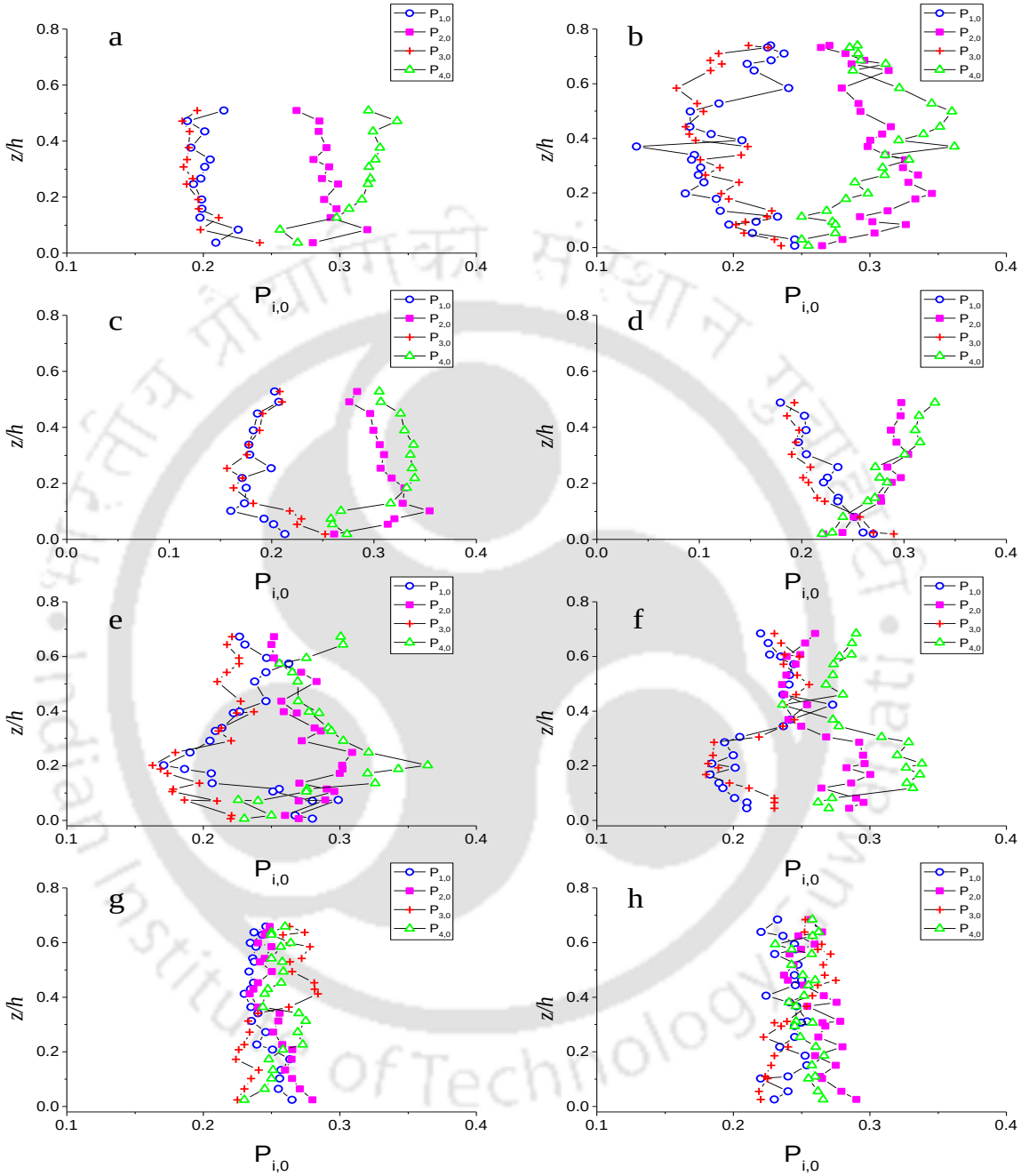

Figure 3.14 Distribution of occurrence probability of bursting events $P_{i,H}$ at (a) Location 1 (Without pit), (b) Location 1 (with pit), (c) Location 2 (Without pit), (d) Location 2 (with pit), (e) Location 3 (Without pit), (f) Location 3 (with pit), (g) Location 4 (Without pit), and (f) Location 4 (with pit) for hole size H = 0 around the circular pier.

When the flow has passed over the pit, i.e., at Location-2 [Figure 3.13(d)], the frequency of ejection and sweep events is decreased by ~ 15% as compared to the without-pit case and the near-bed layer (from bed surface up to z/h ~ 0.15) is dominated by inward and outward interactions. In the upper flow layer (from z/h ~ 0.15 and above), the average frequency of ejection and sweep events is decreased from ~ 70% to 60% in the presence of a mining pit.

In front of the pier, i.e., at Location-3 [Figure 3.13(e) and 3.13(f)], contribution towards the total *RSS* production comes from the ejection and sweep events throughout the measurement depth (down-flow as well as reversal zone) for both cases. At this location [Figures 3.14(e) and 3.14(f)], frequencies of the outward interaction and ejection events are dominant (~ 60%) in the horseshoe vortex zone for without pit case. However, the horseshoe vortex region is dominated by the sweep and ejection events in the case of a pit. The dominance of ejection and sweep is associated with increased sediment motion (Best, 1992). Therefore, the scour hole zone at the pier base has a higher erosive propensity in the presence of an upstream mining pit.

At the rear side of the pier, i.e., at Location-4 [Figure 3.13(g) and 3.13(h)], contributions from the ejection and sweep events are higher in the region from bed surface up to z/h ~ 0.4. However, above this depth, contributions by inward and outward interactions are higher for both cases. In the presence of a mining pit [Figure 3.14(g) and 3.14(h)], the frequency of ejection events has increased by ~ 5%, while the frequency of outward interaction events has decreased by ~ 8% in the flow layer from bed surface up to z/h ~ 0.2.

3.2.9 Scales of turbulence

Taylor micro-scale represents the length scale of the inertial sub-range, which is that part of the universal dissipation range where the viscous effects are negligible, and eddy motions are governed by the inertial effects. It is a representation of a relevant length scale of turbulence and is given by:

$$\lambda_T = \left(15\,\nu\,\overline{u'^2}/\varepsilon\right)^{0.5} \tag{3.17}$$

where ε is the *TKE* dissipation rate. The value of ε can be estimated on the basis of Kolmogorov's second hypothesis (Pope, 2000), by relating the spectral density function S_{uu} in the inertial sub-range with:

$$k_w{}^{5/3} S_{uu} = C\varepsilon^{2/3} \tag{3.18}$$

Where k_w is the wavenumber, C is a constant (0.5, as suggested by Monin & Yaglom, 2013), and S_{uu} is the spectral density function of u'. The turbulent kinetic energy dissipation rate can also be calculated as:

$$\varepsilon = \frac{15\,\nu}{u^2}\overline{\left(\frac{\delta u'}{\delta t}\right)^2} \tag{3.19}$$

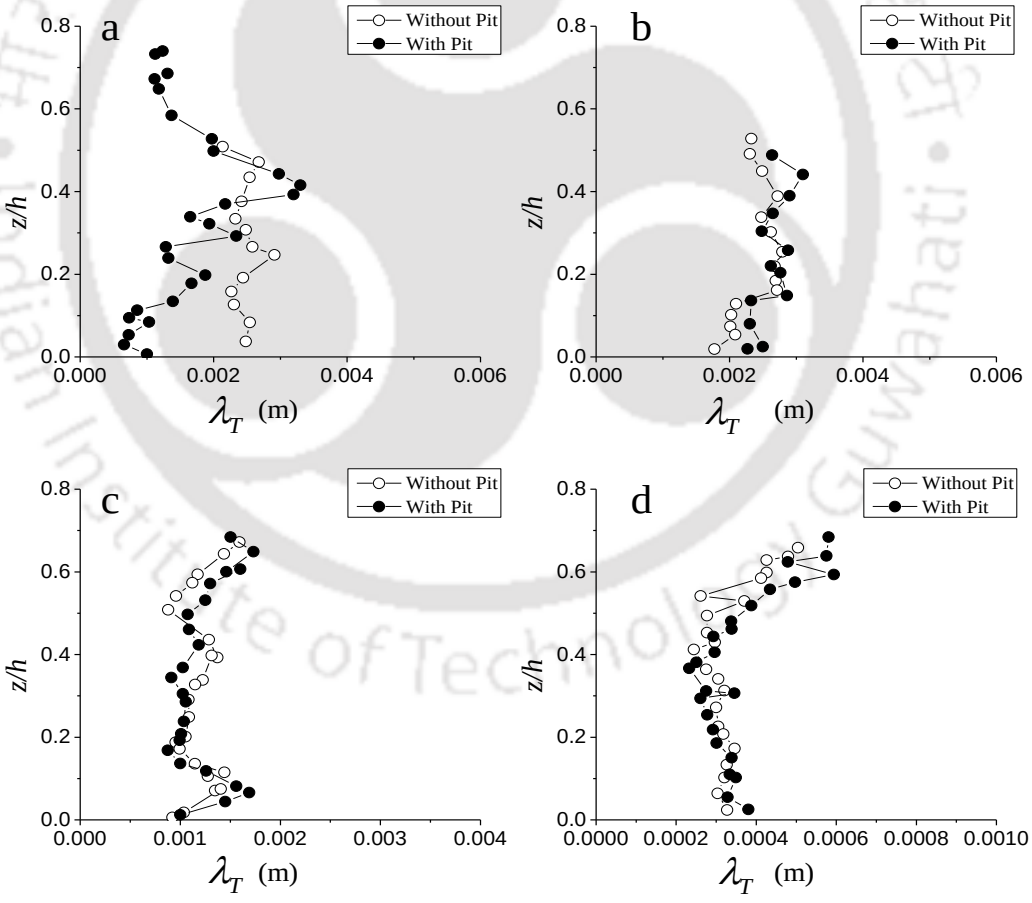

Figure 3.15 Taylor micro-scale λ_T at (a) Location 1, (b) Location 2, (c) Location 3, and (d) Location 4 around the circular pier.

Krogstad and Antonia (1999) found that Equation 3.18 overestimates the value of the dissipation rate, especially in the boundary layer; hence, Equation 3.19 has been used in the present study. Taylor micro-scale λ_T at Locations 1, 2, 3, and 4 are presented in Figure 3.15 for both cases.

Figure 3.15(a) shows that in the pit region (Location-1), the average scale of the inertial sub-range is 30% smaller than that of the no-pit case from bed surface up to $z/h \sim 0.5$. At Location-2 [Figure 3.15(b)], pit excavation causes ~ 15% enlargement of eddy size in the inertial sub-range in the near-bed region ($z/h \sim 0.1$). At the pier front (Location-3), Taylor micro-scales for both cases are similar except for a slight increase in the magnitude in the down-flow region (above $z/h \sim 0.4$). Slight growth in the Taylor micro-scales is also detected in the flow separation zone (above $z/h \sim 0.42$) behind the pier, in the presence of a pit.

Integral length and time scales represent the largest eddies i.e., the energy-containing range of turbulence. Eulerian time scale for a finite time series of velocity can be given by:

$$E_T = \int_0^T R(t)dt \tag{3.20}$$

Here, $R(t)$ is the autocorrelation function for, say u; dt denotes the lag, and T is the time at which the autocorrelation function approaches zero (assuming velocity time series to be purely random). The integral time scale has been calculated from the autocorrelation function for the streamwise velocity data using a lag of 0.01 seconds. Eulerian length scale has also been calculated by using a relation: $E_L = E_T \bar{u}$ (Taylor, 1935). The integral length and time scales at approximately 10 mm above the bed level at Locations 1, 2, 3, and 4 are presented in Table 3.3.

The eddy turnover time in the pit region (near-bed) is 30% more than the without-pit case, yet the length scale of the largest eddies is nearly similar to the without-pit case. Flow passing over the mining pit results in an 18% increase in the energy-containing

largest eddy sizes near the bed at Location-2. At the pier front inside the scour hole (Location-3), the eddy turnover time is decreased due to the presence of a mining pit, but the largest eddy sizes are about 27% bigger than the without-pit case. Eulerian length scale also grows in the scour hole region behind the pier in the case of the mining pit. These results indicate that the dredging of a mining pit leads to greater production of turbulence at pier upstream as well as at the front and rear side of the pier inside a scour hole.

As vortex shedding occurs behind the pier, lateral Euler length scales at Location-4 are also presented in Table 3.4. It can be observed that the effect of mining is maximum in the flow separation zone, as the Euler length scale in the lateral direction increases by about 23%. However, below this zone, the mining pit does not significantly affect the Euler length scales in the lateral direction.

Table 3.3 Eulerian time and length scales at 10 mm above the bed level at various locations around the circular pier

Location	**Eulerian time scale (s)**		**Eulerian length scale (m)**	
	No Pit	**With Pit**	**No Pit**	**With Pit**
Location-1	0.090	0.598	0.0225	0.0239
Location-2	0.214	0.253	0.0400	0.0475
Location-3	0.148	0.070	0.0022	0.0028
Location-4	0.252	0.272	0.0350	0.0390

Table 3.4 Lateral Eulerian length scale at Location-4 around the circular pier

z/h	**Eulerian length scale (m)**	
	No Pit	**With Pit**
0.1 (inside scour hole)	0.009	0.011
0.3	0.056	0.058
0.6 (flow separation zone)	0.026	0.032

3.2.10 Strouhal number

On account of the high Reynolds number, the flow interacting with a circular pier leads to the separation of the boundary layer, and shedding of vortices occurs at downstream of the pier. This is established by the presence of negative velocities in the surface layer of flow (from z/h ~ 0.4 and above) for both cases (i.e., without pit and with pit). These oscillations in the flow are characterized by Strouhal number (St), given as:

$$S_t = \frac{\omega L_{ch}}{\bar{u}} \tag{3.21}$$

Where ω is the frequency of vortex shedding, L_{ch} is the characteristic dimension, which in this case the diameter of the pier, and $\bar{u}$ is the mean flow velocity. The shedding frequency is obtained from the power spectra of streamwise velocity at the pier downstream (Figure 3.16). The frequency associated with the peak is the dominant frequency or shedding frequency. The Strouhal numbers calculated for both cases are given in Table 3.5.

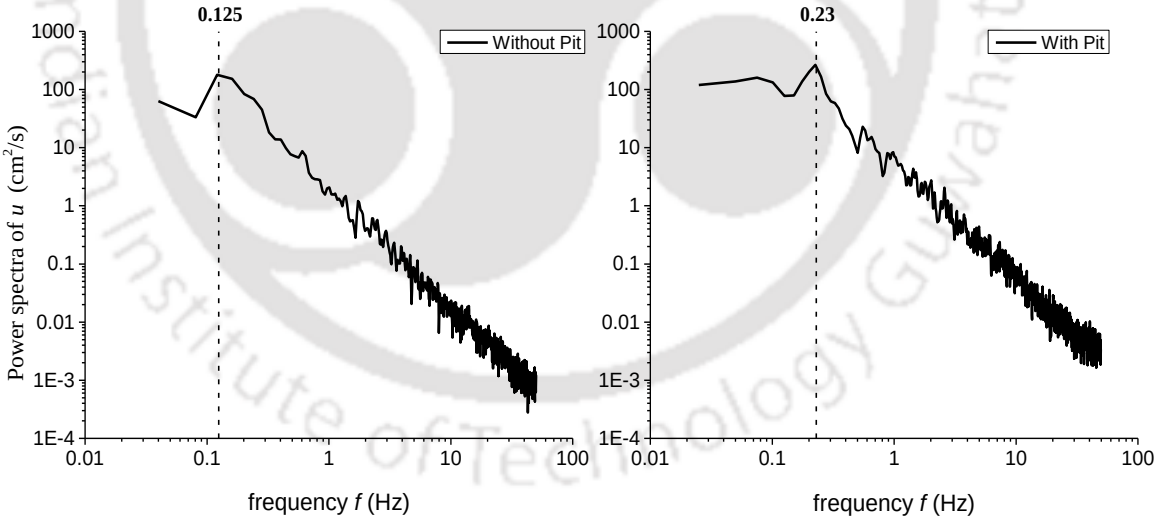

Figure 3.16 Power spectra of streamwise velocity at the rear side of the circular pier (Location-4) at z/h ~ 0.68.

The frequency of vortex shedding in the presence of a mining pit is remarkably higher (f = 0.23 Hz) than without pit case (f = 0.125 Hz). In addition, the peak of spectra at

dominant frequency exhibits a substantial increment (~48%) in the case of a mining pit. The Strouhal number prevailing behind the pier in the without pit case is in conformance to the previous literature (Clark, 2018; Ducrocq et al., 2017). The Strouhal number escalates to 0.38 when the flow that has passed over a mining pit interacts with the pier. This escalation indicates the dominance of inertial forces, and hence oscillations in the flow behind the pier increase because of the pit excavation upstream of the pier.

Table 3.5 Strouhal number behind the circular pier (Location-4)

Case	Dominant frequency (f) (Hz)	Peak of spectra (m^2/s)	Strouhal number S_t
No Pit	0.125	0.0179	0.20
With Pit	0.230	0.0265	0.38

3.2.11 High-order moments of streamwise velocity fluctuations in the cylinder proximity

The turbulence generated due to the fluid-solid interactions around a cylinder becomes significant as it primarily affects the local scouring and deposition characteristics around the cylinder. In order to analyze the effect of channel dredging on the fluid-solid interaction, we also studied the alterations in the scaling characteristics of high order velocity moments around a circular cylinder in a dredged channel.

Recent formulations on the scaling characteristics of high-order velocity moments in pipe flows and turbulent boundary layers form the background of this study. Measurements within the turbulent boundary layer in open-channel flows revealed a peak of the second-order velocity moments close to the channel bed and also detected the effect of wall roughness in the outer layer (Abe et al., 2004; Tachie et al., 2000; Tachie et al., 2004). Hultmark et al. (2012) conducted experiments on high Reynolds number pipe flow and observed dependency of logarithmic scaling zone on Reynolds number, which was supposed to be independent of Reynolds number by earlier studies. For turbulent boundary layers, Meneveau & Marusic (2013) demonstrated that the higher even order

velocity moments also follow a logarithmic behavior, and the scaling depends upon the near-wall length scale as well as outer length scale. De Silva et al. (2015) tested the statistical properties of velocity moments in near-wall and logarithmic region. They validated logarithmic scaling of second-order structure function within the inertial subrange, at sufficiently high Reynolds number. Sharma & Kumar (2018) noticed remarkable similarities in the scaling behavior of high-order velocity moments within a turbulent boundary layer in an open channel with the pipe flows. Comprehensive manifestations of the higher-order velocity moments in this zone of turbulence under the influence of channel dredging are not reported in the literature. The following provides valuable insights on the impact of channel dredging on the nature of turbulence generated around the cylinder.

The higher-order moments were evaluated at Locations 3 and 4 around the cylinder proximity. The mean flow structure due to the fluid-solid interaction is shown in Figure 3.17.

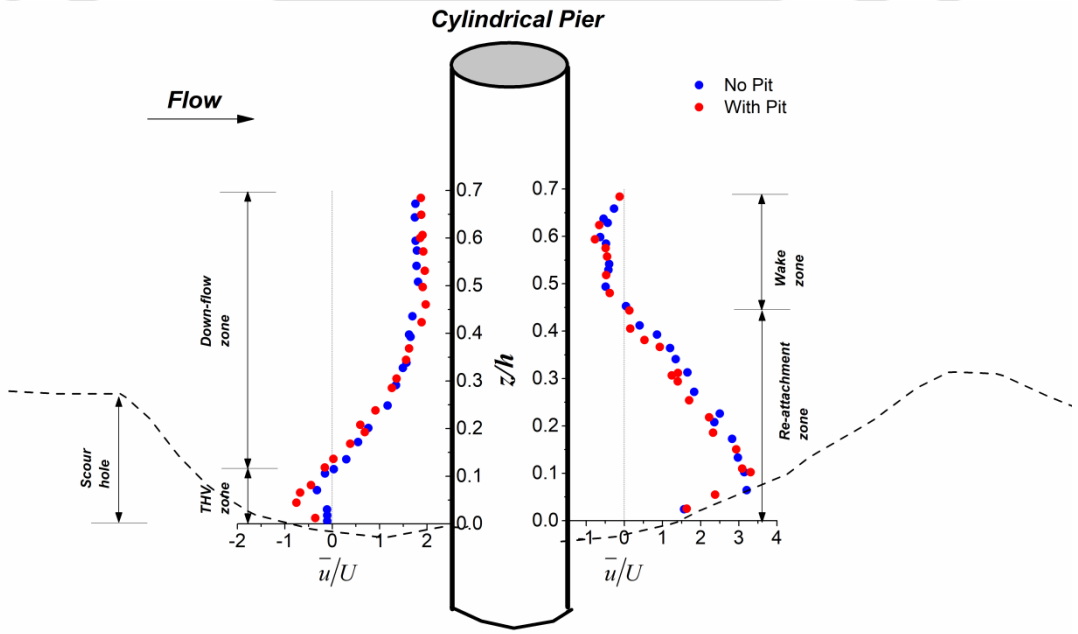

Figure 3.17 Mean flow structure around a circular pier generated due to the fluid-solid interaction.

Recent studies on the turbulent boundary layers (Hultmark et al., 2012; Meneveau & Marusic, 2013) reported a universal form of logarithmic scaling for the variance of streamwise velocity fluctuations $(u'^{+})^2$ as

$$\langle (u'^{+})^2 \rangle = B_1 - A_1 ln\left(\frac{z}{\delta}\right) \tag{3.22}$$

Where $u'^{+} = (u - \langle u \rangle)/u_*$ is the streamwise velocity fluctuation normalized with shear velocity (u_*) given by $u_* = \sqrt{\tau_0/\rho}$ and δ is the boundary layer thickness. The variance of streamwise velocity fluctuations $\langle (u'^{+})^2 \rangle$, are plotted along with normalized depth $z^+ = zu_*/\nu$ in Figure 3.18. Depth is normalized with the characteristic length scale for the near-bed region, i.e. ν/u_*, where ν is the kinematic viscosity of water. It describes the intensity of the turbulence field generated around the cylinder due to the fluid-solid interaction in the mobile bed channel. In front of the cylinder as shown in [Figure 3.18(a)], from the channel bed, the magnitude of $\langle (u'^{+})^2 \rangle$ goes on increasing with z^+ till it reaches its peak (z^+ ~ 400 for no pit case and z^+ ~ 700 in case of a dredged pit). Beyond these distances, logarithmic scaling of turbulence intensity is observed for both cases. A_1 & B_1 are found to be -36.1 & 119.2 for no pit case and -37.7 & 129.6 in case of a dredged pit. It is interesting to note that the peak of turbulence production occurs at a distance where the flow transitions from the THV zone to the down-flow zone for both cases. Logarithmic scaling of $\langle (u'^{+})^2 \rangle$ in the down-flow suggests that turbulence production and dissipation are in equilibrium within this zone.

Close examination of Figure 3.18 also reveals that the peak value of $\langle (u'^{+})^2 \rangle$ decreases at the pier front, but values near the channel bed are higher due to the channel dredging at the rear side. From a granular mechanics standpoint, the drag force acting on the sediment particles is directly proportional to the square of steamwise velocity fluctuations ($F_d \sim u'^2$). Erosion occurs when this drag force on the sediment particles is greater than the critical tractive force. Channel dredging increases $\langle (u'^{+})^2 \rangle$ near the streambed inside the scour hole, thus increasing the instantaneous drag forces on the sediment particles. Primarily, the strength of the THV is responsible for the erosion of sediments around the cylinder. However, higher values of $\langle (u'^{+})^2 \rangle$ near the bed in a dredged channel can lead to an additional amount of erosion around the cylinder due to enhanced drag forces. Such

cases of excessive erosion and undermining of bridge piers caused to sediment mining in natural channels have been reported previously (C Avila, 2016; Sousa et al., 2013).

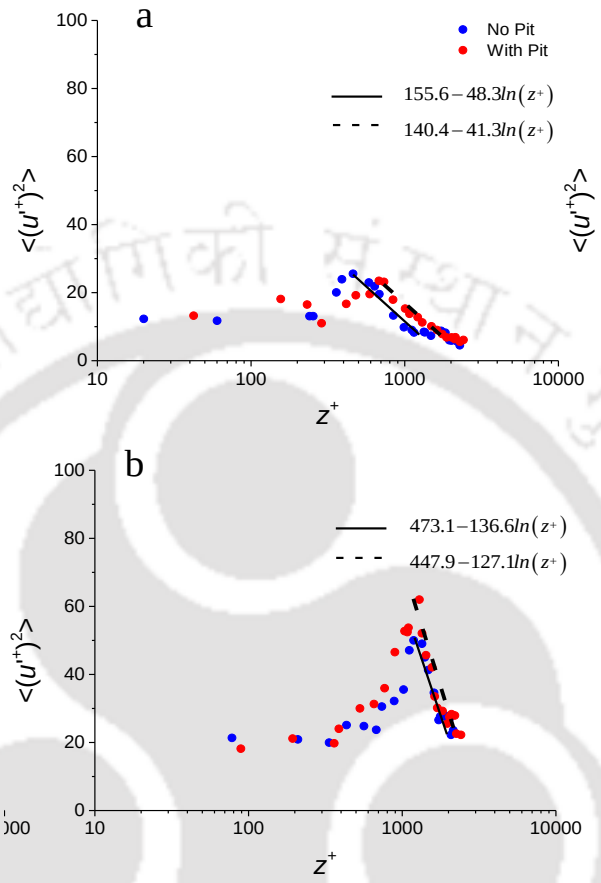

Figure 3.18 Variation of turbulence fluctuations $\langle(u'^{+})^2\rangle$ along with the flow depth z^+ at (a) upstream and (b) downstream of the circular cylinder.

At the rear side of the cylinder in [Figure 3.18(*b*)], $\langle(u'^{+})^2\rangle$ increases with z^+ and the peak is observed at z^+ ~ 1200 for both cases. Thus, peak turbulence production occurs at the interface of the wake zone and flow redevelopment. Above this depth, logarithmic scaling is noticed. Here, A_1 & B_1 are found to be -136.6 & 473.1 for no pit case and -127.1 & 447.9 in case of a dredged pit. It can be seen from Figure 3.18 that the peak of $\langle(u'^{+})^2\rangle$ at the rear side of the cylinder is almost twice the peak at the front side. Also, turbulence production at downstream of the cylinder occurs for greater flow depth (till z^+ ~ 1200) compared to the upstream side (z^+ ~ 400 – 700). Therefore, the flow region in the downstream side of the cylinder is more turbulent than the upstream. Also, about a

15 % rise in the peak of $\langle(u'^{+})^2\rangle$ in this region in the presence of a dredged pit indicates higher turbulence intensity at the rear side of the cylinder on account of channel dredging.

For high Reynolds number pipe flows, Hultmark et al. (Hultmark et al., 2012) observed logarithmic scaling beyond z^+ ~ 400 - 800, depending upon the Reynolds number. They observed that location of peak turbulence shifts further away from the wall with increasing Reynolds number. Similar results were observed by Mckeon et al. (2004), wherein the peak was observed at z^+ ~ 600. Such conclusive studies for turbulent boundary layers in open channel flows are limited. However, experimental results of this study strongly imply that turbulence around the cylinder in an open channel also follows logarithmic scaling of $\langle(u'^{+})^2\rangle$. But the location of peak turbulence and the equilibrium zone of logarithmic scaling depend upon the mean flow structure generated by the fluid-solid interaction. Furthermore, the values of scaling parameters observed around the cylinder in this study differ from the previous results on pipe flows.

Meneveau & Marusic (2013) studied higher-order moments of velocity fluctuations and observed a generalized logarithmic form for p^{th} root of velocity moments as

$$\langle(u'^{+})^{2p}\rangle^{\frac{1}{p}} = B_p - A_p ln\left(\frac{z}{\delta}\right) \tag{3.23}$$

They showed that the 2p order moments of velocity fluctuations, raised to power 1/p, also follow logarithmic law (Equation 3.23) in the same flow region where the scaling of variance is logarithmic. Before evaluating the higher-order moments, the convergence of velocity fluctuations was verified. The pre-multiplied probability density functions $(u'^{+})^{2p}P(u'^{+})$ of the velocity fluctuations at high turbulence zone in the upstream $(z^+ = 400)$ and downstream $(z^+ = 400)$ are plotted in Figure 3.19. The distributions show reasonable convergence; therefore, the high-order moments are discussed further. Figure 3.20 displays the higher-order moments of velocity fluctuations around the cylinder for even order moments 2p = 2, 4, and 6. All the higher-order moments show logarithmic scaling in the down-flow zone at the upstream and in the wake zone at the downstream. Thus, the scaling nature of higher-order moments is found similar to the behavior of variance in agreement to Meneveau & Marusic (2013).

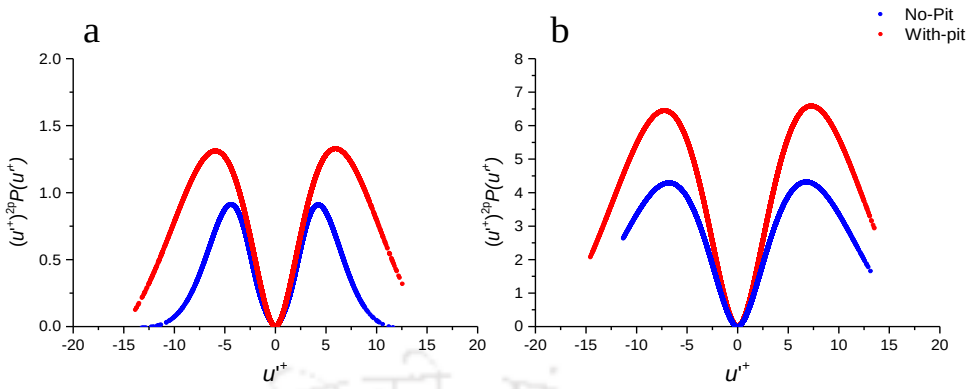

Figure 3.19 Pre-multiplied PDF of velocity fluctuations evaluated at (a) cylinder upstream at $z^+ \sim 400$ and (b) cylinder downstream at $z^+ \sim 1200$ for both cases.

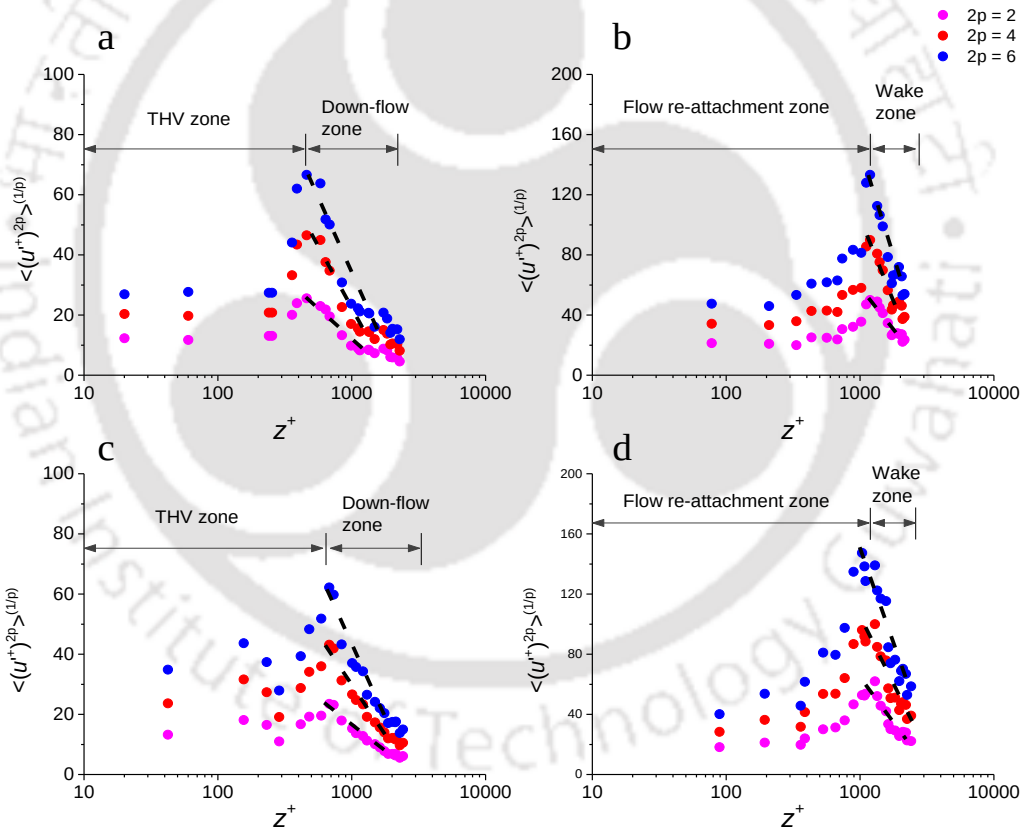

Figure 3.20 High-order moments of velocity $\langle(u'^{+})^{2p}\rangle^{\frac{1}{p}}$ for 2p = 2, 4, and 6 at upstream side for (a) No-pit case and (c) With-pit case as well as at the downstream side for (b) No-pit case and (d) With-pit case. Dashed lines demarcate the log-scaling zones within the flow.

3.2.11 Effect of pit shapes on turbulent flow characteristics

To study the effect of the other two pit shapes (rectangular and irregular) on the flow characteristics around a circular pier, mean velocity profiles and Reynolds shear stress profiles are presented at Locations 1, 2, 3, and 4 for the same discharge. Figure 3.21 and 3.22 compares the mean velocities and Reynolds shear stress profiles at all 4 locations for all three pit shapes (rectangular, trapezoidal, and irregular).

At the pit center (Location -1), The flow separation in the pit zone is similar for the rectangular and trapezoidal pit. However, for the irregular pit, the flow separation and negative velocities at the bottom are weak as compared to other pit shapes since the length of the irregular pit is greater. Here, the peak turbulent stresses are greater for irregular and rectangular pit compared to the trapezoidal pit.

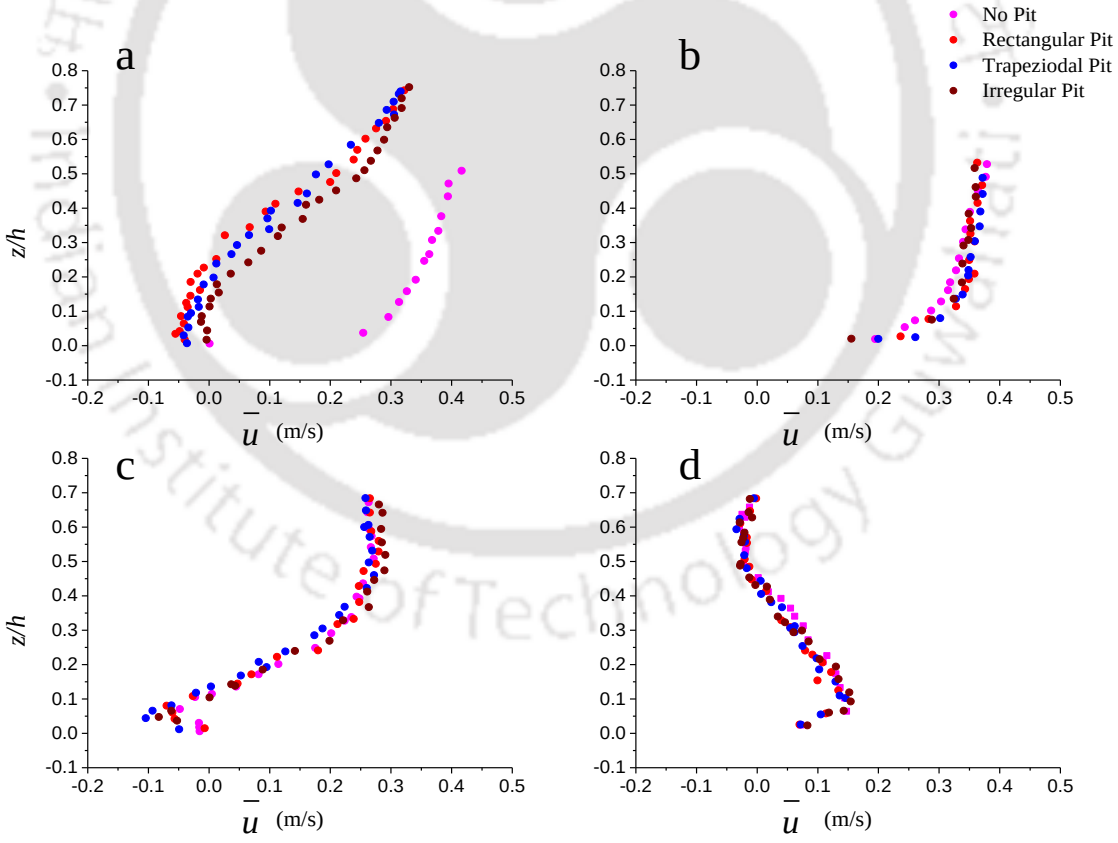

Figure 3.21 Mean streamwise velocity profiles for all three pit shapes at (a) Location -1 (b) Location 2, (c) Location -3, and (d) Location -4.

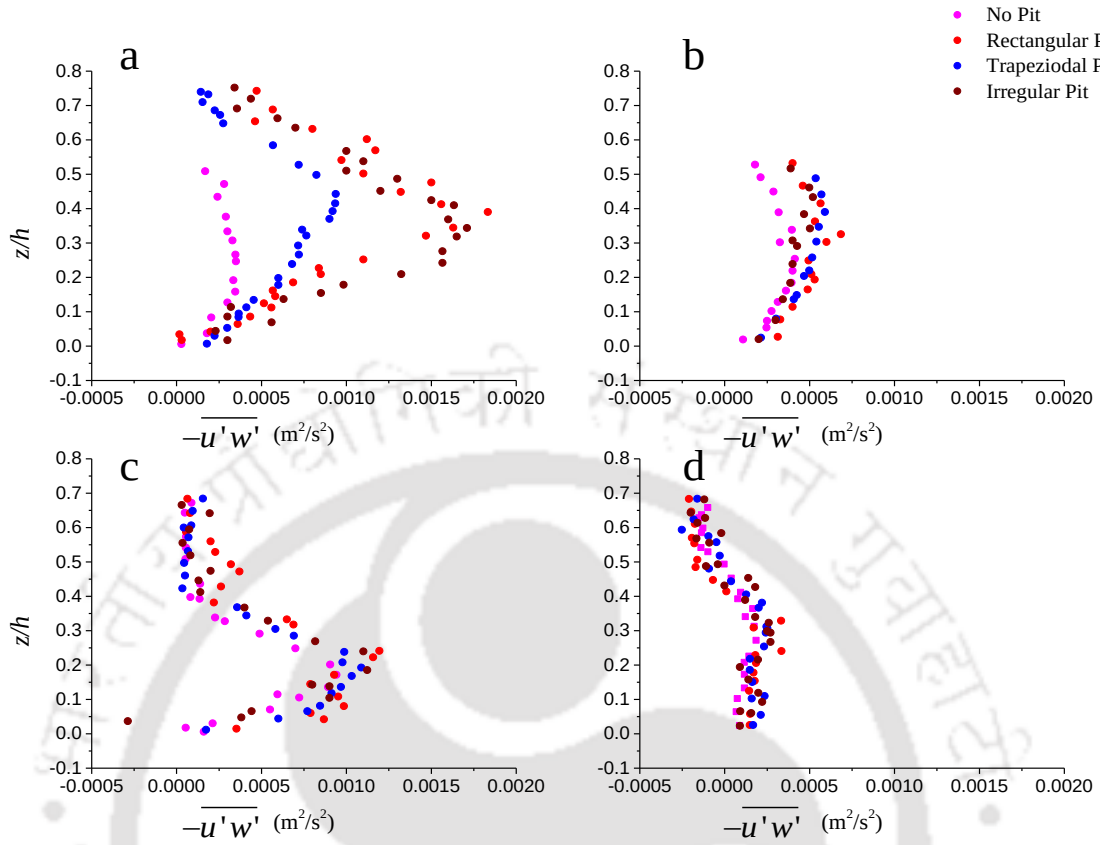

Figure 3.22 Reynolds shear stress (RSS) profiles for all three pit shapes at (a) Location -1 (b) Location 2, (c) Location -3, and (d) Location -4.

At the approach zone (Location -2), the mean velocity profiles, as well as the RSS profiles for all three pit shapes, is almost similar. The rise in the near-bed velocities and increase in the turbulent stress in the upper flow region ($z/h > 0.2$) is similar for all three pit shapes. The mean velocities in front of the pier (Location -3) is also similar for all three pits, however, the velocities in the down-flow zone is are slightly higher in case of an irregular pit. Also, the RSS in the down-flow zone, as well as peak RSS at the initiation of flow recirculation are slightly higher in the case of the rectangular pit, compared to other shapes. At the rear side of the pier, the mean velocities and RSS profiles are almost similar for all cases. The effect of pit shapes on the scour and morphological characteristics are discussed in detail in Chapter 4 based on the morphological findings of all the test cases.

3.2.12 Summary

Summary of the findings based on some turbulent flow parameters observed around a circular bridge pier with and without the presence of an upstream mining pit is as follows:

When flow passes over a mining pit, flow separation occurs on account of a sudden positive pressure gradient, and reattachment of the flow takes place at the downstream edge. A flow reversal zone has been detected inside the pit region. Subsequently, the flow approaches the pier with higher spatial acceleration as compared to without pit case. The streambed upstream of the pier is subjected to higher near-bed mean streamwise velocities in the presence of a pit. Pit excavation can be viewed as a source of turbulence to the downstream flow. The turbulent stresses in the pit region and its downstream increase significantly. An increase in the average turbulent stresses indicates that the excavation of a pit leads to excess momentum transport along with the flow depth inside the pit as well as in its downstream zone. The streambed in the downstream region of the pit is subjected to a higher bed shear stress.

When such flow passing over a pit interacts with a circular pier in the downstream, alterations occur in the flow field around the pier. A stronger horseshoe vortex is formed with greater eddy sizes at the base of the pier front, which can aggravate local scour. The turbulent stresses in this horseshoe vortex zone also increase, and the dominance of sweep and ejection events in this zone is greater than without pit case. Thus, the scour hole at the pier front has a higher sediment transport propensity. Analysis of the turbulent kinetic energy flux in the scour hole zone shows that the pit excavation causes a greater flux of the streamwise turbulent kinetic energy to travel in the streamwise direction. Further, a stronger flux of the vertical turbulent kinetic energy rushes in a vertically downward direction inside the scour hole.

At the rear side of the pier, lateral turbulent shear stresses are found to be significant due to the vortex shedding in downstream. After passing over a pit, these lateral turbulent shear stresses behind the pier are found to increase remarkably. The interaction of the

flow with the pier after passing over a pit significantly increases the length scale of the largest eddies, which are being shed in the flow reversal zone behind the pier. Estimation of the Strouhal number indicates that the strength and frequency of the shedding vortices behind the pier rise due to the pit excavation upstream of the pier, which may alter the transport characteristics at the pier downstream.

The mean flow zones formed around the cylinder govern the scaling characteristics of higher-order moments of streamwise velocity fluctuations around the cylinder. At the cylinder front, turbulence production increases from the channel bed and reaches its peak at a distance where the flow transitions from the recirculation zone (negative mean streamwise velocities) to the down-flow zone (positive mean velocities). Beyond this distance, the variance of streamwise velocity fluctuations follows log law. At the rear side, turbulence production occupies greater flow depth from the channel bed (till z/h ~ 0.4) compared to the front side (till z/h ~ 0.11), and the peak reaches where the boundary layer separates from the cylinder and wake zone occurs. Beyond this distance, log scaling of variance is observed within the wake zone. Scaling of higher-order moments, namely 2p = 4 and 2p = 6, is similar to the variance. These findings validate the universality of logarithmic scaling even in the turbulence field generated around the cylinder due to fluid-solid interaction. Channel dredging increases the peak of $\langle((u'^{+})^2\rangle$ about 5% at the cylinder front and about 15% at the rear side.

3.3 Effect of a Mining Pit on Turbulent Flow Characteristics around an Oblong Pier

3.3.1 Experimental cases and data recording

For this study, experiments were conducted for two cases (Figure 3.23). For the first case, a pier model with an oblong shape (75 mm width and 150 mm length) was embedded in the sand bed at 11.0 m from the upstream entry. Pier diameter was kept less than 0.1 times the channel width, as suggested by (Chiew & Melville, 1987), to avoid boundary effects. Flow was passed gradually till steady flow conditions were reached at a flow discharge of 0.0441 m³/s. The discharge value was adopted to obtain a high Reynolds

number (*Re*), as the local scour becomes independent of the Reynolds number for *Re* >10^4 (Muzzammil & Gangadhariah, 2003). The slope of the channel bed was 0.0017, and the Froude number (*Fr*) of the flow was 0.41. For the second case, a pit was carefully dredged 0.5 m in front of the pier. The shape of the pit was rectangular, having 0.5 m length (along the flow direction) and 0.1 m depth. Similar hydraulic conditions were maintained for both experiments (Table 3.6). The scour depth was monitored using Seatek® ultrasonic ranging system. For both cases, turbulent velocity measurements were done after the local scour depth became constant.

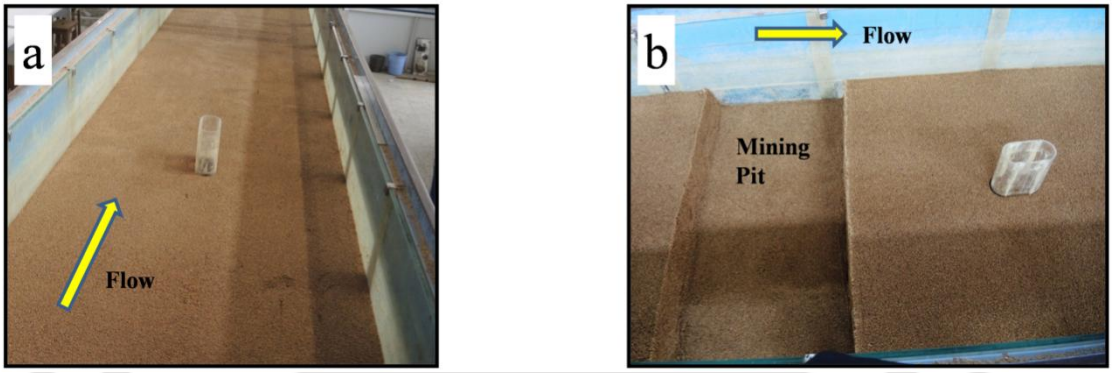

Figure 3.23 Snapshots of the test cases for oblong pier (a) without pit and (b) with pit.

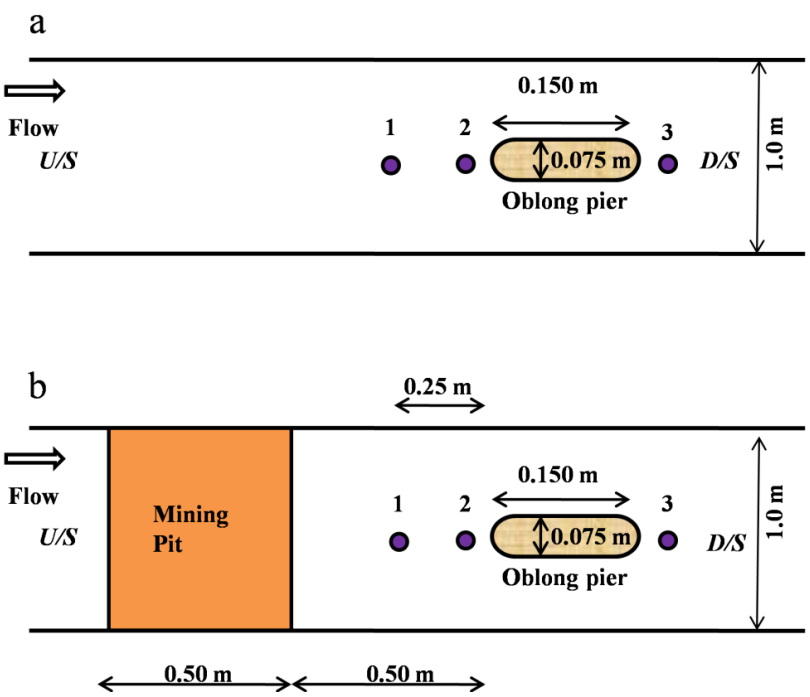

Figure 3.24 Schematic representation of the measurement Locations around the oblong pier

Table 3.6 Hydraulic conditions of the experiments on the oblong pier

Case	Discharge (m^3/s)	Median particle size (mm)	Froude Number *Fr*	Reynolds number *Re*
No Pit	0.0441	1.1	0.493	40951
With Pit	0.0441	1.1	0.493	40951

Turbulent velocity data was recorded along with the depth at three different locations around the pier (Figure 3.24). Measurement Location-1 was at 250 mm upstream of the pier nose. It is the location where the flow is approaching the pier after passing over the mining pit. Locations-2 was 50 mm upstream, and Location-3 was 50 mm downstream from the pier edge, along the centerline of the pier. Locations 2 and 3 were in proximity of the pier inside the scour hole.

3.3.2 Mean Velocities

The time-averaged velocity profiles in the streamwise direction at Locations 1, 2 and 3 along the non-dimensional depth (z/h) are presented in Figure 3.25. Velocity vector plots in the X – Z plane for both the cases are shown in Figure 3.26. The demarcation of mean flow zones in the pier proximity is shown in Figure 3.27.

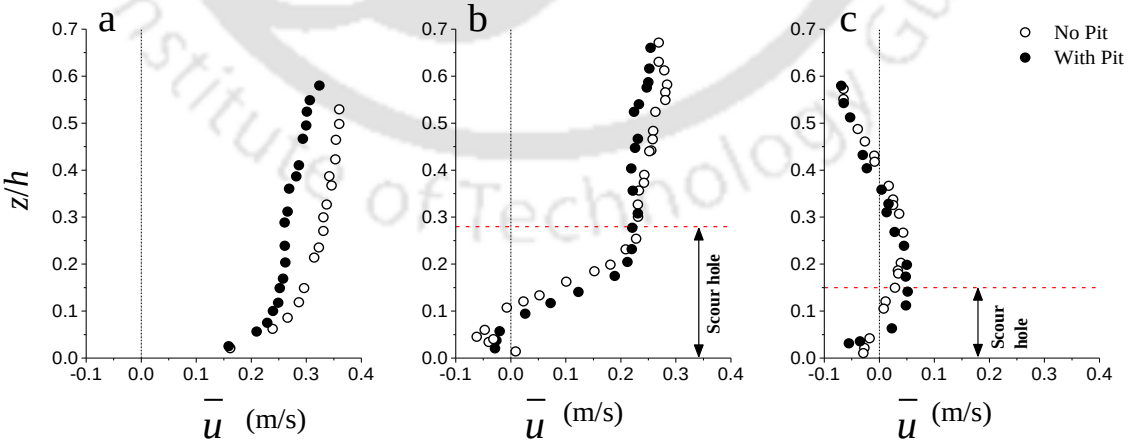

Figure 3.25 Mean streamwise velocity profiles at (a) Lection-1 (b) Location-2 and (c) Location-3 around the oblong pier.

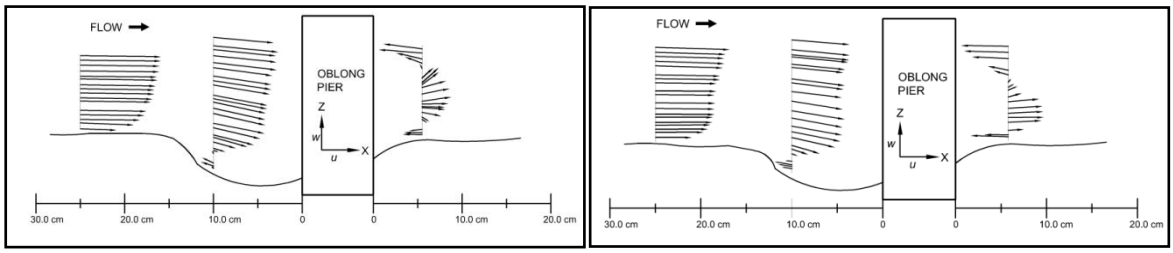

Figure 3.26 Mean velocity vector plot in the X – Z plane for No pit case (Left) and With pit case (Right).

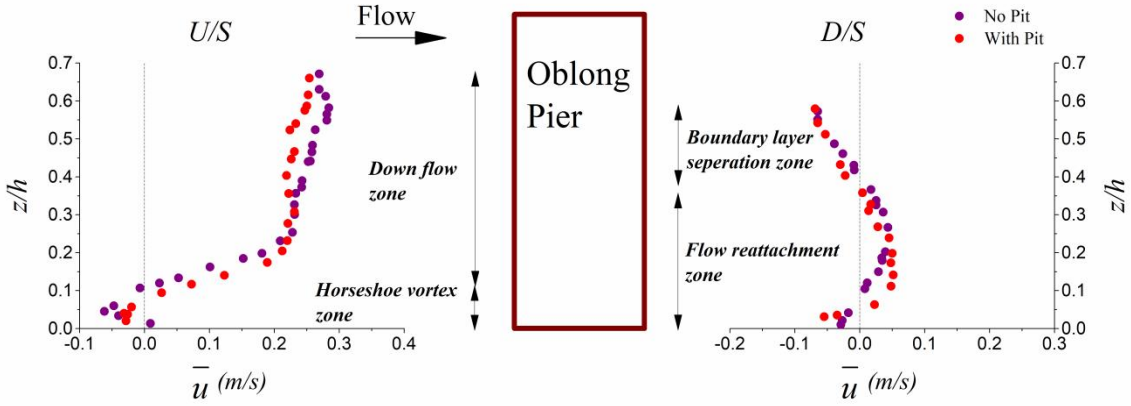

Figure 3.27 Flow zone demarcations along with the depth around an oblong pier.

After crossing the pit [Figure 3.25(a)], the flow approaches the pier with reduced mean velocities (about 15%) and higher depth (z/h ~ 0.6). As the flow interacts with the pier front, it moves downward along the pier due to stagnation. This flow interacts with the mean flow at the base, which is moving the streamwise direction, which results in flow reversal. The reversal zone is observed until z/h ~ 0.1 from the bed (Figure 3.27). This flow zone can be identified as the horseshoe vortex zone. Above z/h ~ 0.1, the down-flow exists as the mean velocities are positive. Boundary layer separation occurs as the water flows past the pier, which is revealed by the negative velocities at the rear side of the pier (above z/h ~ 0.4). The flow zone from the bed until z/h ~ 0.4 is the zone of reattachment of flow (Figure 3.27). After passing over the pit, mean streamwise velocities in the down-flow zone (above z/h ~ 0.3) have decreased by about 10 % as compared to no pit. Also, at the rear side of the pier, the near-bed streamwise velocities are about 15 % greater in the presence of a mining pit.

3.3.3 Bed shear stress and turbulent viscosity of the incoming flow

The local scour, and the characteristics of the sediment movement around the pier are primarily governed by the interaction of the flow and pier. Dredging of a mining pit at the upstream side of the pier can alter the characteristics of the incoming flow, which interacts with the pier.

Shear velocity (u_*) at the upstream bed of the pier (Location-1) was calculated from the RSS measurements as $u_* = \left[\sqrt{-\overline{u'w'}}\right]_{z=0}$ (Figure 3.28). Damping of RSS profiles is observed near the streambed for both cases. Damping occurs due to the motion of sediment particles at the bed, and it is observed previously by many authors (Deshpande & Kumar, 2016; Dey et al., 2012). After passing over a pit, the peak RSS escalates as well as the damping is also stronger. This suggests the excess motion of bed particles due to the incoming flow after passing over a pit. Shear velocity and bed shear stress were found to be 0.0262 m/s and 0.686 N/m^{2,} respectively, for no pit case and 0.0371 m/s and 1.376 N/m^2 in case of a mining pit. Thus, after passing over a dredged zone, the bed shear stress exerted by the flow is significantly higher.

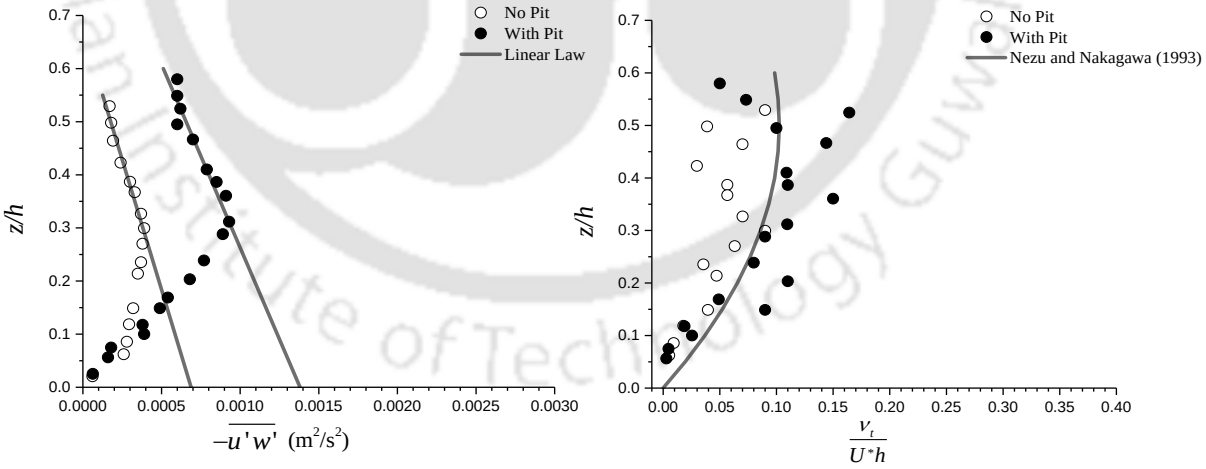

Figure 3.28 Estimation of bed shear stress by linear law at Location-1 (Left) and variation of normalized eddy viscosity along with the flow depth at Location-1 (Right) around the oblong pier.

The turbulent viscosity (ν_T) of the incoming flow (Location-1) is presented in Figure 3.28 (Right). The Experimental data mostly follows the theoretical equation given by Nezu & Nakagawa (1993) within the inner layer (below z/h ~ 0.4). However, in the outer layer (above z/h ~ 0.2), the scatter of the data from the theoretical equation is quite high, especially in the case of a mining pit. The Turbulent viscosity values, especially in the upper region of flow, are significantly higher in the presence of an upstream mining pit. Thus, the pit excavation provides a mechanism for excess momentum transport rate across the flow depth in the downstream flow.

3.3.4 Reynolds shear stresses (RSS)

At the pier upstream, the momentum transport is across a plane parallel to the flow (plane *X*-*Y*) because of the down-flow and unsteady eddy motions in the reversal zone. This leads to the evolution of turbulent shear stresses (Reynolds shear stress) in the streamwise (τ_{Z-X}) and lateral direction (τ_{Z-Y}) as shown in Figure 3.29. The Reynolds shear stress in the streamwise and lateral directions have been computed as $\tau_{Z-X} = -\rho\overline{u'w'}$ and $\tau_{Z-Y} = -\rho\overline{v'w'}$ respectively. The vertical distribution of Reynolds shear stresses (RSS) at upstream and downstream of the pier is shown in Figure 3.30.

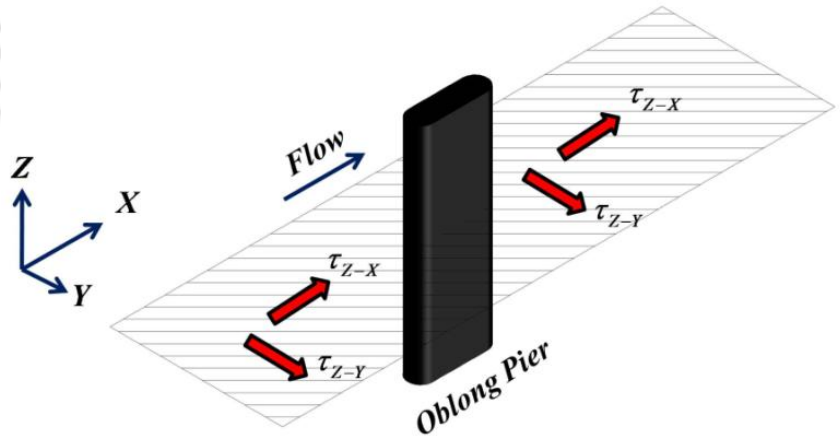

Figure 3.29 Schematic representation of Reynolds shear stresses around an oblong pier.

At the pier upstream, streamwise RSS is negligible in the down-flow zone and concentrated in the bed-proximity zone (till $z/h \sim 0.2$) for no pit case. In the presence of a mining pit, the magnitude of streamwise RSS is twice in the down-flow zone and slightly greater in the bed-proximity region. As the magnitudes of lateral velocities are insignificant, the lateral RSS at the pier upstream are negligible, except for the near-bed zone. Pit excavation slightly increases the lateral RSS at the upstream base of the pier. At the pier downstream, interactions (outward and inward) are the major contributors to the streamwise RSS throughout the flow depth. Streamwise RSS show a rise of about 20 % in the bed-proximity zone (till $z/h \sim 0.2$) in the presence of a pit. On account of higher mean lateral velocities, very high magnitudes of lateral RSS are generated in the presence of a pit at downstream of the pier, especially in the flow reattachment zone.

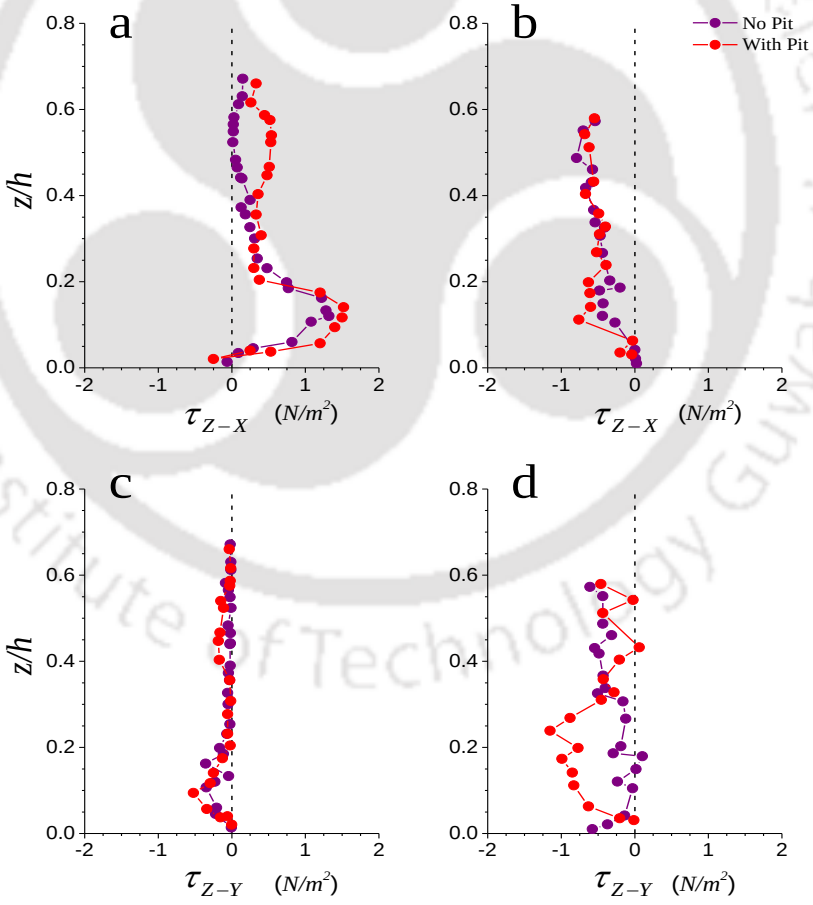

Figure 3.30 Reynolds shear stress τ_{Z-X} at (a) upstream, (b) downstream of the oblong pier; and τ_{Z-Y} at (c) upstream, (d) downstream of the oblong pier.

3.3.5 Quadrant analysis of the Reynolds shear stresses

The momentum transport across the plane parallel to the flow around the pier primarily leads to the turbulent stresses on this plane. The erosion and deposition characteristics around the pier are a result of these stresses. For better apprehension of the effect of a mining pit on the nature of turbulent stresses, quadrant analysis was performed on the streamwise RSS (τ_{Z-X}).

At any point in the flow, the velocity fluctuations u' and w' can be plotted on a $u'w'$ plane with four quadrants (lu & Willmarth, 1973). These four quadrants represent four different types of bursting events, namely: [*Q1*] Outward interactions ($u' > 0,\ w' > 0$); [*Q2*] Ejections ($u' < 0,\ w' > 0$); [*Q3*] Inward interactions ($u' < 0,\ w' < 0$), and [*Q4*] Sweeps ($u' > 0,\ w' < 0$). Further, a hyperbolic hole region (*H*) is introduced on the $u'w'$ plane, given by: $|u'w'| = H(\overline{u'u'})^{0.5}(\overline{w'w'})^{0.5}$. The difference between strong and weak events can be understood using smaller values of *H* while larger values of *H* are used to estimate the contribution of only stronger events among all four types of bursting events to the total RSS production.

The total Reynolds shear stress at a point is the summation of shear stress contribution from all bursting events $\left(\tau_{Z-X} = RSS_{Q1} + RSS_{Q2} + RSS_{Q3} + RSS_{Q4}\right)$.

$$RSS_{Q1} = -\rho\overline{u'w'}_{[+u',+w']};\ RSS_{Q2} = -\rho\overline{u'w'}_{[-u',+w']}$$
$$RSS_{Q3} = -\rho\overline{u'w'}_{[-u';-w']};\ RSS_{Q4} = -\rho\overline{u'w'}_{[+u',-w']} \quad (3.24)$$

The contribution of various bursting events towards the total RSS is presented in Figure 3.31. The probability of occurrence P_i of the bursting events can be calculated as $P_i = n_i/N$, where n_i is the number of bursting events in the quadrant i and N is the total number of events. Occurrence probability plots of the bursting events are presented in Figure 3.32.

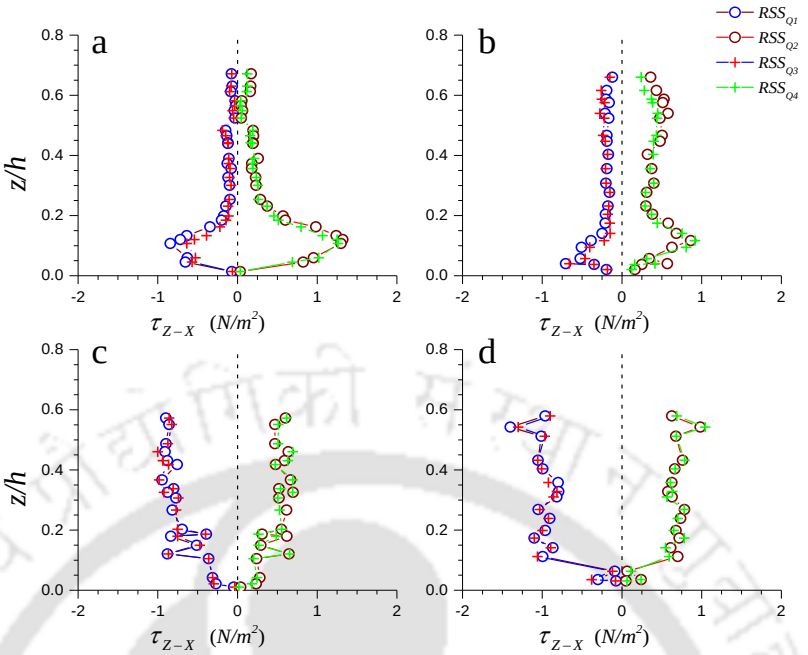

Figure 3.31 Contribution of various bursting events to the total Reynolds shear stresses at (a) upstream (no pit), (b) upstream (with pit), (c) downstream (no pit), and (d) downstream (with pit) considering all the events (Hole size H = 0) around the oblong pier

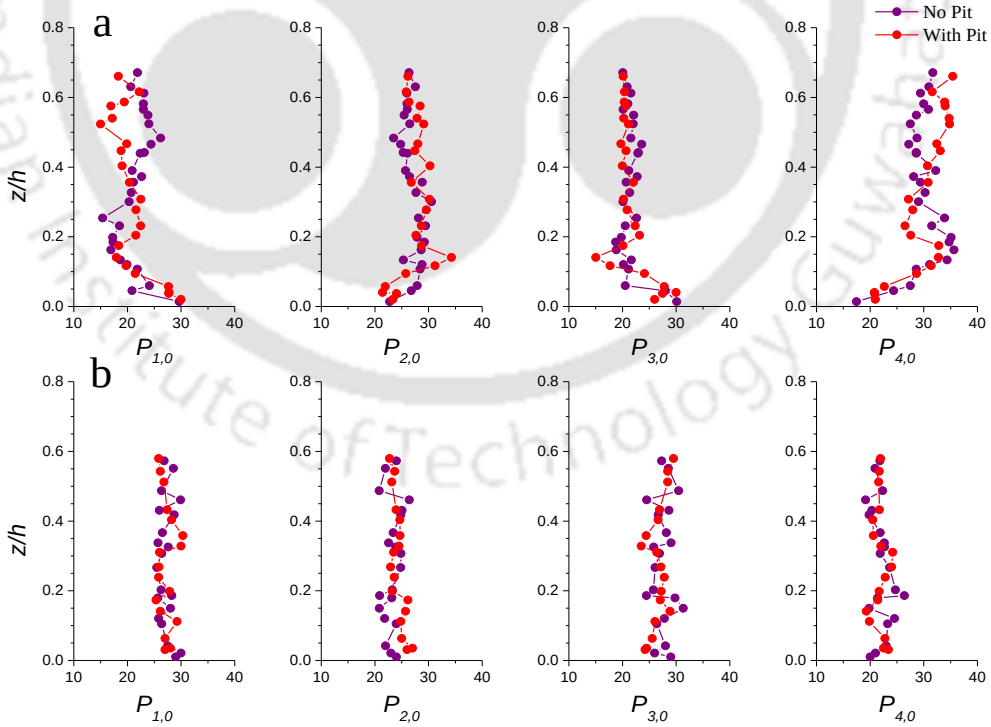

Figure 3.32 Occurrence probability of various bursting events in percentages at (a) upstream, and (b) downstream of oblong pier considering all the events (Hole size H = 0).

After passing over the pit, flow interacts with the pier upstream and moves downward. The Reynolds stresses due to the ejection and sweep events are found to be significantly higher in this down-flow zone [Figure 3.31(a) and 3.31(b)]. In this zone, the occurrence probability of ejection and sweep events has also increased [Figure 3.32(a)]. These findings indicate that after flowing over a pit, the turbulence production is higher in front of the pier as the *Q2* and *Q4* are responsible for turbulence production. At the base of the pier, the RSS due to ejection and sweep have decreased as compared to no pit case.

At the pier downstream, RSS contribution is dominated by inward and outward interactions throughout the flow depth [Figure 3.31(c) and 3.31(d)]. Also, the occurrence of inward and outward interactions is greater than the sweep and ejection events [Figure 3.32(b)]. Pit excavation causes about a 20 % rise in the magnitudes of inward and outward interaction events in the bed-proximity zone up to $z/h \sim 0.2$. But the occurrences of bursts are not significantly altered by the presence of a pit.

Absolute momentum flux carried by various bursting events at varying hole sizes are studied at the front and rear side of the pier to identify the stronger bursting events. Momentum flux at the front side of the pier in the down-flow zone ($z/h = 0.61$) is shown in Figure 3.33, while in the flow reattachment zone ($z/h = 0.14$) at the rear side of the pier is shown in Figure 3.34.

At the upstream of the pier, we can observe that ejection and sweep events are responsible for momentum flux exceeding the average momentum flux value of the hole factor for both cases. In the presence of a pit, even at a higher hole size, momentum flux is transported normally to the *X*-*Y* plane through the ejection events. Thus, pit excavation causes extreme ejection events at the pier front.

At the rear side, pit excavation leads to stronger inward interaction events that are responsible for momentum transport. The excess momentum exchange across a plane parallel to the flow caused due to these extreme events enhances the effective mobility of bed sediments by increasing their temporary suspension and movement (Guan et al., 2018). These characteristics may be linked to the excess scour and transport of sediments around the pier due to dredging activities.

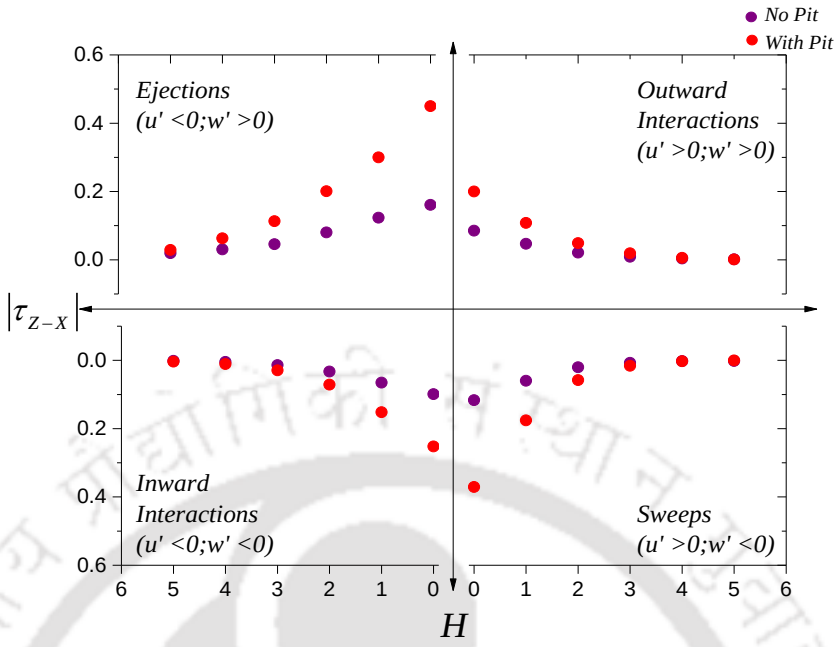

Figure 3.33 Quadrant hole analysis of the Reynolds shear stress τ_{Z-X} in the down-flow zone at the oblong pier upstream (z/h = 0.61). It shows momentum carried normal to the X-Y plane by extreme events of each type of bursts (excess than the average momentum of the hole).

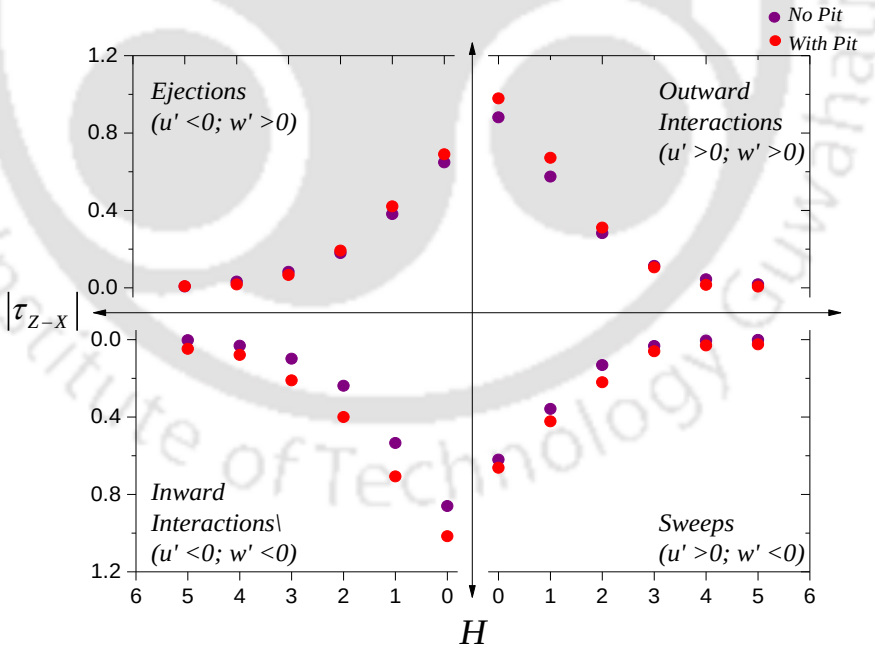

Figure 3.34 Quadrant hole analysis of the Reynolds shear stress τ_{Z-X} in the flow reattachment zone near the bed at the oblong pier downstream (z/h = 0.14). It shows momentum carried normal to the X-Y plane by extreme events of each type of bursts (excess than the average momentum of the hole).

3.3.6 Instantaneous bed shear stress induced by the turbulent horseshoe vortex (THV)

The turbulent horseshoe vortex (THV) formed at the base of the pier exerts high shear stress, which causes erosion within the local scour region. It is formed within the flow reversal zone (below z/h~0.1) detected inside the scour hole in front of the pier (Location-2). However, these stresses vary temporally on account of continuous formation and progression of THV vortices. The instantaneous bed shear stress (τ_b) beneath the THV can be calculated by Equation 3.25 (Graf & Istiarto, 2002).

$$\tau_b = \rho(\nu + \nu_T)\frac{u}{y} \tag{3.25}$$

where ρ is the mass density of water, ν is the kinematic viscosity, ν_T is the turbulent viscosity, u is the instantaneous streamwise velocity, and y is the vertical distance of the measurement point from the streambed, respectively. The instantaneous amplification of the bed shear stress is quantified by (τ_n) which is the ratio of instantaneous bed shear stress (τ_b) to the average bed shear stress (τ_o) exerted by the approaching flow at the pier upstream. These amplifications in the bed shear stress at the base of the pier front on account of THV are presented in Figure 3.35 for both cases. The absolute value of normalized critical bed shear stress τ_c/τ_o is also shown here. Figure 3.31 reveals that there is a drastic variation in the bed shear amplification over the temporal scale. τ_n is characterized by fluctuations at high frequencies and shows strong irregular periodic patterns along the temporal scale at low frequency. The high-frequency fluctuations in τ_n arise due to the instantaneous turbulent bursts occurring inside the near-bed boundary layer. The quasi-periodic nature of τ_n beneath the THV zone can be linked to the process of dynamic formation and progression of turbulent horseshoe vortices.

The RMS values of τ_n for no pit and with pit cases are found to be 2.15 and 3.87, respectively. Thus, in the presence of an upstream mining pit, the instantaneous bed shear stress amplification in the local scour region on account of the THV increases by about 80%. Consequently, excess erosion inside the scour hole might occur due to mining.

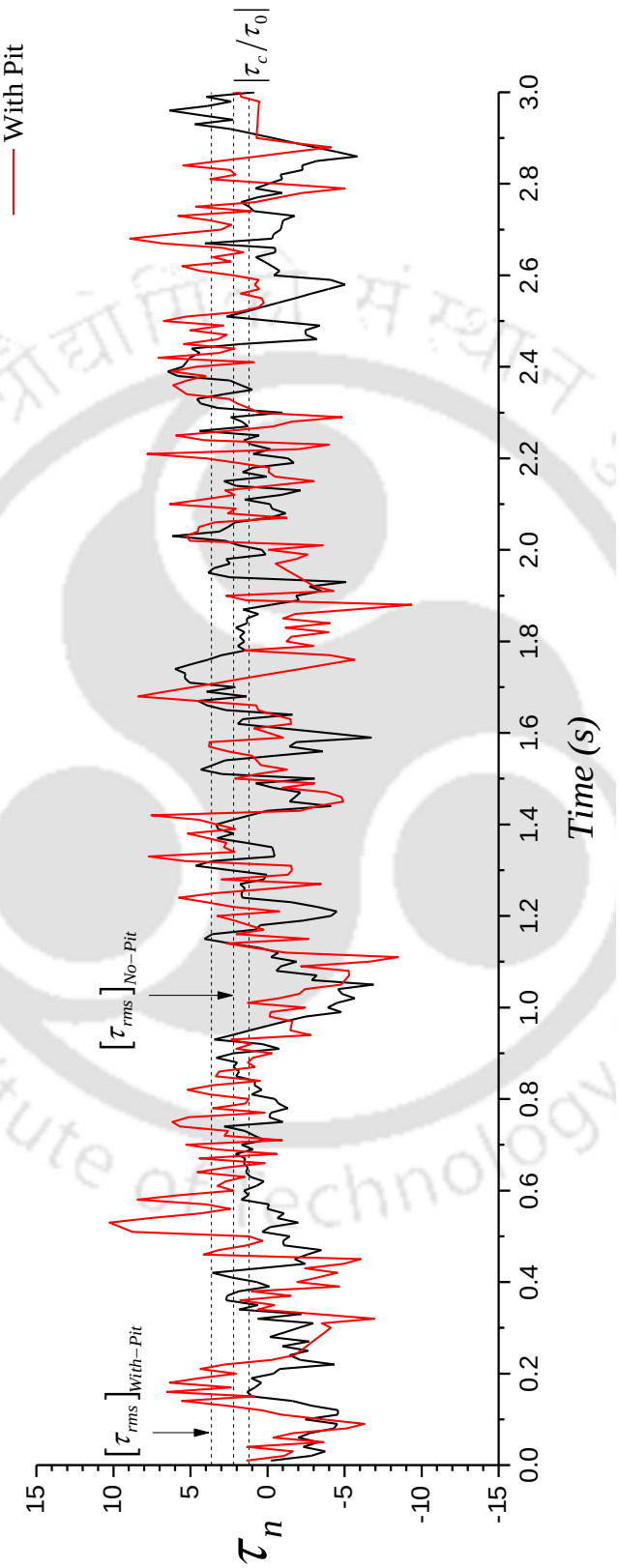

Figure 3.35 Temporal variation of instantaneous bed shear stress amplification (τ_n) within the THV zone of an oblong pier.

3.3.7 Flow oscillations and Strouhal number

Flow past the oblong pier causes separation, which is evident from the negative velocities observed in the upper flow zone. Alternating vortices at the rear side result in vibrational forces on the pier. The oscillatory behavior of flow is characterized by the Strouhal number (S_t) given as: $S_t = \omega\, L_{ch}/\bar{u}$; where ω is the frequency of vortex shedding, L_{ch} is the characteristic dimension of the pier and $\bar{u}$ is the mean flow velocity (Ducrocq et al., 2017). Here, the width of the oblong pier (75 mm) is the characteristic dimension.

Power spectral analysis was performed to detect the frequency of vortex shedding (ω). First, the power spectra of velocities in *X*, *Y*, and *Z* direction were calculated by performing a fast Fourier transform (FFT) of the respective auto-correlation functions. Then a resultant power spectra *F*(*f*) (summation of all three power spectra) was plotted against the frequency, as shown in Figure 3.36.

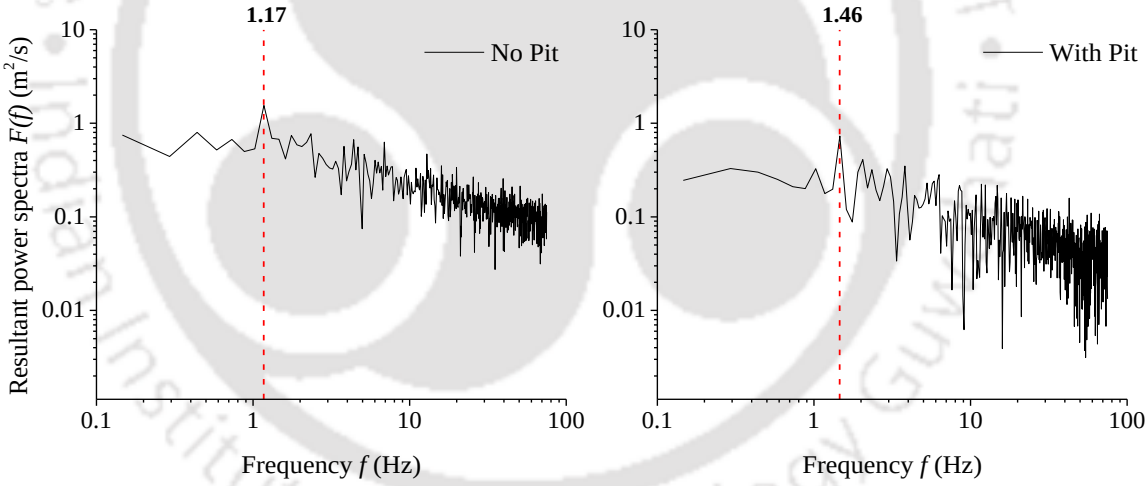

Figure 3.36 Resultant power spectra at the rear side of the oblong pier

Careful inspection of Figure 3.36 reveals that the vortices are shed across an array of frequencies. The dominant frequency associated with peak power was detected as the frequency of alternate shedding of vortices. Characteristic frequency of vortices observed in the case of a mining pit (1.46 Hz) is higher than that for the no pit case (1.17 Hz). Strouhal number obtained for the no pit case (0.24) is in accordance with the earlier studies (Clark, 2018). However, it escalates to 0.33 due to the excavation of an upstream

mining pit. Although the vibrational forces are not considered as a major cause of concern regarding the structural stability of the piers, the influence of sediment mining on the flow oscillations is noteworthy. Also, the deposition pattern and bedform dynamics behind the pier can alter due to mining, as it depends upon the nature of the oscillatory flow.

3.3.8 Summary

After traveling over a dredged pit, the flow has excess turbulent stresses and exerts greater shear on the streambed in the downstream side of the pit. Pit excavation provides a mechanism for greater mixing and momentum transport in the downstream flow. The fluctuations in the instantaneous velocities increase because of the pit and the downstream flow possess excess turbulent energy. This may cause streambed instabilities in the pier upstream.

As this high turbulent energy flow interacts with an oblong pier, stronger down-flow is initiated at the pier front. In this case, the horseshoe vortex zone formed in the local scour hole has enhanced negative velocities and excess turbulent shear stresses, compared to no-pit conditions. The amplification of the instantaneous bed shear beneath the turbulent horseshoe vortex (THV) zone is almost twice as compared to the no-pit case. This indicates that the dynamics of THV are also influenced by the pit excavation.

At the rear side of the pier, the mean streamwise velocities inside the scour hole zone increase due to pit excavation. For both cases, momentum transport across the depth at the rear flow region of the pier occurs due to inward and outward interaction type bursting events. Frequency of the vortex trail behind the pier amplifies, and the Strouhal number escalates from 0.24 to 0.33 due to pit excavation. Due to this increase in the dominance of inertial forces behind the pier, the pier body may be subjected to greater vibrational forces as well as the transport characteristics in this region may alter. Pit excavation causes the initiation of stronger ejection events in the down-flow zone at the upstream of the pier as well as stronger inward interaction events in the bed-proximity zone at the downstream side. There is an excess momentum flux (due to the stronger bursts) normal to a plane parallel to the flow direction due to pit excavation.

3.4 Effect of a Mining Pit on Turbulent Flow Characteristics Around Two circular piers in tandem arrangement

3.4.1 Experimental cases and data recording

In this section, turbulence parameters around two circular piers (75 mm diameter) in a tandem arrangement are presented. Data for two cases was analyzed [Figure 3.37(c) and 3.37(d)].

For the first case, two circular piers having 75 mm diameter (*d*) were embedded carefully in the sand bed in a tandem (inline) arrangement at a 6.0 m distance from the downstream end of the flume. (Ataie-Ashtiani & Beheshti, 2006) Ataie-Ashtiani and Beheshti (2006) stated that the proximity interference between the piers could be avoided by keeping the *L/d* ratio (spacing between the cylinders/diameter of the cylinders) in between 2 – 4. Therefore, the distance between these two piers (*L*) was kept 150 mm, such that *L/d* = 2.0.

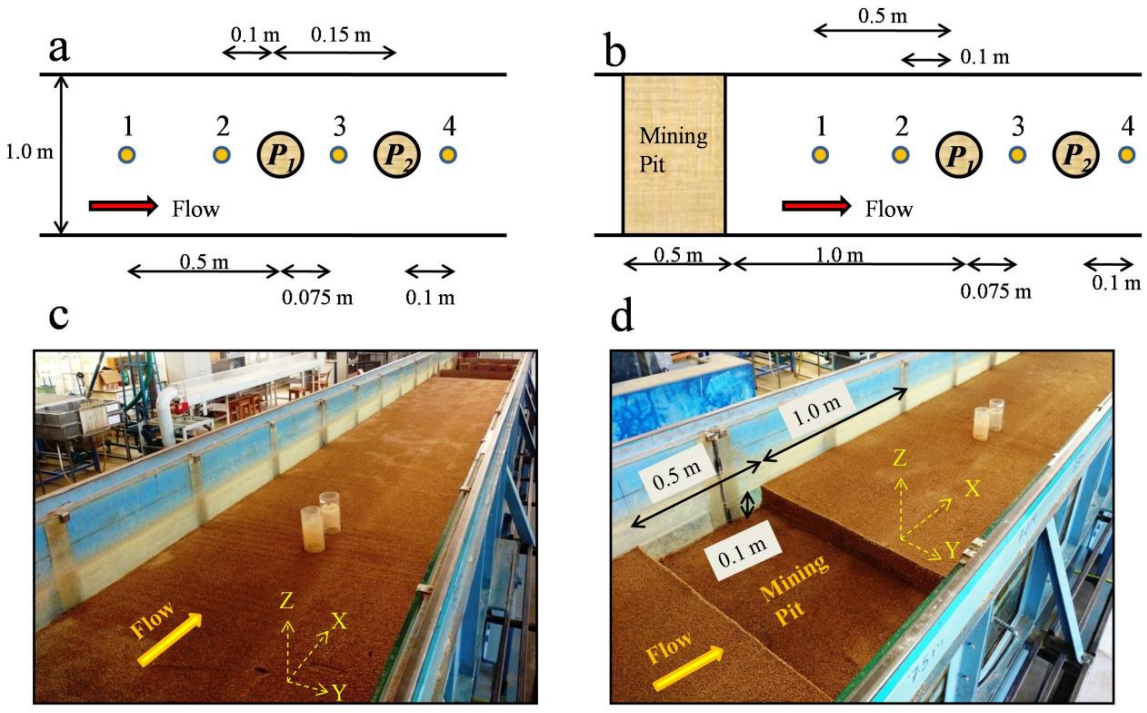

Figure 3.37 Schematic plan view of data recording locations for (a) No pit, (b) With Pit; Snapshots of experimental cases (c) No pit, (d) With pit around tandem piers.

In the second case, in addition to the tandem piers, a rectangular pit (dimensions: 0.5 m x 0.1 m) was excavated at 1.0 m upstream of the pier front to imitate the presence of mining in the channel. The pit was excavated before the initiation of flow in the channel so that steady flow conditions are not hampered during the experiment. Length of the pit along the flow direction was 0.5 m, its depth was 0.1 m, and it was excavated for the entire width of the channel, i.e., 1.0 m.

Velocity measurements at Q = 0.0441 m³/s were recorded along with the depth (Z-axis) at 4 critical locations along the centerline of the flume [Figure 3.37(a) and 3.37(b)]. Location-1 was 0.5 m upstream from the center of the pier front. It represents the location where flow approaches the piers after passing over the mining pit. Location-2 was 0.1 m upstream of the center of the pier front within the scour hole representing the region of horseshoe vortex. Location-3 was in the center of both the piers, and Location-4 was 0.1 m downstream of the rear pier.

3.4.2 Time-averaged flow field

For both the test cases, mean flow parameters such as mean streamwise velocity, turbulent stresses, and turbulent kinetic energy were calculated from filtered ADV data at Locations-1, 2, 3, and 4. The comparative profiles of these quantities along the normalized depth z/h are presented in this section.

Streamwise velocity profiles at Locations-1, 2, 3, and 4 are shown in Figure 3.38. Figure 3.38(a) represents a region at which the flow is moving towards the piers after passing over the pit (Location-1). At this location, the mean velocity in the inner layer is ~ 15% higher as compared to no pit case. As the flow strikes the pier front (*P1*), it is suddenly obstructed by the pier causing stagnation. Stagnation causes a pressure gradient along with the depth, and hence the flow moves in the downward direction along the pier. In the near-bed region, flow reversal takes place, and a horseshoe vortex is formed. This vortex at the base of the pier front picks up sediments along with it and causes erosion. Scour depth is directly proportional to the strength of this horseshoe vortex. Close observation of Figure 38(b) reveals that in the presence of a mining pit, stronger flow reversal occurs with higher negative velocities at the base of the pier front (*P1*). As a result of these

higher negative velocities, a stronger horseshoe vortex is formed (Melville, 1984). Therefore, excavation of a mining pit in the channel leads to greater scour depth and a higher volume of sediment extraction at the base of the pier front.

The nature of velocity profiles along the depth for both the cases at Location-2 is in agreement with previous studies (Kothyari & Kumar, 2012). In the central region of both the piers, mean velocities are higher near the bed up to $z/h \sim 0.3$, and above this depth, velocities drop significantly for both the experimental cases [Figure 3.38(c)]. In the presence of a pit, there is an overall rise of about 25 % in the mean velocity in this region (Location-3). Behind the rear pier (*P2*), i.e., at Location-4 [Figure 3.38(d)], the streamwise velocities are extremely low, indicating flow separation, which confirms the previous literature. The mean velocity profile in this region is nearly similar for both the experimental cases.

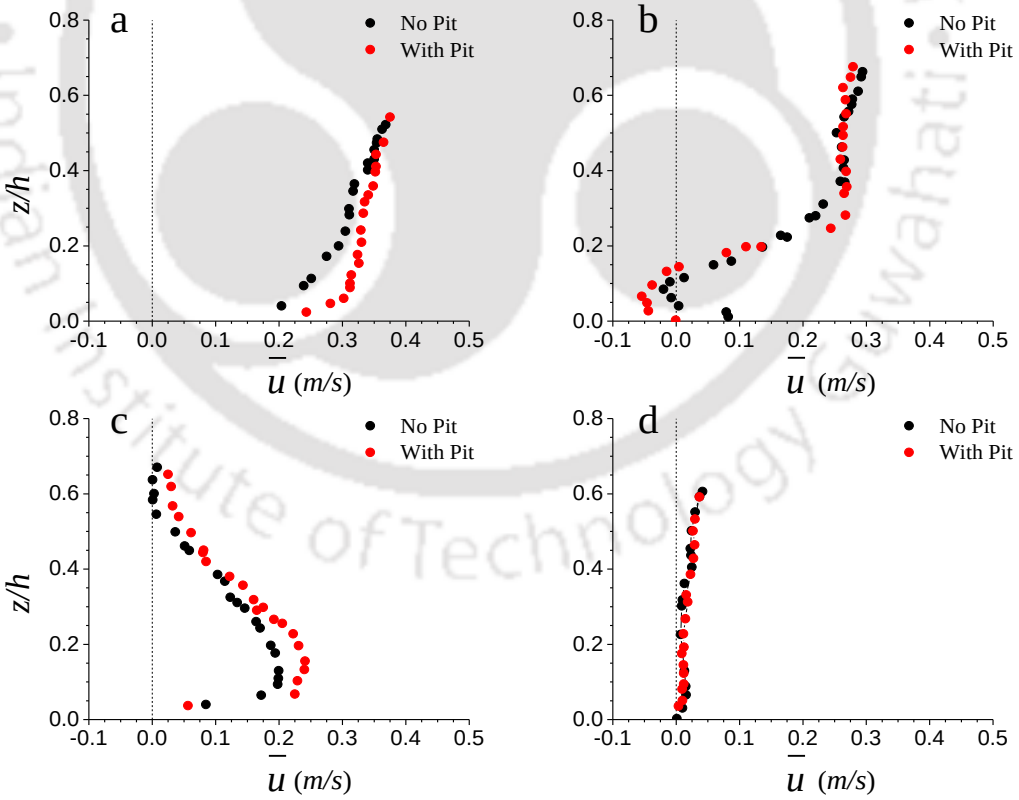

Figure 3.38 Streamwise mean velocity profiles at (a) Location-1, (b) Location-2, (c) Location-3, and (d) Location-4 around tandem pier.

The RSS profiles at Locations-1, 2, 3, and 4 are plotted in Figure 3.39. Excavation of a mining pit generates additional turbulence in the flow when it passes over the pit. Figure 3.39(a) indicates that the peak RSS of the flow approaching towards the pier after passing over the pit is about 1.5 times higher than the no pit case. Horseshoe vortex zone (from the bed level to z/h ~ 0.25) formed in the presence of a mining pit possesses about 20 % more RSS than the no pit case [Figure 3.39(b)]. At this location, RSS in the down-flow region (above z/h ~ 0.25) is also slightly greater in the presence of a pit. An escalation in RSS values (~ 15 %) has also been observed in between the two piers [Figure 3.39(c)], because of pit excavation. Behind the rear pier [Figure 3.39(d)], the contribution of inward and outward interaction towards the production of RSS is greater than sweep and ejection events; hence the RSS profile is negative throughout the depth for both the experimental cases. However, the presence of a mining pit doesn't cause any significant change in the RSS magnitudes in this region of flow.

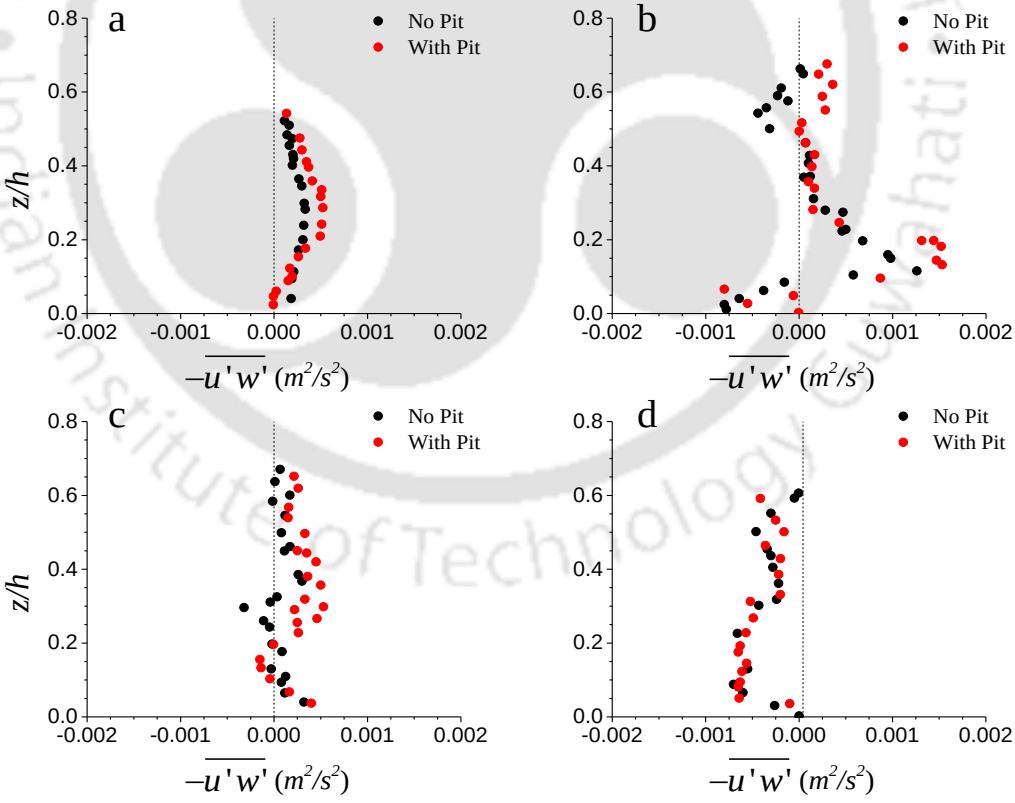

Figure 3.39 Streamwise Reynolds Shear Stress profiles at (a) Location-1, (b) Location-2, (c) Location-3, and (d) Location-4 around tandem piers.

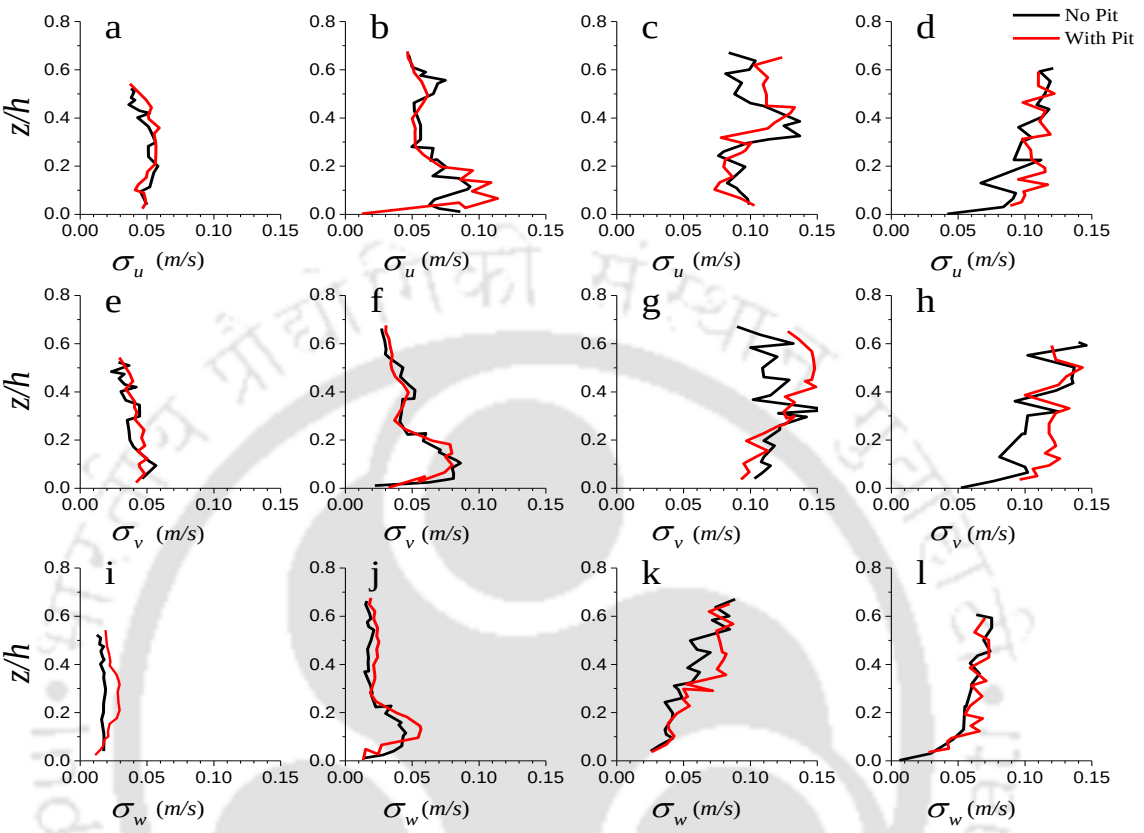

Figure 3.40 Streamwise turbulence intensity profiles at (a) Location-1, (b) Location 2, (c) Location-3, and (d) Location-4; transverse turbulence intensity profiles at (e) Location-1, (f) Location-2, (g) Location-3, and (h) Location-4; vertical turbulence intensity profiles at (i) Location-1, (j) Location-2, (k) Location-3, and (l) Location-4 around tandem piers.

Streamwise vertical and transverse turbulence intensities have been plotted in Figure 3.40. It is evident that after passing over the pit, flow approaches the piers with significantly higher vertical turbulent intensity (σ_w). The horseshoe vortex formed at the base of *P1* is highly turbulent in the case of a mining pit. In this zone (below $z/h \sim 0.2$), mean turbulent intensities in streamwise and vertical directions are about 20 % more than the no pit case [Figures 3.40(b) and 3.40(j)]. The nature of turbulence intensity profiles in this region is similar to the results of (Kumar & Kothyari, 2012).

The flow region between *P1* and *P2* is also characterized by a slight increase in σ_u and σ_w [Figures 3.40(c) and 3.40(k)], because of pit excavation. In this region, the average σ_v above *z/h* ~ 0.3 increases by 28% due to pit excavation. Within the separation zone behind *P2* [Figures 3.40(d), 3.40(h), and 3.40(l)], σ_u rises steeply in the near-bed region (up to *z/h* ~ 0.3) in the presence of a pit. The average σ_v in this region is about 30% more in case of a pit. This indicates that the vortex shedding intensity behind *P2* increases due to pit excavation.

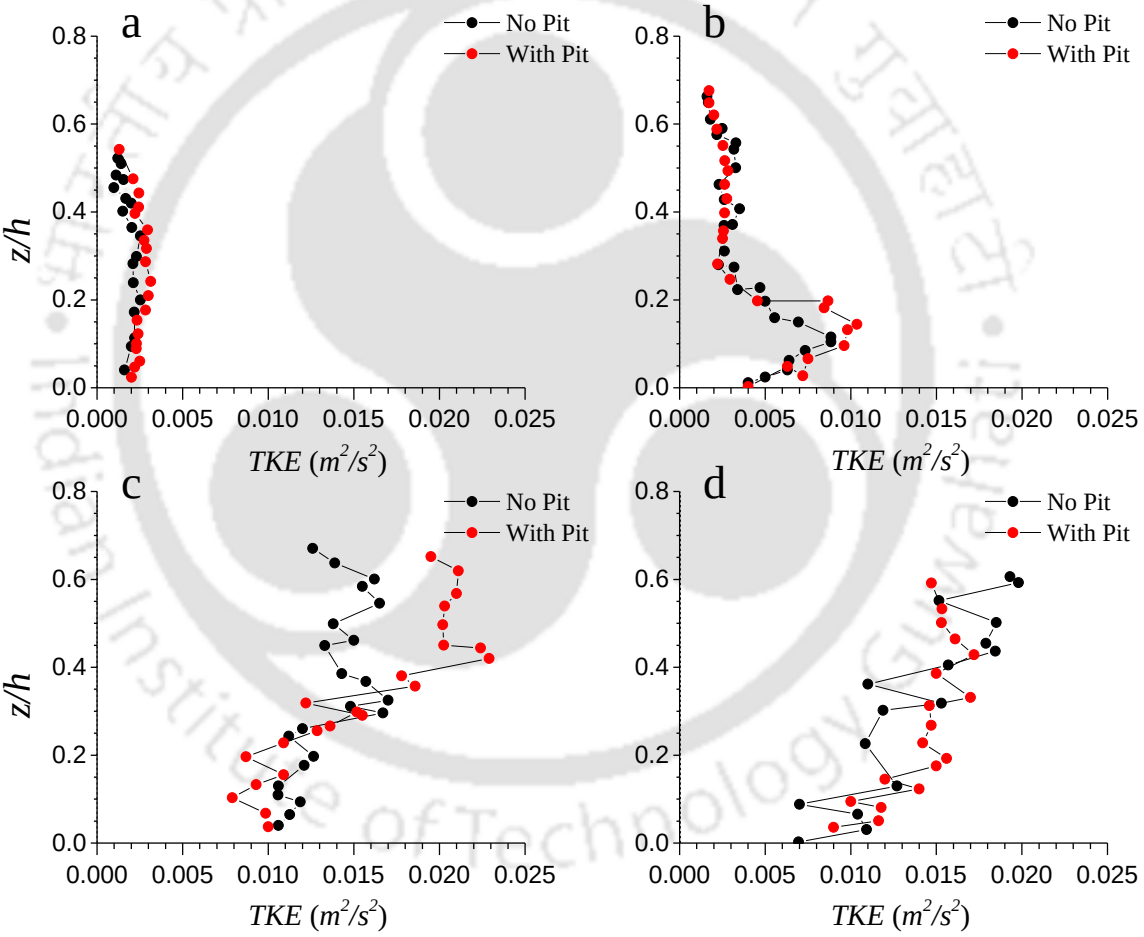

Figure 3.41 Turbulent kinetic energy (*TKE*) profiles at (a) Location-1, (b) Location-2, (c) Location-3, and (d) Location 4 around the tandem piers.

TKE profiles, along with normalized depth (*z*/*h*) at all 4 locations around the tandem piers, are presented in Figure 3.41. Examination of the figure reveals that *TKE* is higher in the zone of horseshoe vortex in front of *P1*, flow zone between *P1* and *P2*, and region behind *P2*, owing to higher velocity fluctuations. Pit acts as a source of turbulence to the flow downstream of the pit, where the piers are present. Therefore, *TKE* in the zone of horseshoe vortex is about 15% higher than the no pit case [Figure 3.41(b)]. Also, *TKE* in the flow zone between *P1* and *P2* and behind *P2* increased due to pit excavation.

Bed shear stress τ_0 and shear velocity u_*were evaluated based on the *TKE* approach as discussed Section 3.2.3, and the calculated values are mentioned in Table 3.7. Pit excavation results in an average rise of 15% in the bed shear stress around the piers.

Table 3.7 Bed shear stress and shear velocity at Locations1, 2, 3, and 4 around tandem piers.

Location	**Bed Shear Stress $\tau_0(N/m^2)$**		**Shear Velocity $u_*(m/s)$**	
	No Pit	**With Pit**	**No Pit**	**With Pit**
Location-1	0.304	0.418	0.0174	0.0204
Location-2	1.197	1.425	0.0346	0.0377
Location-3	2.014	1.900	0.0449	0.0436
Location-4	2.075	2.261	0.0455	0.0475

3.4.3 Summary

After passing over a pit, the flow approaches the tandem piers with higher mean velocities and increased turbulent stresses. The bed upstream of the piers was subjected to higher bed shear stresses in the presence of an upstream mining pit.

The interaction of this incoming flow with the pier front resulted in a stronger reversal zone at the base of the front pier. This led to the formation of a horseshoe vortex having higher turbulent kinetic energy and turbulent stresses compared to the no pit case. Pit excavation also increases the vortex shedding intensity behind the rear pier.

Chapter **4**

Streambed Instabilities around Bridge Piers in a Dredged Channel

4.1 Introduction

In this section, the morphological response of the streambed around a bridge pier is presented. Excavation of a mining pit significantly alters the flow field around bridge piers present on the downstream side. These alterations may influence the morphological features around bridge piers such as local scour, dune formation, etc. and cause streambed instabilities. The effects of two parameters of a mining pit on the streambed instabilities around a circular bridge pier are studied, namely distance of the pit from the pier and shape of the pit. Finally, the morphological behavior around two circular tandem piers in the presence of a mining pit is also presented in the end.

4.2 Mining Induced Streambed instabilities Around a Circular Pier

4.2.1 Experimental cases and data recording

Six sets of erodible bed experiments on the circular pier were analyzed for this study (Figure 4.1). For the 1st set of experiments, a circular cylinder-shaped pier of 75 mm diameter (d) was carefully embedded in the sand bed without any pit. For the next three sets of experiments, a rectangular-shaped pit with a depth of 10 cm (Figure 1) was carefully dug upstream of the cylinder to resemble the phenomenon of in-stream channel dredging. To study the effect of pit distance, three different distances of the pit from the pier (L) were tested (Set-2, Set-3 and Set-4), i.e., 3.0 m (L/d = 40.0), 2.0 m (L/d = 26.66) and 1.0 m (L/d = 13.33). In order to study the effect of pit shape, two more sets of experiments were analyzed (Set-5 and Set-6). For Set-5, a trapezoidal pit was excavated 1.0 m upstream of the circular pier, and for Set-6, an irregular shaped pit was excavated 1.0 m upstream of the circular pier. The volume of all three shapes of the mining pit was equal (0.05 m^3) as well as the depth of all three shapes was equal (100 mm).

For every test, the flow was gradually increased until steady flow conditions were established. For every set, tests were conducted for five different discharges to achieve fully turbulent flow conditions with Reynolds number greater than 10^4 (Muzzammil & Gangadhariah, 2003). The flow was maintained at sub-critical conditions. The hydraulic conditions used are presented in Table 4.1.

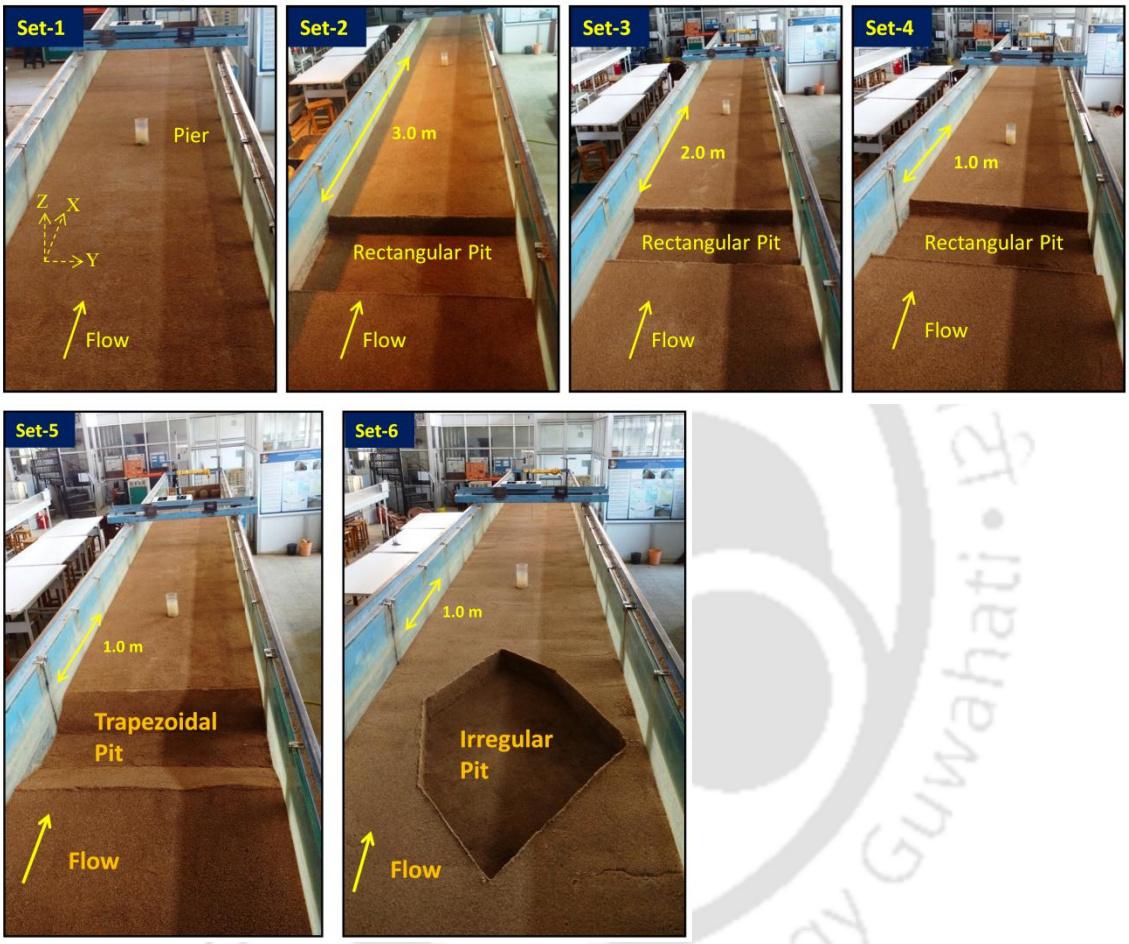

Figure 4.1 Snapshots of 6 experimental sets analyzed for the study of streambed instabilities

Scale effects shall arise as each and every force ratio in the experiment will not be exactly the same as the actual river flows. As gravity is the driving force of free surface flows in rivers, Froude number (*Fr*) becomes significant in the case of gravity flow experiments. Field measurements (Bathurst, 1985; Nikora & Smart, 1997) reported a wide range of Froude numbers for river flows (*Fr* = 0.1 - 0.8). In this context, we maintained subcritical flow conditions (*Fr* = 0.4 - 0.5). Also, the flow was maintained in a rough

turbulent regime (Flow Reynolds number $Re > 10^4$; Shear Reynolds number $R^* > 70$), as the flow characteristics are independent of Reynolds number in this regime.

Clear-water scour was observed for no pit experiments as the bed particles were not in motion. However, when a pit was dredged in the sand bed, the edges of the pit were gradually eroded by the flow. The sediments at the downstream end of the pit were in motion, where the pier was located; therefore, active-bed scour was observed in this case. Local scouring is a nonlinear temporal process, and the scour depth almost attained equilibrium after a certain period of time. Even after this stage, sediments eroded in the downstream of the pit continued to transport, and some of them were deposited in the local scour hole at the pier front. The experiments were stopped once the sediment transport rate was negligible. Water was gradually drained out of the flume at the end of the experiments. The bed elevations around the pier were recorded using a digital point gauge (Mitutoyo Corp.®) having an accuracy of 0.01 mm.

Table 4.1 Hydraulic conditions of all the experimental cases analyzed for the study of streambed instabilities.

Set	Discharge (m^3/s)	Distance between pit and pier (L)	Depth-averaged approach flow velocity (m/s)	Froude Number Fr	Reynolds number Re	Shear Reynolds number R^*
No Pit [Set-1]	0.0382	-	0.382	0.422	35768	89
	0.0441		0.420	0.455	40951	91
	0.0472		0.429	0.456	43470	93
	0.0503		0.437	0.457	45949	95
	0.0567		0.473	0.485	51377	96
Rectangular Pit [Set-2]	0.0382	3.0 m	0.382	0.422	35768	89
	0.0441		0.420	0.455	40951	91
	0.0472		0.429	0.456	43470	93
	0.0503		0.437	0.457	45949	95
	0.0567		0.473	0.485	51377	96
Rectangular Pit [Set-3]	0.0382	2.0 m	0.382	0.422	35768	89
	0.0441		0.420	0.455	40951	91
	0.0472		0.429	0.456	43470	93
	0.0503		0.437	0.457	45949	95
	0.0567		0.473	0.485	51377	96
Rectangular Pit [Set-4]	0.0382	1.0 m	0.382	0.422	35768	89
	0.0441		0.420	0.455	40951	91
	0.0472		0.429	0.456	43470	93
	0.0503		0.437	0.457	45949	95
	0.0567		0.473	0.485	51377	96
Trapezoidal Pit [Set-5]	0.0441	1.0 m	0.420	0.455	40951	91
	0.0472		0.429	0.456	43470	93
	0.0503		0.437	0.457	45949	95
	0.0567		0.473	0.485	51377	96
Irregular Pit [Set-6]	0.0441	1.0 m	0.420	0.455	40951	91
	0.0472		0.429	0.456	43470	93
	0.0503		0.437	0.457	45949	95
	0.0567		0.473	0.485	51377	96

4.2.2 Effect of distance of pit from the pier on the streambed morphology

Results of 4 sets of experimental cases are presented in this section, i.e. no pit case and rectangular pit at all three distances i.e., 3.0 m (L/d = 40.0), 2.0 m (L/d = 26.66) and 1.0 m (L/d = 13.33).

The effects of channel dredging on the streambed morphology around the pier can be observed in Figures 4.2 – 4.7. The cross-section and longitudinal section of streambed along the centerline of the circular pier are plotted in Figure 4.2. The contour plots of the streambed morphology around the circular pier at various Reynolds numbers are illustrated in Figures 4.3 – 4.7. Results were plotted considering the origin as the center of the pier, Flow direction as *X*, transverse direction as *Y*, and depth as the *Z* direction. The initial bed level before the experiment was considered as a datum for plotting contours.

It is evident from these plots that the morphological effects of in-stream mining are not localized in a particular region but observed over the entire streambed on the downstream side of the mining pit. As reported in the previous chapter, there is increased flow turbulence and excess bed shear on the streambed downstream of a pit. Due to a dredged zone, transport of momentum across the flow depth increases, which causes higher turbulent stresses in downstream of the dredged zone. On account of these flow alterations, excess erosion occurred inside the local scour hole in the transverse direction, causing the exposure of the pier (Figure 4.3). The streambed in the approach zone of the pier also eroded, causing a lowering of bed elevation in front of the pier. The streambed behind the pier also eroded in the presence of a dredged zone, which can be observed in Figure 3. These effects were most significant when the mining zone was closest to the pit (L/d = 13.33).

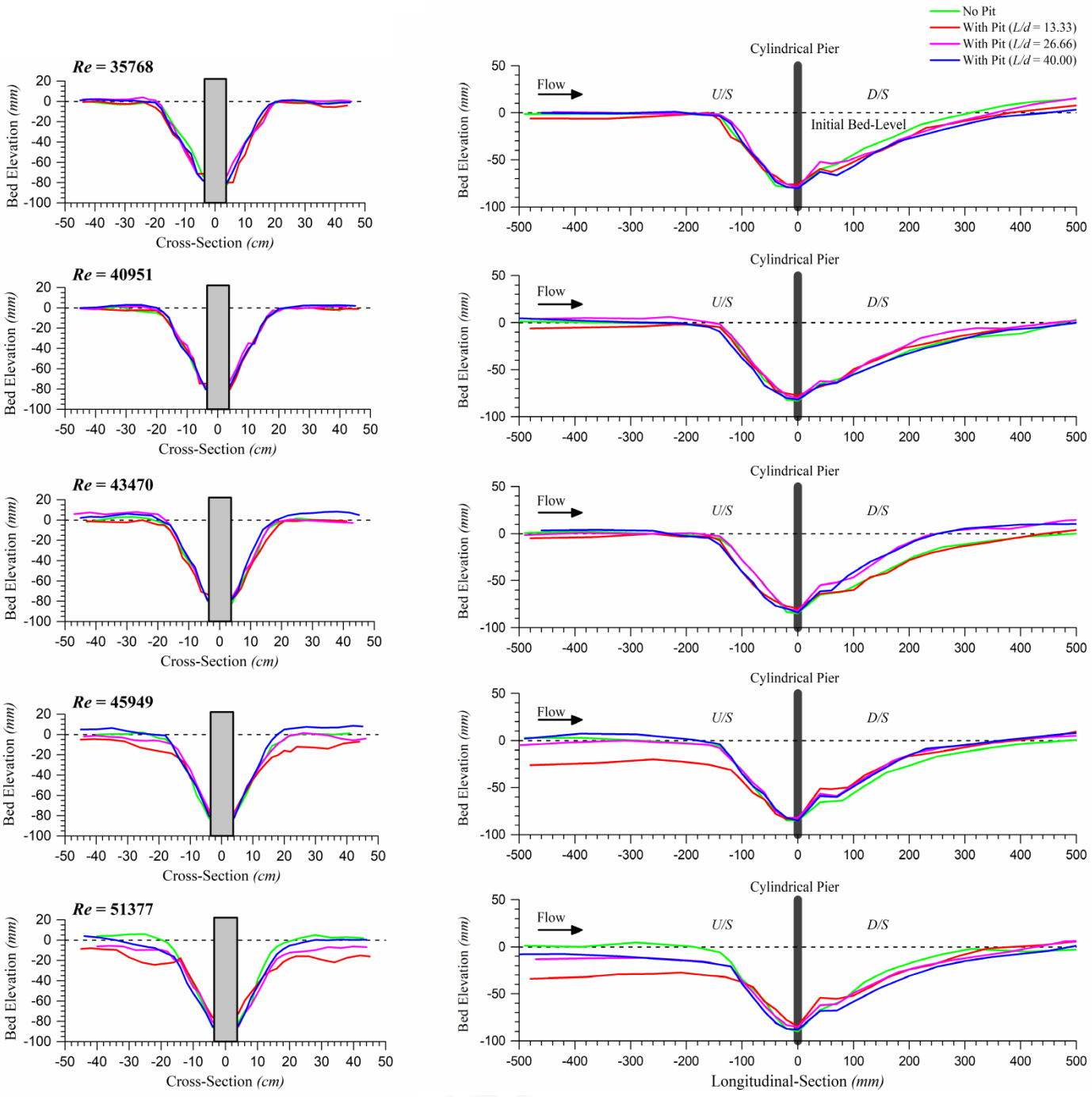

Figure 4.2 Cross-section and longitudinal-section of streambed along the center line of the circular pier of all the tests with rectangular pit at various Reynolds number (*Re*).

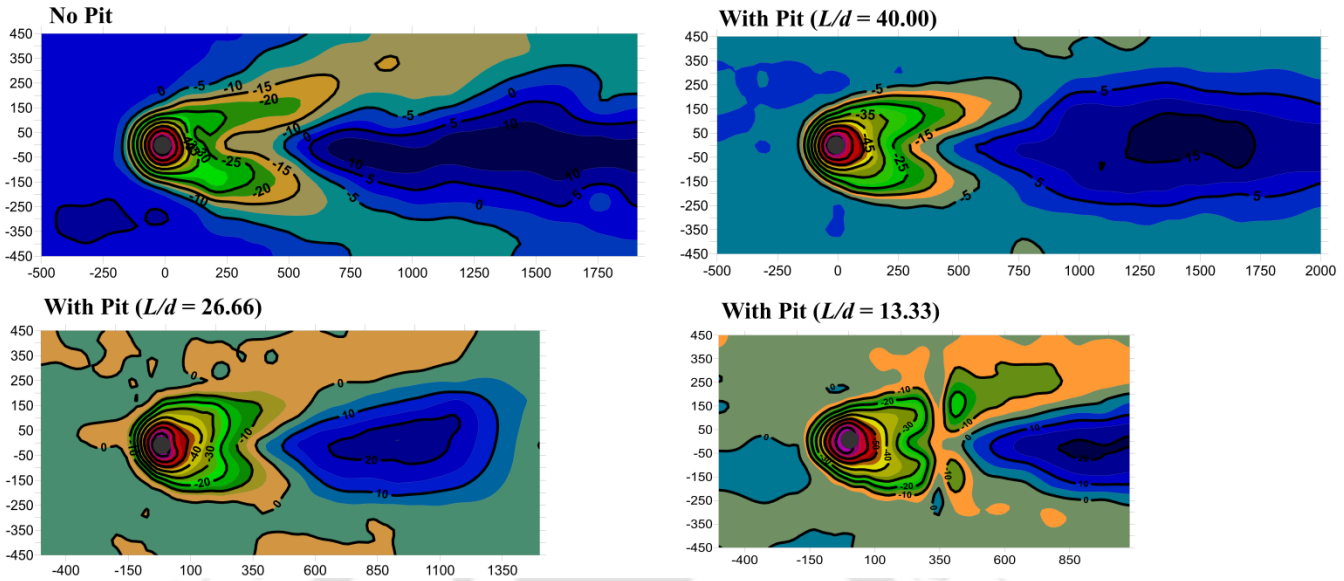

Figure 4.3 Contour plots of the streambed morphology around the pier for all 4 test cases at Reynolds number (*Re*) = 35768.

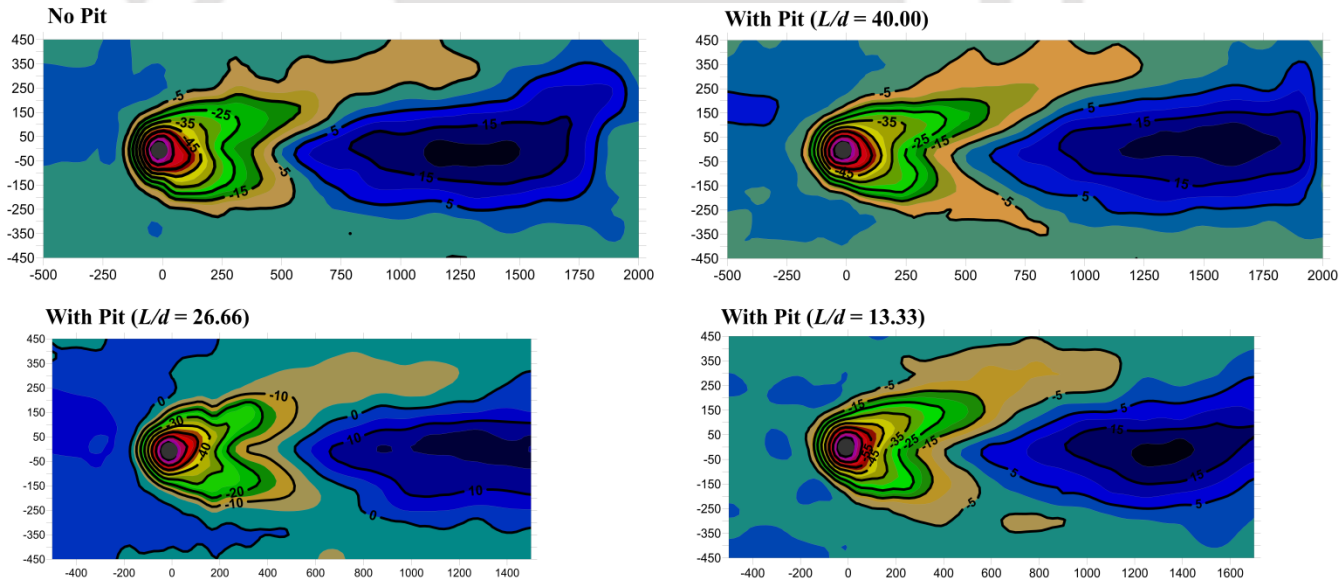

Figure 4.4 Contour plots of the streambed morphology around the pier for all 4 test cases at Reynolds number (*Re*) = 40951.

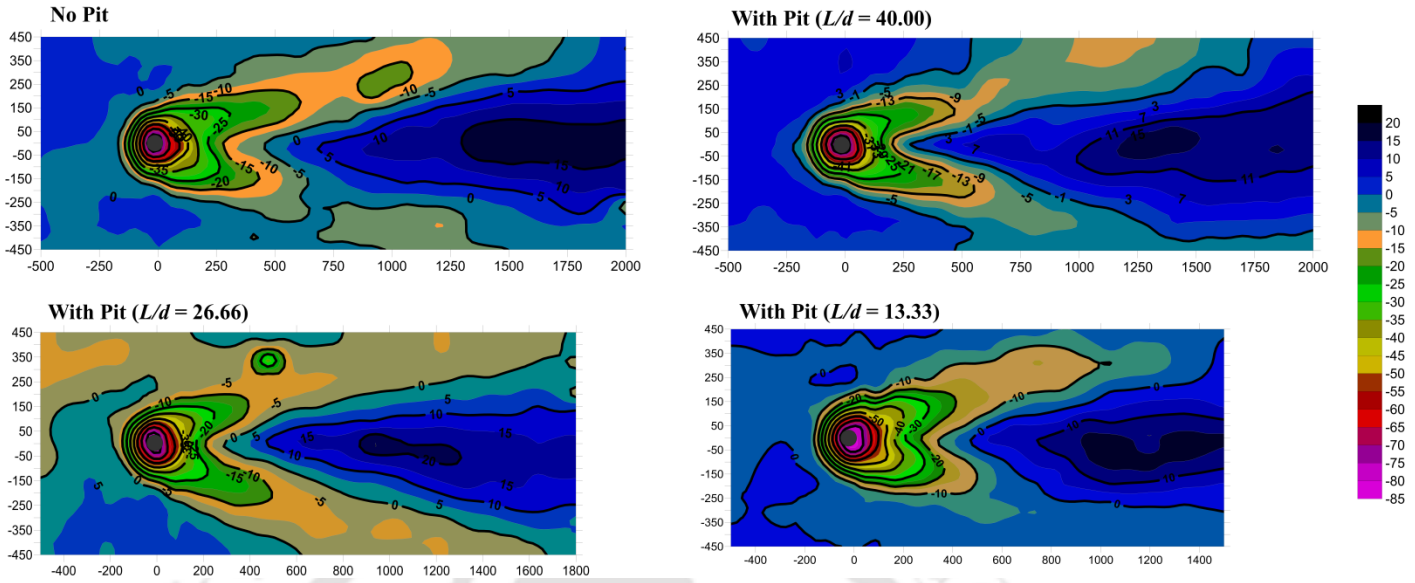

Figure 4.5 Contour plots of the streambed morphology around the pier for all 4 test cases at Reynolds number (*Re*) = 43470.

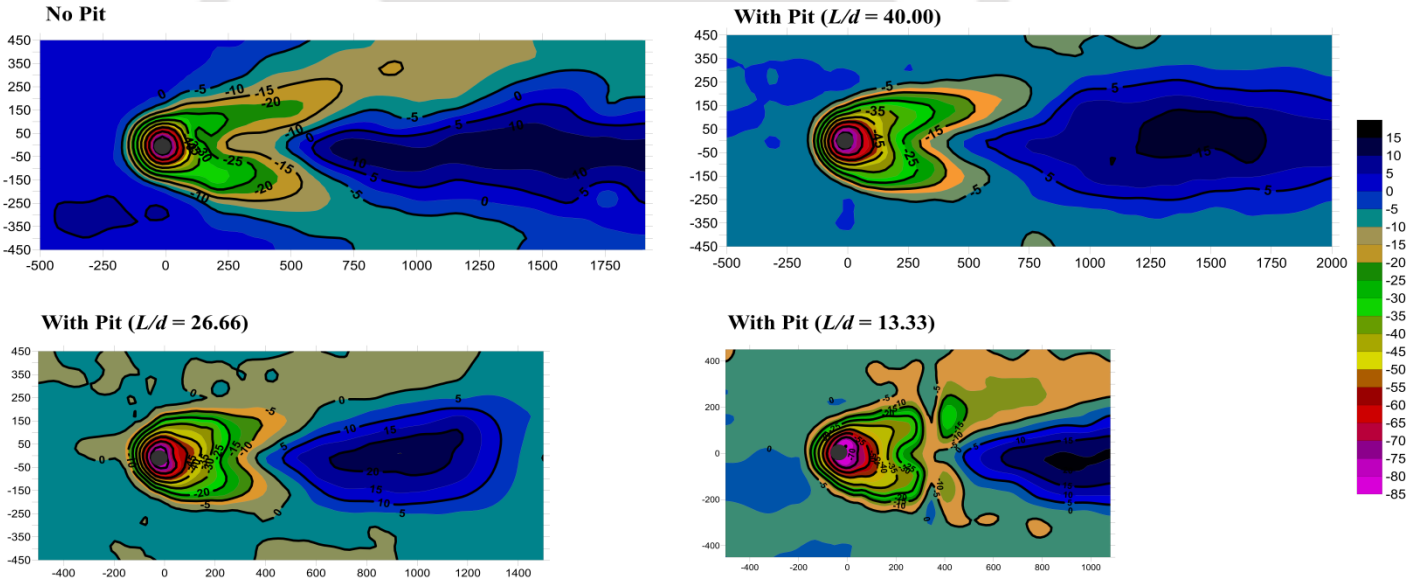

Figure 4.6 Contour plots of the streambed morphology around the pier for all 4 test cases at Reynolds number (*Re*) = 45949.

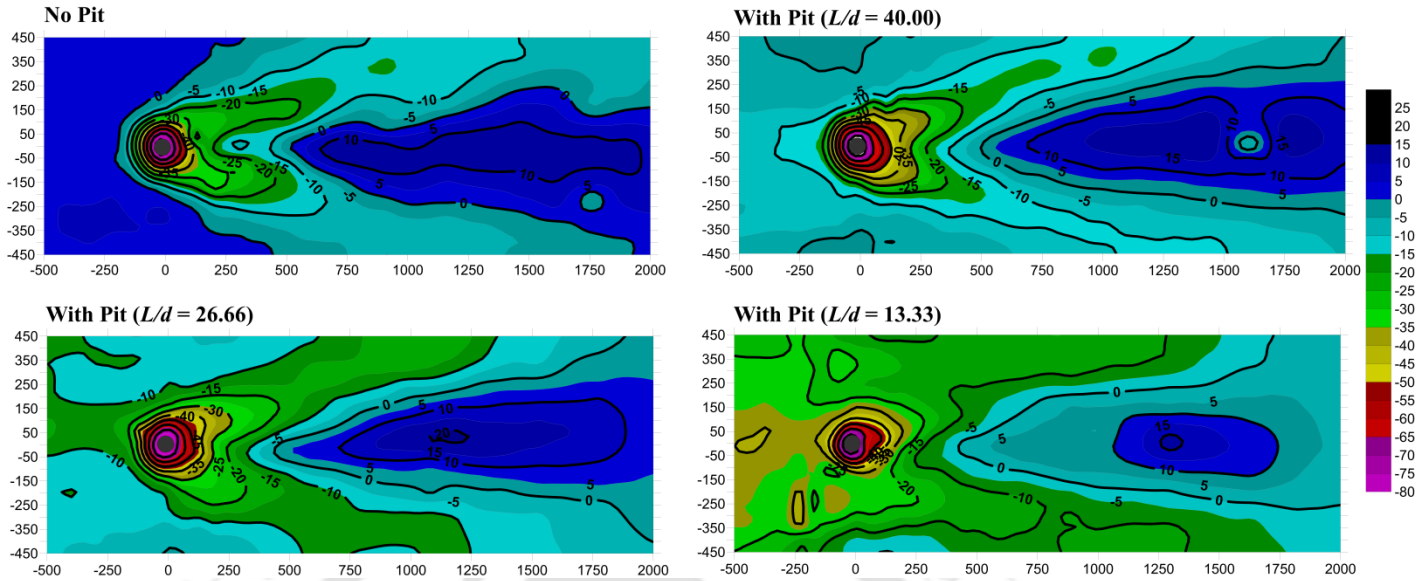

Figure 4.7 Contour plots of the streambed morphology around the pier for all 4 test cases at Reynolds number (*Re*) = 51373.

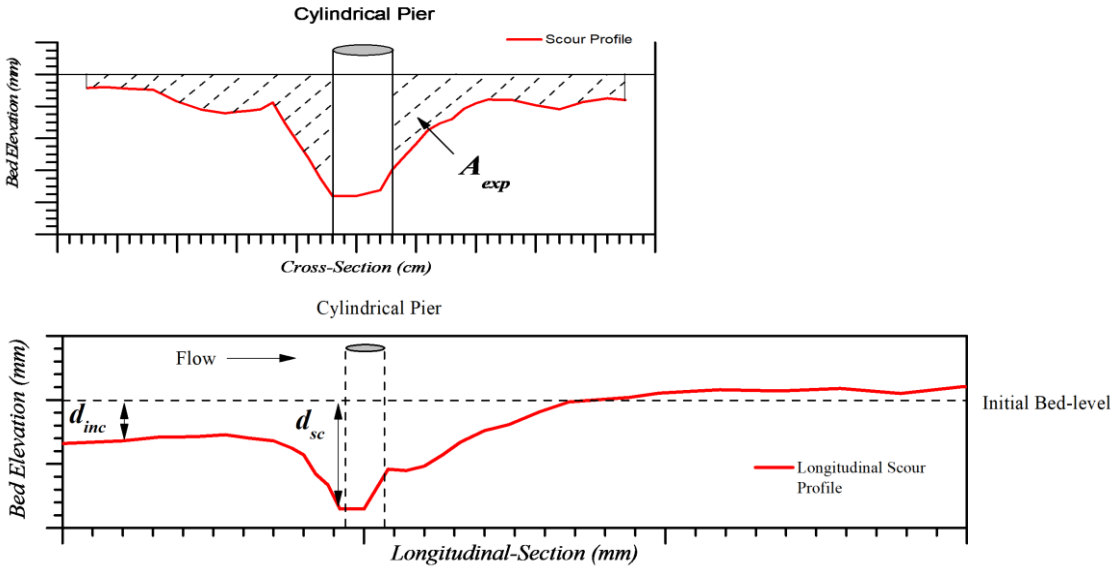

Figure 4.8 Sketch showing morphological parameters including maximum scour depth (d_{sc}) at the pier front, Exposure area (A_{exp}) along pier cross-section and incision depth (d_{inc}) of upstream bed, because of a mining pit.

The streambed instability around the pier was quantified by two morphological parameters, namely exposure factor (E) and normalized upstream incision (d_{inc}/d_{sc}). Exposure factor (E) is defined as $E = A_{exp}/A_{\exp\ (No\ Pit)}$ and normalized upstream incision depth is defined as d_{inc}/d_{sc}, where A_{exp} is the area of erosion in the pier cross-section, d_{sc} is the maximum frontal scour depth at the pier base, and d_{inc} is the depth of incision observed on the bed upstream of the pier (Figure 4.8). For calculating the pier exposure factor (E) for every case, the exposure area calculated (A_{exp}) was divided by the exposure area for the same discharge when no pit was excavated [$A_{exp\ (\text{No Pit})}$]. Thus, the exposure factor without any pit would be equal to 1 for every discharge.

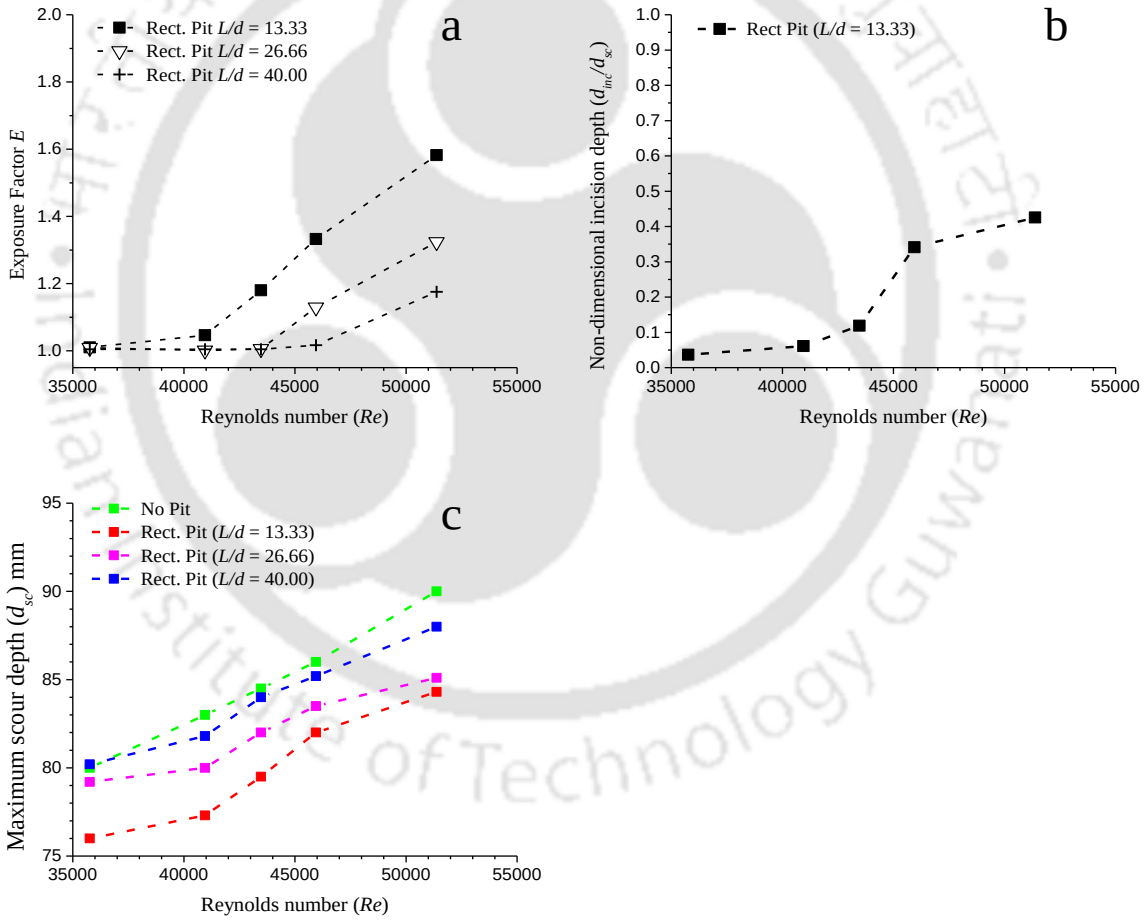

Figure 4.9 a. Variation of Exposure factor (E) with Reynolds number [for L/d =13.33, 26.66 and 40.00] b. Variation of non-dimensional incision depth (d_{inc}/d_{sc}) with Reynolds number [for L/d =13.33] c. Variation of maximum scour depth (d_{sc}) with Reynolds number [for L/d =13.33, 26.66 and 40.00]

It can be observed from Figure 4.9(a) that the exposure factor strongly depends upon the Reynolds number as well as the distance of the pit from the pier. The maximum exposure factor was observed when the mining zone was closest to the pier (L/d = 13.33). However, when the mining zone was 2 and 3 m upstream of the pier, i.e., $L/d \geq 26.66$, pier exposure was significant only when the Reynolds number exceeds 45000. Thus, excavation of a mining pit very close to the pier can critically expose the pier. The lowering of the streambed upstream of the pier or upstream incision was also observed for L/d =13.33. The normalized upstream incision depth escalates to as high as 0.4 beyond a Reynolds number of 45000 [Figure 4.9(b)]. This indicates critical erosion and lowering of channel bed in the approach zone of the pier due to close proximity mining. For $L/d \geq 26.66$, mining pit excavation does not affect the bed morphology upstream of the pier critically.

The local scour occurring on the frontal pier base was caused due to turbulent horseshoe vortices. It was a temporally continuous phenomenon wherein the bed particles were lifted up from the pier base and swept along by the vortices until equilibrium was reached. Basically, channel dredging acts as a source of turbulence to the downstream flows. When such highly turbulent flow interacted with the bridge pier located downstream of the pit, stronger horseshoe vortices were formed at the pier base, and they caused excessive erosion around the pier. Local scour region around the pier attained quasi-equilibrium after a certain period of time. The sediments eroded in the downstream of the pit continued to transport downstream, and some of the sediments were deposited in the local scour hole at the frontal side. Therefore the maximum scour depths at the end of the experiments measured at the frontal side of the pier slightly decreased [Figure 4.9(c)]. Filling of the scour hole directly depends upon the distance of the pit from the pier. Filling of the scour hole increased, and consequently, the maximum scour depth decreased as the mining occurred near the pier. The behavior of scour depth under the influence of a dredged zone was similar to the live-bed scour condition. However, in-stream mining has more of a ‘global’ erosive effect on the entire streambed morphology around the pier.

4.2.3 Effect of shape of the pit on the streambed morphology

The study of a rectangular pit indicated that the streambed instabilities are maximum when the pit was excavated closest to the pier, i.e., L/d =13.33. Therefore two more shapes of the pit, i.e., trapezoidal and irregular, were tested at 1.0 m (L/d =13.33) for Set-5 and Set-6. The effect of the shape of pit on the streambed instabilities is presented in this section by analyzing rectangular pit, trapezoidal pit, and irregular pit cases at L/d =13.33.

The cross-section and longitudinal-sections of the streambed profile along the center of the pier are plotted in Figure 4.10 and 4.11, respectively. The contour plots of the streambed morphology around the circular pier for all three shapes of the mining pit are shown in Figure 4.12 – 4.15. The overall pattern of erosion around the circular pier was almost consistent for all the three shapes of the mining pit. Exposure of the pier in the transverse direction, as well as the incision of streambed in front of the pier, was observed in the case of all three shapes of the pit. The extension of the zone of erosion in the downstream side of the pier was also consistent in all three cases.

However, there was a slight effect of the pit shape as far as the severity of the excess erosion is concerned. The effect of rectangular and trapezoidal shaped pits was almost similar, but erosion due to the irregular pit was slightly less severe. This variation can be observed by careful observation of the morphological plots. A strong possibility for this behavior can be the difference in the width of the pit. Both rectangular and trapezoidal pits are 1.0 wide; however, the average width of the irregular pit is about 0.74 m. This hypothesis is supported by earlier studies, which reported that the morphological effects directly depend upon the width of the mining pit (Neyshabouri et al., 2002).

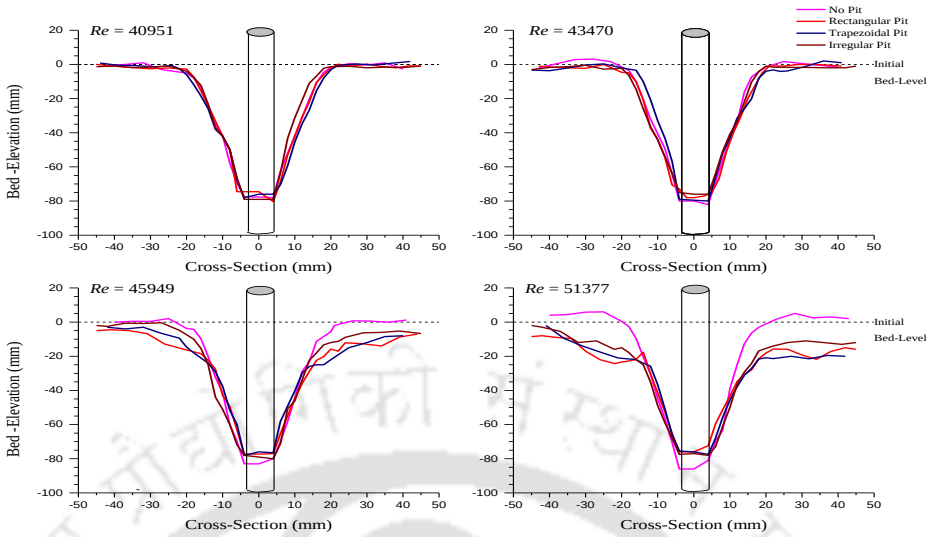

Figure 4.10 Cross-sectional profiles of streambed along the center of the circular pier for various pit shapes.

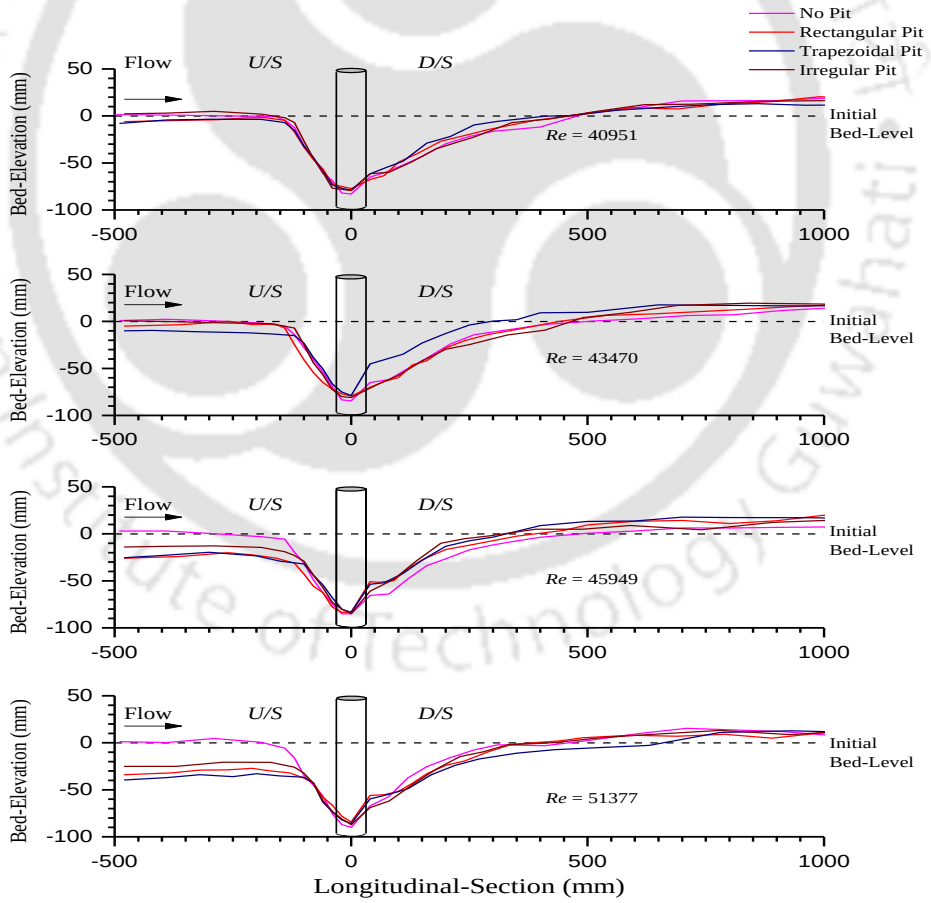

Figure 4.11 Longitudinal-section profiles of streambed along the center of the circular pier for various pit shapes.

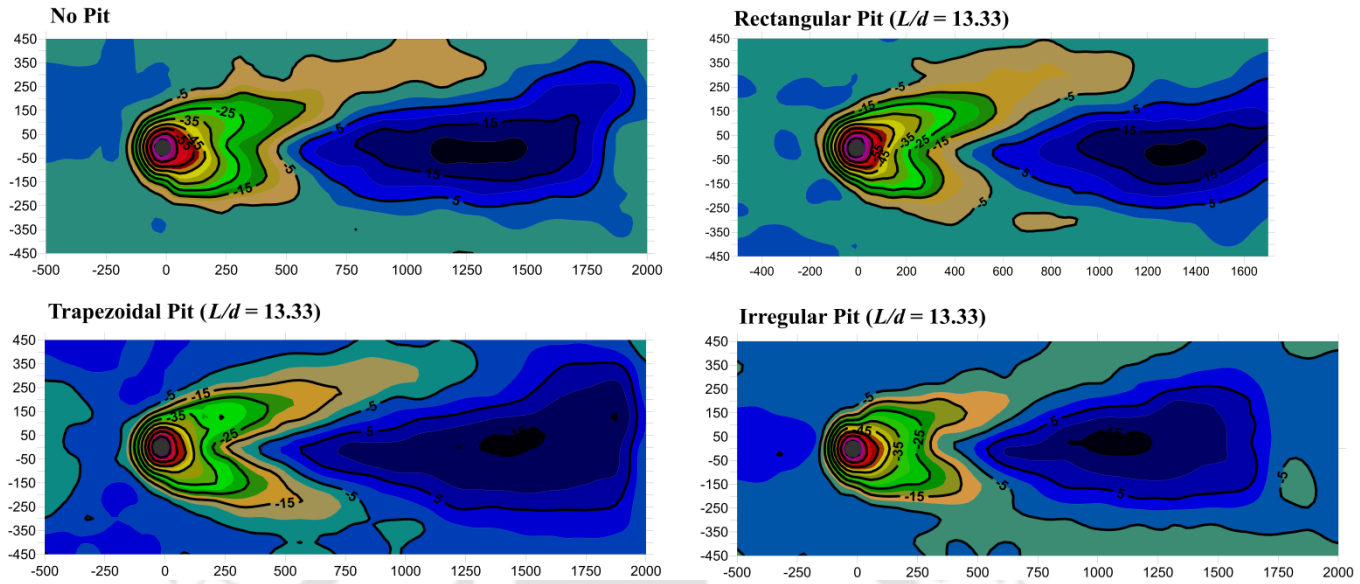

Figure 4.12 Contour plot of the streambed morphology around the circular pier for various shapes of mining pit at *Re* = 40951.

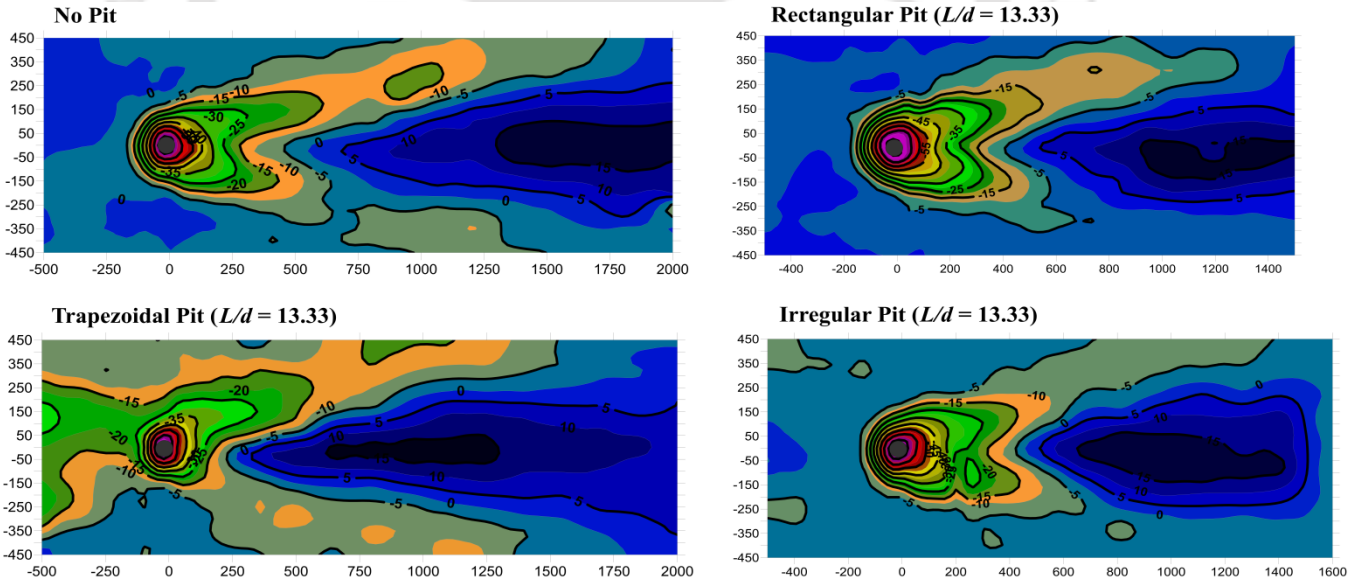

Figure 4.13 Contour plot of the streambed morphology around the circular pier for various shapes of mining pit at *Re* = 43470.

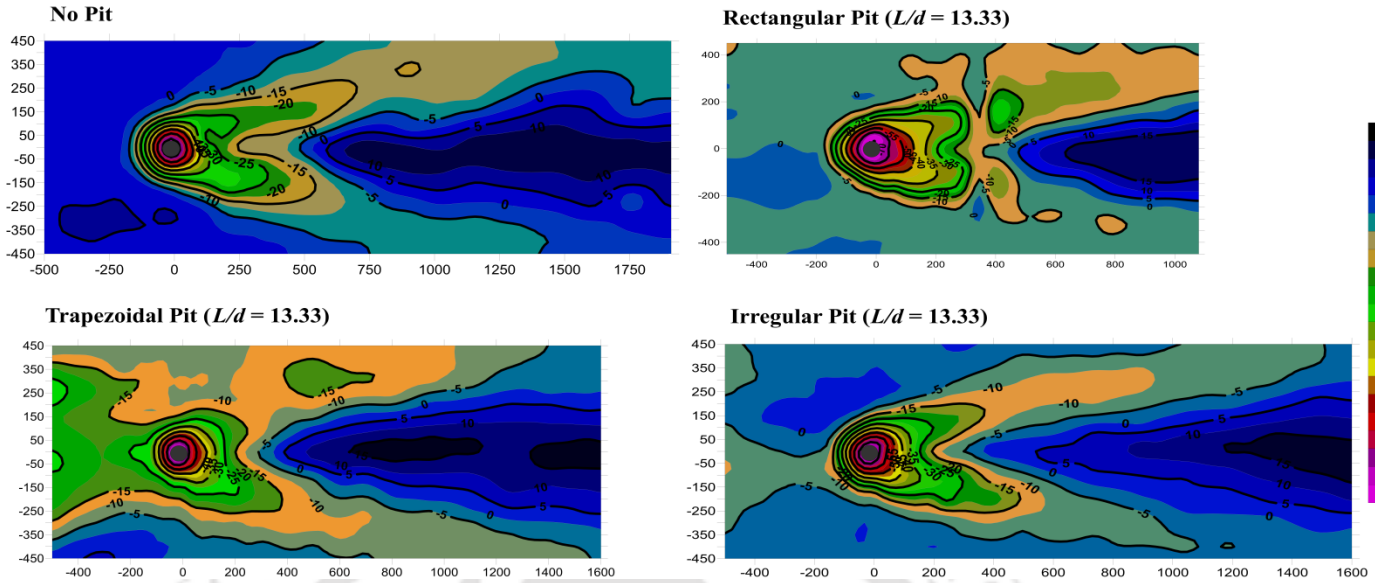

Figure 4.14 Contour plot of the streambed morphology around the circular pier for various shapes of mining pit at *Re* = 45949.

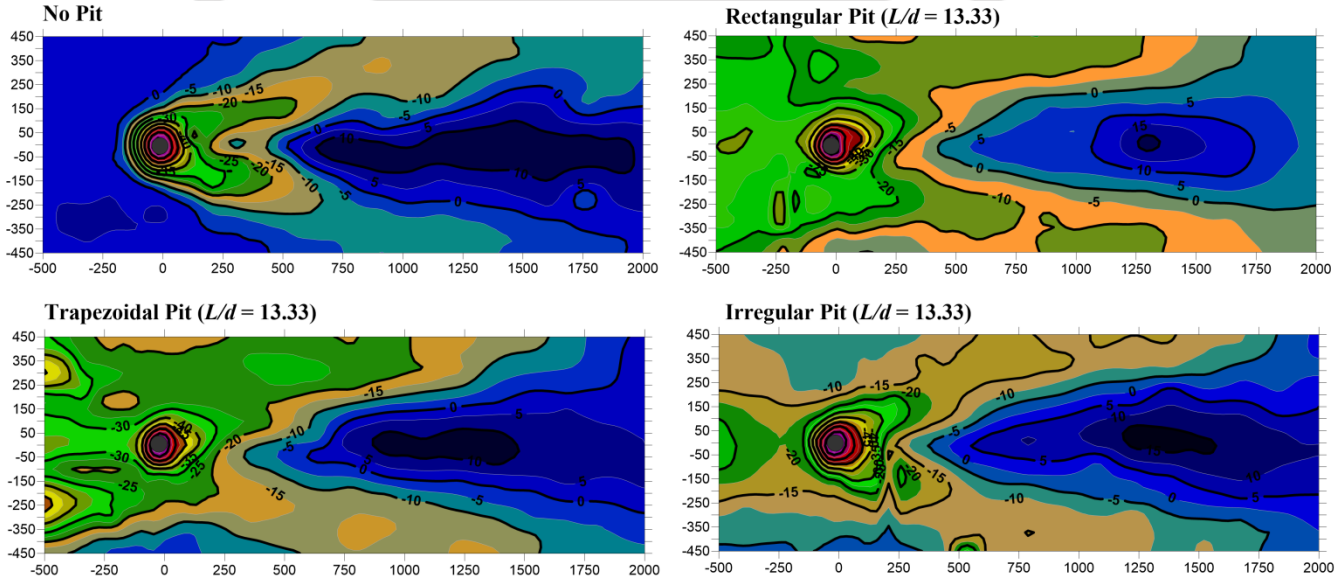

Figure 4.15 Contour plot of the streambed morphology around the circular pier for various shapes of mining pit at Re = 51373.

The effect of pit shapes on the transverse exposure of pier caused due to excessive erosion is quantified in Figure 4.16(a). The Exposure factor (E) increased almost linearly with the Reynolds number, for all three shapes of the pit. The Exposure factors for rectangular and trapezoidal pits were almost similar for all the Reynolds number, crossing a value of 1.5 for Re > 50000. It indicates that in high flow cases, mining pits can cause more than 50 % lateral exposure of the pier. However, for the irregular shaped pit, E was reduced by about 10 % as compared to rectangular and trapezoidal shaped pits.

A similar trend was observed for non-dimensional incision depth (d_{inc}/d_{sc}), plotted in Figure 4.16(b). The normalized incision depth at the upstream of the pier was similar for rectangular and trapezoidal pits and reached a maximum value of but reduced to a maximum of around 0.45. However, this maximum value of normalized upstream incision depth was reduced to about 0.3 in the case of an irregular pit.

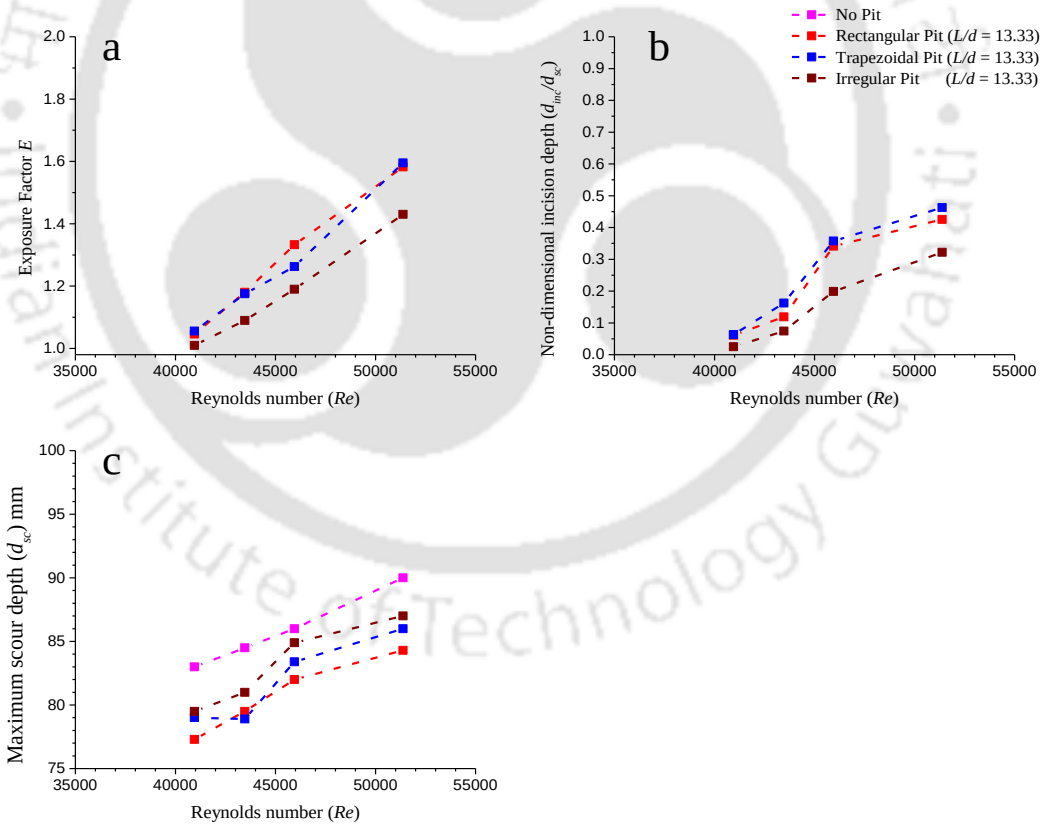

Figure 4.16 a. Variation of Exposure factor (E) with Reynolds number b. Variation of non-dimensional incision depth (d_{inc}/d_{sc}) with Reynolds number and c. Variation of maximum scour depth (d_{sc}) with Reynolds number for all three shapes of mining pits.

4.2.4 Summary

Dredging a pit caused morphological instabilities around the pier present downstream. The pit resulted in excessive erosion and exposure of the pier as well as bed lowering in the approach zone of the pier. The streambed instability around the pier was a function of the Reynolds number (*Re*) as well as the distance between the pier and the mining zone (*L/d*). Dredging of a pit very close to the pier (*L/d* = 13.33) was critical as the pier exposure factor can reach as high as 1.5, and the normalized depth of bed lowering in the approach zone can reach 0.4. For $L/d \geq 26.66$, pier exposure was only significant for high Reynolds numbers ($Re > 45000$). Dreading of a pit caused the filling of the scour hole at the frontal side of the pier. Therefore, the maximum scour depths measured at the pier base were slightly lowered in the presence of a mining pit.

Three shapes of a mining pit were compared on the basis of these morphological instability parameters, namely rectangular, trapezoidal, and irregular. Morphological response of the streambed around a circular pier was almost similar in the case of rectangular and trapezoidal pits, which had the same widths. However, the severity of streambed instabilities was slightly decreased in the case of an irregular pit, which had a lesser width. Thus, pier exposure and upstream incision depth can be affected by the width of mining pits. In-stream mining activities, especially in the proximity of a bridge pier, have the potential to erode the streambed around the pier and may contribute to its failure.

4.3 Effect of a Mining Pit on the Morphodynamics Around Two Circular Pier in Tandem

4.3.1 Morphology around tandem piers

In this study, the morphological behavior of two test cases (Section 3.3) is analyzed (Figure 4.17). For the first case, two circular piers having 75 mm diameter (*d*) were embedded carefully in the sand bed in a tandem (inline) arrangement at 6.0 m distance from the downstream end of the flume. In the second case, in addition to the tandem piers, a rectangular pit (dimensions: 0.5 m x 0.1 m) was excavated at 1.0 m upstream of

the pier front to imitate the presence of mining in the channel. The morphological features around the tandem piers are presented for a flow discharge of Q = 0.0441 m³/s.

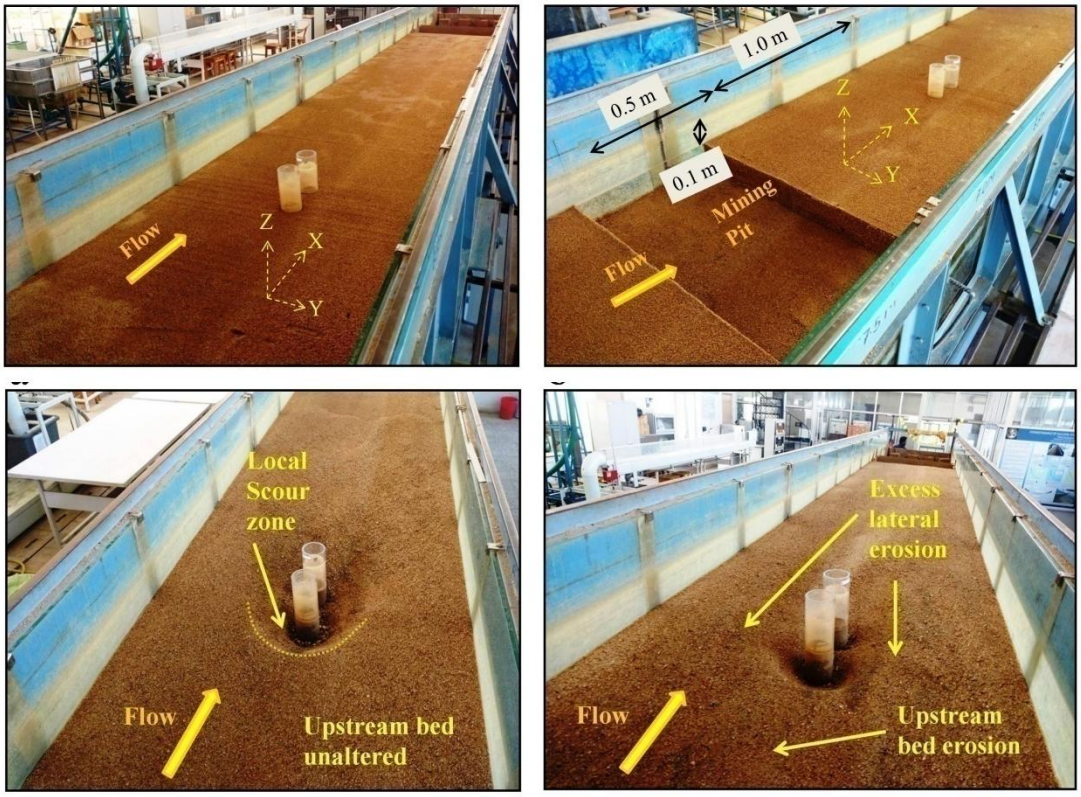

Figure 4.17 Snapshot of tandem piers before and after the experiments for no-pit case (left) and with-pit case (right).

Table 4.2 Statistics of the morphological features around tandem piers

Case	Maximum scour depth at P_1(mm)	Maximum scour depth at P_2(mm)	Scour volume (mm^3)	Average upstream bed level (mm)	Distance of dune crest from P_1(mm)
No Pit	79.2	60.0	12735436.5	-03.0	1200
With Pit	80.7	59.5	19678061.8	-25.0	1750

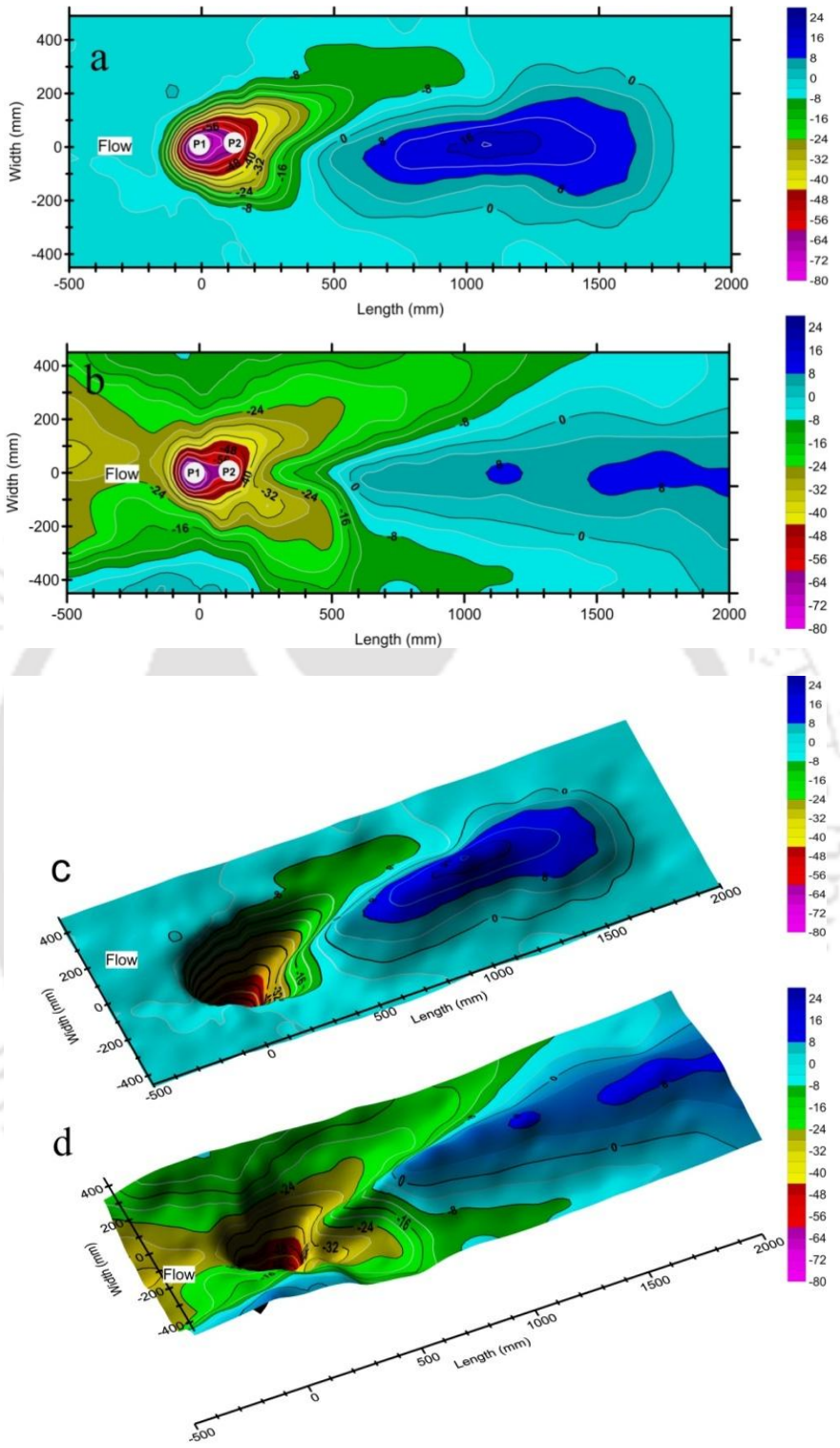

Figure 4.18 Contour plan of streambed morphology around tandem piers for (a) No pit and (b) With pit case; as well as the perspective plot for (c) No pit and (d) With pit case

The contour plots of streambed morphology around the tandem piers are shown in Figure 4.18, and the statistics of morphological features are provided in Table 4.2. The cross-section and longitudinal section along the centerline of the piers are plotted in Figure 4.19. Initial bed level was considered as the datum.

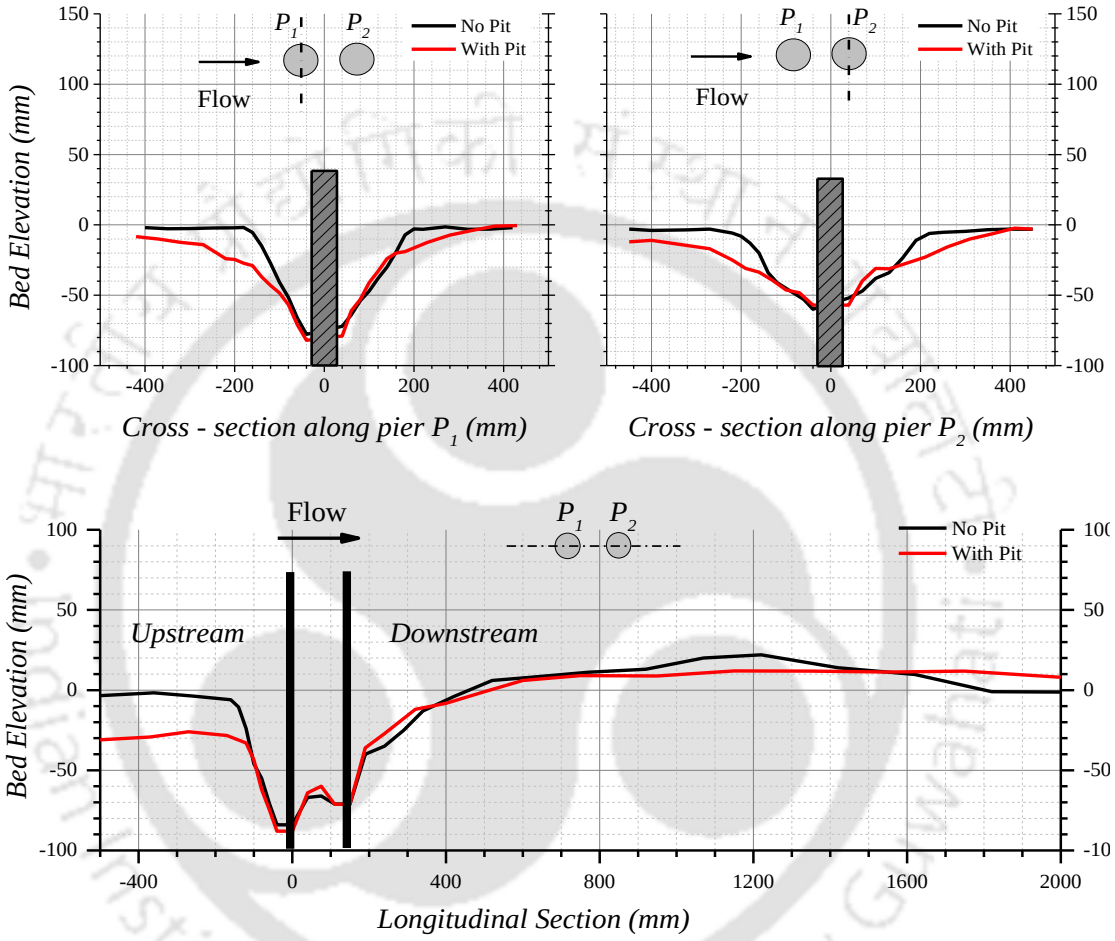

Figure 4.19 Cross-sections along both the piers and longitudinal section along the centerline of the tandem piers.

For no pit case, the flow was initially obstructed by the pier front (P_1), and a down-flow is initiated along P_1 because of stagnation. The interaction of down-flow with the main flow in streamwise direction leads to the formation of horseshoe vortices owing to the reversal of flow occurring at the base of P_1. These vortices dislodge the sediments at the base of P_1, causing local scour. Maximum scour depth in front of the pier P_1 was found to be 79.2 mm. The flow passed around P_1 and immediately encountered the rear pier P_2. As the flow had a high Reynolds number ($Re > 10^4$) and $Pier\ spacing/Pier\ diameter$

ratio as 2.0, wake interference existed between the piers (Zdravkovich, 1987). If this ratio is less than 2, proximity interference exists and the boundary layer does not reattach in between the two piers. Accordingly, in the present case, reattachment of the turbulent boundary layer occurred in the region between both the piers. High velocity flow in the near-bed region of P_2 caused scouring around it. Maximum scour depth in front of the rear pier P_2 was found to be 60 mm. Flow separation occurred behind the rear pier P_2, and a wake zone was created. Very low streamwise velocities were observed in this region. Due to this, the deposition of sediment occurred along the centerline at the downstream side of P_2, which leads to the formation of a dune-like structure. Maximum height of the dune was found to be 22 mm (above the initial bed level), and it was observed at 1200 mm downstream of P_1.

In the second experimental case, a rectangular pit was excavated 1.0 m upstream of the pier front, as stated above. After passing over the pit, flow approaches the piers with higher near-bed velocities, greater bed shear stresses, and increased turbulence intensities compared to no pit case (Section 3.3). Increased turbulence in the flow caused heavy erosion and lowering of channel bed upstream of the piers. Average channel degradation of about 25 mm was observed in the upstream bed. This spatially accelerating flow struck the pier front P_1, and a stronger flow reversal occurred at the base of P_1. This led to the formation of a stronger horseshoe vortex possessing higher turbulent kinetic energy and turbulent stresses than the no pit case (Section 3.3). The stronger horseshoe vortex eroded the lateral sides of the scour hole, and deposition was observed further downstream as compared to the no pit case. The maximum scour depth found in this case (80.7 mm) was slightly higher than the no pit case. This highly turbulent flow at the base of P_1 caused excess erosion of scour hole in the lateral direction and led to greater exposure of both the piers.

4.3.2 Wavelet-based statistical evolution of local scour

Aim of this study was to statistically estimate the spatial evolution of scour depth at various time scales. In order to explore the evolution of local scour in the presence of a mining pit at various time scales, wavelet analysis was employed (Singh et al., 2011).

The statistical speed of spatial evolution of local scour at various time scales was evaluated using cross-correlation analysis of the wavelet coefficients, and the results are presented in the following section.

The temporal progression of local scour was tracked at two fixed locations, i.e., upstream and downstream of the front pier (Location-1 and Location-2, respectively, details of the measurement locations can be found in Section 3.3) using Seatek ultrasonic ranging system. Firstly, the bed elevation time series at the two tracking locations were recorded. It represented the scour depth (amplitude of the signal) against time. We then transformed each of the signals (bed elevation time series in this case) using a wavelet to obtain a matrix of wavelet coefficients. The matrix has rows equal to the number of time scales that we wanted to study and columns equal to the number of data points in the time series. Thus, we obtained the distribution of amplitude for various time scales along the entire length of the signal. Finally, after calculating the wavelet coefficients for both the bed elevation time series, the cross-correlation between the two signals was calculated for all the time scales. For a particular time scale, maximum cross-correlation in the two signals was obtained. This maximum cross-correlation occurred at a time difference in the two signals, and this difference was considered as the lag time. Statistically, this lag represents the time required for the scour depth at that particular time scale to evolve from pier upstream to the pier downstream. The distance between the two measurement locations was divided with this time lag to obtain the speed of the spatial evolution of scour depth at that particular time scale. Same procedure was repeated for various time scales. Note that the spatial evolution estimated by this method is based on the statistical dependence of the cross-correlation between the wavelet coefficients.

For this analysis, the bed elevations at Locations-2 and 3 (upstream and downstream of P_1), recorded at a temporal resolution of 0.5 s are utilized. The bed elevations of local scour at 2 h, 4 h, and 6 h are plotted in Figure 4.20 for both cases.

Careful observation shows that fluctuations in the scour depth are greater in the case of the mining pit. The reason for this lies in the flow alterations in the horseshoe vortex zone, in the case of a pit. Vortex formation at the base of the pier is highly unsteady. For

every event of vortex formation, whose primary circulation lies in the *X-Z* plane, sediments are dislodged from the bed and go in suspension for a fraction of time. Depending upon the specific weight of individual sediment particles, some of them are swept downstream while some again settle down in the scour hole. Movement/settling of the particles depends upon the balance of drag and lift forces acting on the sediment particles and their specific weight. Because of this unsteady movement of bed particles within the scour hole, there are fluctuations in the recordings bed elevations (Figure 4.20). Higher fluctuations in case of a mining pit is an implicit indication of a higher number of unsteady vortex events, compared to no pit case.

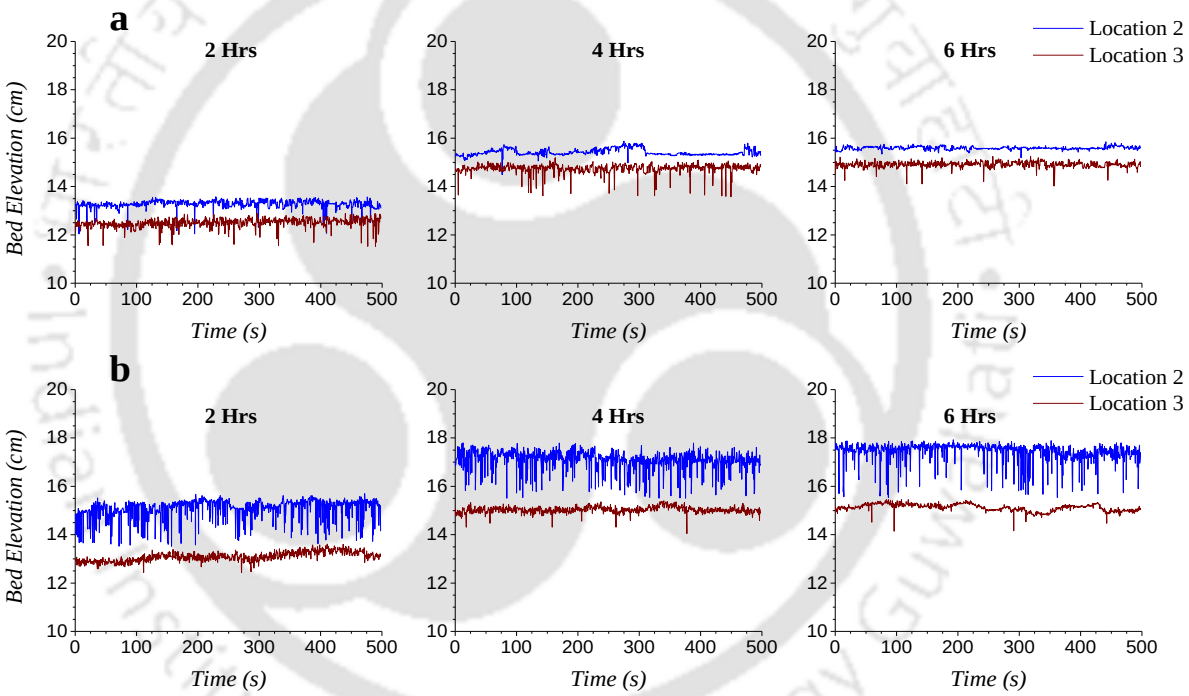

Figure 4.20 Bed elevation time series of scour depth (upstream and downstream) of P_1 for (a) No pit and (b) With pit case.

Spatial evolution of scour at various time scales can be resourceful in understanding the effect of a mining pit local scour around bridge piers. Local scour at the base of the piers is a time-dependent non-linear phenomenon. Therefore wavelets were used to transform the bed elevation time series of local scour into multi-scale coefficients. A major advantage of using wavelets is that it provides a matrix of coefficients that are identified

by their scale and translation. Hence the distribution of amplitude for a signal can be understood at various scales as well as translations as opposed to fast Fourier transform wherein amplitude distribution only in the frequency domain is obtained, and the information across the time domain is lost.

The bed elevation time series at both these locations were treated a discrete signal over the time domain. The bed elevation series at upstream and downstream of P_1 were referred to as two signals $f_1(t)$ and $f_2(t)$ respectively. Continuous wavelet transform of a signal $f(t)$ is given by:

$$W_{f(t)}(a,b) = \int_{-\infty}^{+\infty} f(t)\,\psi_{a,b}(t)dt \tag{4.1}$$

where $\psi_{a,b}$ is a wavelet function which comes from a mother wavelet $\psi(t)$ post translation and scaling, given by:

$$\psi_{a,b}(t) = \frac{1}{\sqrt{a}}\psi\left(\frac{t-b}{a}\right); \quad a > 0; \quad b \in R. \tag{4.2}$$

Here a is the scale and b is the translation, i.e., location along with the signal. $1/\sqrt{a}$ is a multiplying factor to normalize the variance (Mallat, 1999). A necessary condition for wavelet transform is that the area under the wavelet function should be zero i.e. $\int_{-\infty}^{+\infty}\psi(t)dt = 0$. A Mexican hat wavelet $\phi(t)$ was used in this study which has a number of vanishing moments as 2. Hence, this wavelet transform acts as a second-order local differencing filter and eliminates the linear trend in the signal along with the translation. More details about wavelets can be found in previous literature (Kumar & Foufoula-Georgiou, 1997).

$$\phi(t) = \frac{2}{\sqrt{3}}\pi^{-1/4}(1-t^2)e^{-t^2/2} \tag{4.3}$$

Thus, the wavelet coefficients for both the bed elevation time series along various scales and translation are obtained by the following expression:

$$WC(a,b) = \frac{1}{\sqrt{a}} \int_{-\infty}^{+\infty} f(t)\phi\left(\frac{t-b}{a}\right) dt \tag{4.4}$$

The wavelet cross-correlation analysis can be useful to assess the statistical dependence between two signals separated by a spatial distance S. After calculating the wavelet coefficients from the above expression, the cross-correlation between two signals was obtained by:

$$WCC_{f_1(t)f_2(t)}(a,\Delta t) = \int_{-\infty}^{+\infty} WC_{f1}(a,b)WC_{f2}(a,b+\Delta t)\, db \tag{4.5}$$

Here, $WC_{f1}(a,b)$ and $WC_{f2}(a,b+\Delta t)$ are the wavelet coefficients of bed elevation series $f_1(t)$ and $f_2(t)$ respectively at scale a and two consecutive locations b and $b+\Delta t$ along with the signals. For a particular scale a, the lag Δt_{max} which resulted in maximum cross-correlation between the wavelet coefficients of two signals $f_1(t)$ and $f_2(t)$ was calculated. The speed of spatial evolution of the scour at scale a can be calculated as $V_c(a,\Delta t) = S/\Delta t_{max}$.

For this study, the spatial evolution speed of the local scour at various time scales at 2 h, 4 h, and 6 h from the start of both experiments was calculated. The spatial evolution speed of local scour at various time scales is provided in Table 4.3, and plots are presented in Figure 4.21.

Scour evolution is a dynamic process, and spatial evolution (between upstream and downstream of the pier) with the time scale is non-linear [Figure 4.21(b)]. The spatial evolution at lower time scales is faster, and it becomes nearly constant at about 25 s for no pit case and 30 s in the case of the mining pit. Figure 12(b) shows that the spatial evolution of local scour at smaller time scales (< 20 s) is faster in the case of a mining pit. Especially, at the early stage of the run (2 hours), the average speed of spatial scour evolution in the case of a mining pit is found to be maximum (2.545 m/h) in comparison to no pit case (2.157 m/h). This indicates that the spatial evolution of scour at smaller time scales is faster in the case of a mining pit. The spatial scour evolution is about 15 % faster because of the excavation of a mining pit (Table 4.3).

Table 4.3 Spatial evolution speed of local scour (between upstream and downstream of the pier) for different time scales.

Time scale (s)	**Spatial evolution speed** (m/h)					
	2 hours		**4 hours**		**6 hours**	
	No Pit	**With Pit**	**No Pit**	**With Pit**	**No Pit**	**With Pit**
1	6.641	5.405	6.084	5.758	6.696	4.300
2	5.198	5.029	4.886	5.228	5.098	3.929
3	4.455	5.129	4.728	3.777	4.119	3.903
4	3.740	4.953	4.589	3.567	3.016	3.423
5	3.307	4.690	4.611	3.516	2.938	3.380
6	3.471	4.122	4.331	3.070	2.582	3.439
7	3.354	3.412	3.727	2.850	2.428	3.386
8	3.194	3.060	3.182	2.841	2.435	3.714
9	2.993	2.760	2.866	3.050	2.457	3.541
10	2.981	2.575	2.732	3.007	2.289	2.966
11	2.896	2.462	2.471	3.015	2.204	2.492
12	2.619	2.411	2.330	3.020	2.153	2.226
13	2.391	2.403	2.269	2.759	2.005	2.067
14	2.217	2.434	2.270	2.614	1.874	1.997
15	2.075	2.494	2.313	2.544	1.759	1.957
16	1.953	2.567	2.131	2.517	1.659	1.929
17	1.865	2.663	1.901	2.550	1.577	1.916
18	1.799	2.755	1.716	2.412	1.508	1.894
19	1.733	2.807	1.565	2.279	1.448	1.856
20	1.681	2.704	1.445	2.185	1.395	1.811
21	1.630	2.541	1.350	2.107	1.346	1.762
22	1.589	2.357	1.277	2.056	1.304	1.715
23	1.546	2.185	1.219	2.015	1.263	1.673
24	1.504	2.040	1.175	1.974	1.223	1.628
25	1.460	1.922	1.143	1.927	1.185	1.587
26	1.413	1.827	1.119	1.871	1.148	1.546
27	1.376	1.755	1.102	1.819	1.114	1.507
28	1.331	1.698	1.091	1.756	1.081	1.476
29	1.293	1.652	1.085	1.688	1.051	1.449
30	1.259	1.618	1.084	1.620	1.025	1.426
31	1.226	1.590	1.084	1.552	1.000	1.407
32	1.195	1.567	1.087	1.490	0.978	1.391
33	1.173	1.553	1.092	1.435	0.960	1.382
34	1.153	1.543	1.098	1.388	0.944	1.376
35	1.135	1.533	1.103	1.347	0.930	1.372
36	1.118	1.525	1.108	1.309	0.917	1.368

37	1.103	1.520	1.111	1.276	0.907	1.364
38	1.086	1.517	1.111	1.246	0.900	1.362
39	1.074	1.510	1.112	1.220	0.891	1.357
40	1.064	1.507	1.109	1.193	0.885	1.357
Average speed of spatial evolution	2.157	2.545	2.120	2.371	1.817	2.141

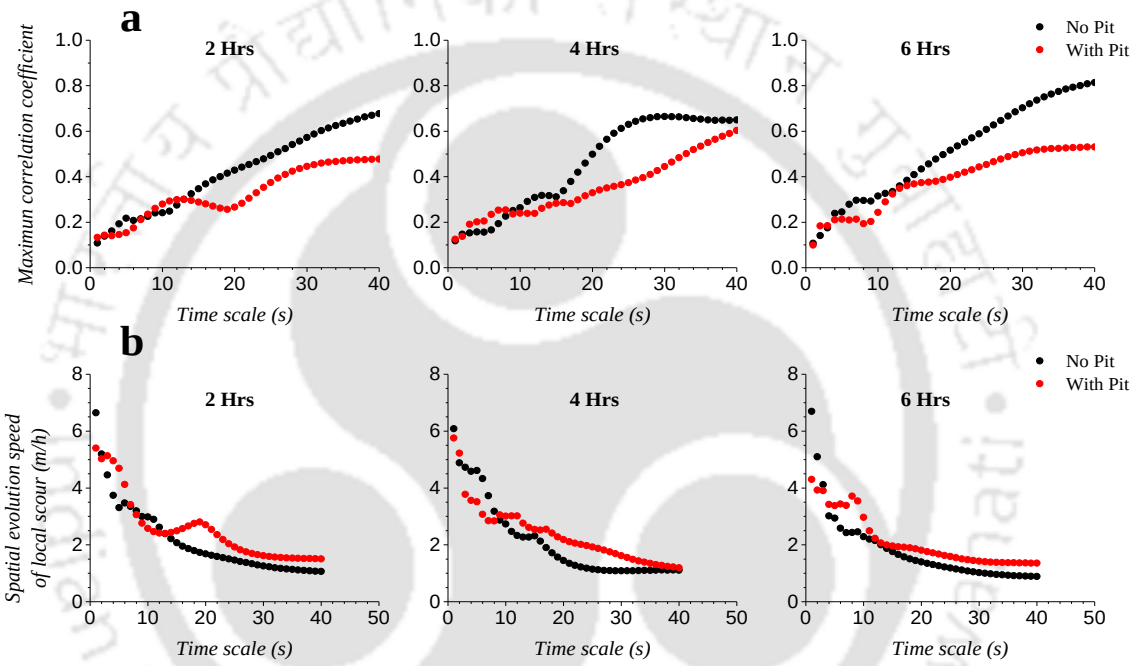

Figure 4.21 (a) Maximum correlation coefficients between the wavelet-coefficients at upstream and downstream of the pier front and (b) Spatial evolution speed of local scour at various time scales for both cases.

4.3.3 Summary

The mining pit caused excessive streambed scour around the tandem piers and widening of scour hole on the lateral sides. The spatial evolution of local scour was remarkably faster in the presence of a pit. Excavation of pit in the channel caused higher exposure of the piers due to lateral erosion of the scour hole. Also, the dune crest behind the rear pier was shifted further downstream because of pit excavation.

Chapter **5**

Conclusions and Recommendations

With the ever-increasing demand for sand, in-stream mining has grown extensively in the last few decades. The mining industry is highly unregulated, and unrestricted dredging of sand from the riverbed is a common sight, especially in the Asian and African countries. In-stream mining causes incision of the riverbed, which can extend in kilometers; therefore, the safety of bridges in the proximity is a major concern. Mining pits can drastically alter the flow characteristics as well as local scouring around bridge piers on the downstream side, which may lead to the undermining and failure of such bridge piers.

In order to understand the alterations in the flow-field around bridge piers and mechanism of streambed deterioration due to mining activities, gravity-flow experiments were conducted in a laboratory flume. Effects of an upstream mining pit on the turbulence field around a circular and oblong bridge pier were evaluated. The morphological response of the streambed around a circular pier under the influence of a mining pit was also studied. The variation of streambed instabilities with the shape of the mining pit as well as the distance between the pit and the circular pier, was also explored. Major conclusions of the study are outlined below.

5.1 Effect of a Mining Pit on the Structure of Turbulence Around Bridge Piers

- Flow separation occurs on account of a sudden positive pressure gradient and reattachment of the flow at the downstream edge of the pit, when flow passes over a mining pit. Flow reversal zone was detected inside the pit region.
- Flow approaches the pier with higher spatial acceleration and streambed upstream of the pier subjected to higher near-bed mean streamwise velocities in the presence of a pit.
- Pit excavation acts as a source of turbulence to the downstream flow causing a significant increase in the turbulent stresses in the pit region and its downstream.

- Excess momentum transport along with the flow depth inside the pit as well as in its downstream zone. as indicated by the increase in the average turbulent stresses around circular pier, oblong pier as well as two circular piers in tandem.
- The streambed in the downstream region of the pit subjected to a higher bed shear stress in case of a circular pier, oblong pier, as well as two circular piers in tandem.
- Formation of a stronger horseshoe vortex with greater eddy sizes at the base of the pier front, on account of the interaction of flow passing over a pit with the pier. Similar observation of stronger horseshoe vortex at the base of the circular pier, oblong pier, as well as two circular piers in tandem.
- Increase in the turbulent stresses in this horseshoe vortex zone and greater dominance of sweep and ejection events in this zone is compared to without pit case.
- Greater flux of the streamwise turbulent kinetic energy traveling in the streamwise direction in the scour hole zone due to pit excavation. Further, a stronger flux of the vertical turbulent kinetic energy rushing in a vertically downward direction inside the scour hole.
- The amplification of the instantaneous bed shear beneath the turbulent horseshoe vortex (THV) zone almost twice as compared to no-pit case, indicating the influence of pit excavation on the dynamics of THV.
- Remarkable increase in the lateral turbulent shear stresses behind the pier after passing over a pit. The interaction of the flow with the pier after passing over a pit significantly increases the length scale of the largest eddies, which are being shed in the flow reversal zone behind the pier.
- Rise the strength and frequency of the shedding vortices behind the pier due to the pit excavation upstream of the pier indicated by Strouhal number, which may alter the transport characteristics at the pier downstream.
- The mean flow zones formed around the cylinder govern the scaling characteristics of higher-order moments of streamwise velocity fluctuations around the cylinder. At the cylinder front, turbulence production increases from the channel bed and reaches its peak at a distance where the flow transitions from

the recirculation zone (negative mean streamwise velocities) to the down-flow zone (positive mean velocities). Beyond this distance, the variance of streamwise velocity fluctuations follows log law. At the rear side, turbulence production occupies greater flow depth from the channel bed (till $z/h \sim 0.4$) compared to the front side (till $z/h \sim 0.11$), and the peak reaches where the boundary layer separates from the cylinder and wake zone occurs. Beyond this distance, log scaling of variance is observed within the wake zone. Scaling of higher-order moments, namely 2p = 4 and 2p = 6, is similar to the variance. The turbulence field generated around the cylinder due to fluid-solid interaction also follows logarithmic scaling. Channel dredging increases the peak of $\langle (u'^{+})^2 \rangle$ about 5% at the cylinder front and about 15% at the rear side.

5.2 Effect of a Mining Pit on the Morphology around Bridge Piers

- Morphological instabilities around the pier present downstream of a mining pit.
- Excessive erosion and exposure of the pier as well as bed lowering in the approach zone of the pier, due to pit excavation.
- The streambed instability around the pier was a function of the Reynolds number (Re) as well as the distance between the pier and the mining zone (L/d).
- Dredging of a pit very close to the pier (L/d = 13.33) critical as the pier exposure factor can reach as high as 1.5, and the normalized depth of bed lowering in the approach zone can reach 0.4. For $L/d \geq 26.66$, pier exposure only significant for high Reynolds numbers (Re > 45000).
- Filling of the scour hole at the frontal side of the pier present downstream of a mining pit. Therefore, the maximum scour depths measured at the pier base slightly lowered in the presence of a mining pit.
- Similar morphological response of the streambed around a circular pier was in the case of rectangular and trapezoidal pits having the same widths. However, the severity of streambed instabilities slightly decreased in the case of an irregular pit, which had a lesser width. Thus, pier exposure and upstream incision depth can be affected by the width of mining pits.

- The spatial evolution of local scour remarkably faster in the presence of a pit.
- In-stream mining activities, especially in the proximity of a bridge pier, have the potential to erode the streambed around the pier and may contribute to its failure.

5.3 Recommendations Regarding Mining Activities in Proximity of Bridges

- In-stream mining in the proximity of the pier can lead to exposure of bridge piers, especially during flood conditions. Therefore In-stream mining activities should not be allowed inside a distance of at least 40 times the diameter of the pier, from the bridges.
- The safe distance between bridge piers and mining sites should be worked out on a case to case basis, as directed by the Supreme Court of India, since the streambed instabilities depend upon the distance between the pit and bridge pier, the width of the mining zone, etc.
- As the effect of mining is not localized in the local scour zone and has a global erosive effect around the piers, pier modifications shall not be extremely effective in mitigating the erosion and exposure of the piers. Therefore a holistic approach should be adopted for scour mitigation of mining-affected bridges such as local armoring of the pier base supplemented with and end sill across the streambed width.

5.4 Recommendations for Future Research

- Based on the results of the present study, future research can be conducted on the morphodynamic response of a complex bridge pier with a pile cap and a group of piles along with the pier.
- Further research is required to device effective strategies for the mitigation of streambed deterioration around bridge piers caused due to mining activities.
- Sediment feeding from the upstream may have a significant effect on the hydro-morphology around bridge piers downstream of the mining pit. This aspect may be explored further for more realistic results.

References

Abe, H., Kawamura, H., & Choi, H. (2004). Very large-scale structures and their effects on the wall shear-stress fluctuations in a turbulent channel flow up to Re_τ = 640. *Journal of Fluids Engineering*, *126*(5), 835–843.

Ahmed, F., & Rajaratnam, N. (1998). Flow around bridge piers. *Journal of Hydraulic Engineering*, *124*(3), 288–300.

Ataie-Ashtiani, B., & Aslani-Kordkandi, A. (2013). Flow field around single and tandem piers. *Flow, Turbulence and Combustion*, *90*(3), 471–490.

Ataie-Ashtiani, B., & Beheshti, A. A. (2006). Experimental investigation of clear-water local scour at pile groups. *Journal of Hydraulic Engineering*, *132*(10), 1100–1104.

Avila, C. (2016). 25 years of fixing bridges on gravel mined rivers in California. In *8rd International Conference on Scour and Erosion (ICSE-8).*September 12-15, Oxford, UK.

Avila, C. (2006). Bridges in Critical Condition-San Benito River Gravel Mining and the Hospital Road Bridge. In *3rd International Conference on Scour and Erosion (ICSE-3).* November 1-3, Amsterdam, The Netherlands (pp. 23–30).

Azar, M. G., Davoudi, M. H., & Tokaldani, E. A. (2011). Time dependent variation of river bed profile due to mining pit. In *5th Symposium on Advances in Science and Technology*, May 12 - 17, Mashhad, Iran (pp. 1–8).

Barman, B., Kumar, B., & Sarma, A. K. (2017). Experimental Study on Mining Pit Migration. In *Development of Water Resources in India* (pp. 305–309). Springer.

Barman, B., Kumar, B., & Sarma, A. K. (2018). Turbulent flow structures and geomorphic characteristics of a mining affected alluvial channel. *Earth Surface Processes and Landforms*, *43*(9), 1811–1824.

Bathurst, J. C. (1985). Flow resistance estimation in mountain rivers. *Journal of Hydraulic Engineering*, *111*(4), 625–643.

Bendixen, M., Best, J., Hackney, C., & Iversen, L. L. (2019). Time is running out for sand. *Nature*, *57*, 29–31.

Best, J. I. M. (1992). On the entrainment of sediment and initiation of bed defects: insights from recent developments within turbulent boundary layer research. *Sedimentology*, *39*(5), 797–811.

Brestolani, F., Solari, L., Rinaldi, M., & Lollino, G. (2015). On the morphological impacts of gravel mining: the case of the Orco River. In *Engineering Geology for Society and Territory-Volume 3* (pp. 319–322). Springer.

Cao, Z., & Pender, G. (2004). Numerical modelling of alluvial rivers subject to interactive sediment mining and feeding. *Advances in Water Resources*, *27*(5), 533–546.

Chen, D., & Liu, M. (2009). One-and two-dimensional modeling of deep gravel mining in the Rio Salado. In *World Environmental and Water Resources Congress 2009.* May 17-21, Kansas City, Missouri, United States (pp. 1–9).

Chen, D., Acharya, K., & Stone, M. (2010). Sensitivity analysis of nonequilibrium adaptation parameters for modeling mining-pit migration. *Journal of Hydraulic Engineering*, *136*(10), 806–811.

Chen, S., Wang, J., Xu, H., Di, J., & Li, Z. (2018). Effect of Sand Mining on Bridge Capacity and Safety under the Bridge. *Journal of Highway and Transportation Research and Development (English Edition)*, *12*(2), 51–58.

Chiew, Y.-M., & Melville, B. W. (1987). Local scour around bridge piers. *Journal of Hydraulic Research*, *25*(1), 15–26.

Chiew, Y. M. (1984). *Local scour at bridge piers*. Doctoral dissertation, Auckland University.

Clark, C. (2018). *Measuring the Vortex-Shedding Frequency Behind Staggered Cylinders in Cross-Flow*. Masters thesis, Santa Clara University.

Collins, B., & Dunne, T. (1990). *Fluvial geomorphology and river-gravel mining: a guide for planners, case studies included*. California Department of Conservation, Division of Mines and Geology. USA.

Collins, B. D., & Dunne, T. (1989). Gravel transport, gravel harvesting, and channel-bed degradation in rivers draining the southern Olympic Mountains, Washington, USA. *Environmental Geology and Water Sciences*, *13*(3), 213–224.

Cordone, A. J., & Kelley, D. W. (1961). *The influences of inorganic sediment on the aquatic life of streams*. California Department of Fish and Game, USA.

Crunkilton, R. L. (1982). An overview of gravel mining in Missouri and fish and wildlife implications [Water pollution control, land use regulation, environmental impact]. *University of Minnesota, Agricultural Experiment Station*.

Dargahi, B. (1989). The turbulent flow field around a circular cylinder. *Experiments in Fluids*, *8*(1–2), 1–12.

Das, S., Das, R., & Mazumdar, A. (2013). Circulation characteristics of horseshoe vortex in scour region around circular piers. *Water Science and Engineering*, *6*(1), 59–77.

De Silva, C. M., Marusic, I., Woodcock, J. D., & Meneveau, C. (2015). Scaling of second- and higher-order structure functions in turbulent boundary layers. *Journal of Fluid Mechanics*, *769*, 654–686.

Deshpande, V., & Kumar, B. (2016). Turbulent flow structures in alluvial channels with curved cross-sections under conditions of downward seepage. *Earth Surface Processes and Landforms*, *41*(8), 1073–1087.

Dey, S. (1995). Three-dimensional vortex flow field around a circular cylinder in a quasi-equilibrium scour hole. *Sadhana*, *20*(6), 871–885.

Dey, S., & Raikar, R. V. (2007). Characteristics of horseshoe vortex in developing scour holes at piers. *Journal of Hydraulic Engineering*, *133*(4), 399–413.

Dey, S., Das, R., Gaudio, R., & Bose, S. K. (2012). *Turbulence in mobile-bed streams*. *Acta Geophysica, 60(6)*, 1547-1588.

Ducrocq, T., Cassan, L., Chorda, J., & Roux, H. (2017). Flow and drag force around a free surface piercing cylinder for environmental applications. *Environmental Fluid Mechanics*, *17*(4), 629–645.

Erskine, W. D. (1990). Environmental impacts of sand and gravel extraction on river systems. *The Brisbane River: A Source Book for the Future, Australian Littoral Society, Moorooka*, 295–302.

Gill, M. A. (1994). Hydrodynamics of mining pits in erodible bed under steady flow. *Journal of Hydraulic Engineering*, *120*(11), 1337–1348.

Goring, D. G., & Nikora, V. I. (2002). Despiking acoustic Doppler velocimeter data. *Journal of Hydraulic Engineering*, *128*(1), 117–126.

Graf, W. H., & Istiarto, I. (2002). Flow pattern in the scour hole around a cylinder. *Journal of Hydraulic Research*, *40*(1), 13–20.

Graf, W. H., & Yulistiyanto, B. (1998). Experiments on flow around a cylinder; The velocity and vorticity fields. *Journal of Hydraulic Research*, *36*(4), 637–653.

Guan, D., Agarwal, P., & Chiew, Y. M. (2018). Quadrant analysis of turbulence in a rectangular cavity with large aspect ratios. *Journal of Hydraulic Engineering*, *144*(7), 1–9.

Guan, D., Chiew, Y.-M., Wei, M., & Hsieh, S.-C. (2019). Characterization of horseshoe vortex in a developing scour hole at a cylindrical bridge pier. *International Journal of Sediment Research*, *34*(2), 118–124.

Haghnazar, H., & Saneie, M. (2019). Impacts of pit distance and location on river sand mining management. *Modeling Earth Systems and Environment*, *5*(4), 1463–1472.

Hamilton, J. D. (1961). The effect of sand-pit washings on a stream fauna: With 2 tables in the text. *Internationale Vereinigung Für Theoretische Und Angewandte Limnologie: Verhandlungen*, *14*(1), 435–439.

Hultmark, M., Vallikivi, M., Bailey, S. C. C., & Smits, A. J. (2012). Turbulent pipe flow at extreme reynolds numbers. *Physical Review Letters*, *108*(9), 1–5.

Ikhsan, J., Fujita, M., & Takebayashi, H. (2009). Sustainable sand mining management in Merapi Area using groundsills. *Annuals of Diasaster Prevention Research Institute, Kyoto University, 52(B)*, 647-657.

Izadinia, E., Heidarpour, M., & Schleiss, A. J. (2013). Investigation of turbulence flow and sediment entrainment around a bridge pier. *Stochastic Environmental Research and Risk Assessment*, *27*(6), 1303–1314.

Jang, C.-L., Shimizu, Y., & Lee, G. H. (2015). Numerical simulation of the fluvial processes in the channels by sediment mining. *KSCE Journal of Civil Engineering*, *19*(3), 771–778.

JM Weeks, I Sims, C Lawson, D. H. (2003). River Mining: assessment of the ecological effects of river mining in the Rio Minho and Yallahs rivers, Jamaica. *British Geological Survey Commissioned Report*.

Kanehl, P. D., & Lyons, J. D. (1992). *Impacts of in-stream sand and gravel mining on stream habitat and fish communities, including a survey on the Big Rib River, Marathon County, Wisconsin* (Vol. 155). Wisconsin Department of Natural Resources, Bureau of Research.

Keshavarzi, A., Melville, B., & Ball, J. (2014). Three-dimensional analysis of coherent turbulent flow structure around a single circular bridge pier. *Environmental Fluid Mechanics*, *14*(4), 821–847.

Kim, C. (2005). Impact analysis of river aggregate mining on river environment. *KSCE Journal of Civil Engineering*, *9*(1), 45–48.

Kirkil, G., Constantinescu, G., & Ettema, R. (2005). The horseshoe vortex system around a circular bridge pier on equilibrium scoured bed. In *Impacts of Global Climate Change* (pp. 1–12).

Kirkil, G., Constantinescu, S. G., & Ettema, R. (2008). Coherent structures in the flow field around a circular cylinder with scour hole. *Journal of Hydraulic Engineering*, *134*(5), 572–587.

Kondolf, G. M., & Swanson, M. L. (1993). Channel adjustments to reservoir construction and gravel extraction along Stony Creek, California. *Environmental Geology*, *21*(4), 256–269.

Kondolf, G Mathias. (1994). Geomorphic and environmental effects of instream gravel mining. *Landscape and Urban Planning*, *28*(2–3), 225–243.

Kondolf, G Mathias. (1997). PROFILE: hungry water: effects of dams and gravel mining on river channels. *Environmental Management*, *21*(4), 533–551.

Kothyari, U. C., & Kumar, A. (2012). Temporal variation of scour around circular compound piers. *Journal of Hydraulic Engineering*, *138*(11), 945–957.

Krogstad, P. Å., & Antonia, R. A. (1999). Surface roughness effects in turbulent boundary layers. *Experiments in Fluids*, *27*(5), 450–460.

Kumar, A., & Kothyari, U. C. (2012). Three-dimensional flow characteristics within the scour hole around circular uniform and compound piers. *Journal of Hydraulic Engineering*, *138*(5), 420–429.

Kumar, P., & Foufoula-Georgiou, E. (1997). Wavelet analysis for geophysical applications. *Reviews of Geophysics*, *35*(4), 385–412.

Kumar, V., Raju, K. G. R., & Vittal, N. (1999). Reduction of local scour around bridge piers using slots and collars. *Journal of Hydraulic Engineering*, *125*(12), 1302–1305.

Langer, W. H. (2003). *A general overview of the technology of in-stream mining of sand and gravel resources, associated potential environmental impacts, and methods to control potential impacts*. US Department of the Interior, US Geological Survey.

Lee, H.-Y., Fu, D.-T., & Song, M.-H. (1993). Migration of rectangular mining pit composed of uniform sediments. *Journal of Hydraulic Engineering*, *119*(1), 64–80.

lu, S. S., & Willmarth, W. W. (1973). *Measurements of the structure of the Reynolds stress in a turbulent boundary layer*. *Journal of Fluid Mechanics*, 60(3), 481-511.

Mallat, S. (1999). *A wavelet tour of signal processing*. Elsevier.

Marcus, L. (1992). Status report: Russian River resource enhancement plan. *California Coastal Conservancy, Oakland, California*.

Marsh, N. A., Western, A. W., & Grayson, R. B. (2004). Comparison of methods for predicting incipient motion for sand beds. *Journal of Hydraulic Engineering*, *130*(7), 616–621.

Martín-Vide, J. P., Ferrer-Boix, C., & Ollero, A. (2010). Incision due to gravel mining: modeling a case study from the Gállego River, Spain. *Geomorphology*, *117*(3–4), 261–271.

Maurer, D., Keck, R. T., Tinsman, J. C., & Leathem, W. A. (1981). Vertical migration and mortality of benthos in dredged material—Part I: Mollusca. *Marine Environmental Research*, *4*(4), 299–319.

McKenzie, M., Mathers, K. L., Wood, P. J., England, J., Foster, I., Lawler, D., & Wilkes, M. (2020). Potential physical effects of suspended fine sediment on lotic macroinvertebrates. *Hydrobiologia*, *847*(3), 697–711.

Mckeon, B. J., Li, J., Jiang, W., Morrison, J. F., & Smits, A. J. (2004). Further observations on the mean velocity distribution in fully developed pipe flow. *Journal of Fluid Mechanics*, *501*, 135–147.

Melville, B. W. (1984). Live-bed scour at bridge piers. *Journal of Hydraulic Engineering*, *110*(9), 1234–1247.

Melville, B. W., & Coleman, S. E. (2000). *Bridge scour*. Water Resources Publication.

Melville, B. W., & Raudkivi, A. J. (1977). Flow characteristics in local scour at bridge piers. *Journal of Hydraulic Research*, *15*(4), 373–380.

Meneveau, C., & Marusic, I. (2013). Generalized logarithmic law for high-order moments in turbulent boundary layers. *Journal of Fluid Mechanics*, *719*, 1–11.

Ministry of Environment Forest and Climate Change. (2016). *Sustainable Sand Mining Management Guidelines 2016*.

Monin, A. S., & Yaglom, A. M. (2013). *Statistical fluid mechanics, volume II: mechanics of turbulence*. Courier Corporation.

Muzzammil, M., & Gangadhariah, T. (2003). The mean characteristics of horseshoe vortex at a cylindrical pier. *Journal of Hydraulic Research*, *41*(3), 285–297.

Naik, Y. (2017, February 7). Sand mining threatens more Mahad bridges. *The Times of India*. Retrieved from https://mumbaimirror.indiatimes.com/mumbai/other/sand-mining-threatens-more-mahad-bridges/articleshow/57011554.cms

Nakagawa, H., & Nezu, I. (1977). Prediction of the contributions to the Reynolds stress from bursting events in open-channel flows. *Journal of Fluid Mechanics*, *80*(1), 99–128.

Neyshabouri, S., Farhadzadeh, A., & Amini, A. (2002). Experimental and field study on mining-pit migration. *International Journal of Sediment Research*, *17*(4), 323–331.

Nezu, I., & Nakagawa, H. (1993). Turbulence in open-channel flows, IAHR monograph series. *AA Balkema, Rotterdam*, 1–281.

Nikora, V. I., & Smart, G. M. (1997). Turbulence characteristics of New Zealand gravel-bed rivers. *Journal of Hydraulic Engineering*, *123*(9), 764–773.

Nilipour, N., De Cesare, G., & Boillat, J.-L. (2004). Application of UVP transducers to measure bed geometry and velocity profiles in a hydraulic scale model with gravel pit. In *4th International Symposium on Ultrasonic Doppler Method for Fluid Mechanics and Fluid Engineering*,September 6-8, Hokkaido University, Sapporo, Japan (pp. 41–46).

Owens, P. N., Batalla, R. J., Collins, A. J., Gomez, B., Hicks, D. M., Horowitz, A. J. (2005). Fine-grained sediment in river systems: environmental significance and management issues. *River Research and Applications*, *21*(7), 693–717.

Peng, J., Chen, D., & Yuill, B. T. (2019). Modeling Evolution of a Large Mining Pit in the Lower Mississippi River. In *World Environmental and Water Resources Congress 2019: Hydraulics, Waterways, and Water Distribution Systems Analysis* May 19-23, Pittsburgh, Pennsylvania, USA (pp. 287–295).

Pope, S. B. (2000). *Turbulent Flows*. Cambridge University Press.

Qadar, A. (1981). The Vortex Scour Mechanism at Bridge Piers. *Proceedings of the Institution of Civil Engineers*, *71*(3), 739–757.

Qi, M., & Kuai, Y. (2017). Pier scour under influence of headcut erosion of sand pit. *Shuili Xuebao/Journal of Hydraulic Engineering*, *48*(7), 791–798.

Qi, M., Yang, Y., & Kuai, Y. (2017). Study on Effect and Mechanism of Pier Scour Mitigation by Sill in Riverbed with Sand Excavation. *Zhongguo Tiedao Kexue/China Railway Science*, *38*(4), 33–39.

Raupach, M. R. (1981). Conditional statistics of Reynolds stress in rough-wall and smooth-wall turbulent boundary layers. *Journal of Fluid Mechanics*, *108*, 363–382.

Rinaldi, M., Wyżga, B., & Surian, N. (2005). Sediment mining in alluvial channels: physical effects and management perspectives. *River Research and Applications*, *21*(7), 805–828.

Rivier, B., & Seguier, J. (1985). Physical and biological effects of gravel extraction in river beds. In *Symposium on Habitat Modification and Freshwater Fisheries, ,* May 23rd , Aarhus, Denmark.

Rovira, A., Batalla, R. J., & Sala, M. (2005). Response of a river sediment budget after historical gravel mining (the lower Tordera, NE Spain). *River Research and Applications*, *21*(7), 829–847.

Samadi, A., & Azizian, A. (2015). Two Dimensional Simulation of the Evolution of a Mining Pit using CCHE2D. In *GIAN Conference on Water: Source of Life,* October 17-18,Qazvin, Iran.

Sear, D. A., & Archer, D. R. (1998). The effects of gravel extraction on the stability of gravel-bed rivers: A case study from the Wooler Water, Northumberland, UK. In *Gravel Bed Rivers in the Environment,* Water Research Council, Colorado, USA, (pp. 415-432).

Sharma, A., & Kumar, B. (2018). High-Order Velocity Moments of Turbulent Boundary Layers in Seepage Affected Alluvial Channel. *Journal of Fluids Engineering, Transactions of the ASME*, *140*(8), 1–8.

Shields Jr, F. D., & Nunnally, N. R. (1984). Environmental aspects of clearing and snagging. *Journal of Environmental Engineering*, *110*(1), 152–165.

Shourian, M., & Neshabouri, S. A. A. (2004). Effect Of The Initial Location On Sand And Gravel Mining Pit Migration. In *2nd International Conference on Scour and*

Erosion (ICSE-2). November 14-17, Singapore.

Singh, A., Lanzoni, S., Wilcock, P. R., & Foufoula-Georgiou, E. (2011). Multiscale statistical characterization of migrating bed forms in gravel and sand bed rivers. *Water Resources Research*, *47(*12*)*. W12526.

Soulsby, R. L., & Dyer, K. R. (1981). The form of the near-bed velocity profile in a tidally accelerating flow. *Journal of Geophysical Research: Oceans*, *86(*9*)*, 8067–8074.

Sousa, J. J., Bastos, L., Monserrat, O., & Perski, Z. (2013). Multi-temporal SAR interferometry reveals acceleration of bridge sinking before collapse. *Natural Hazards & Earth System Sciences*, *13*(3), 659-667.

Sreebha, S., & Padmalal, D. (2011). Environmental impact assessment of sand mining from the small catchment rivers in the southwestern coast of India: a case study. *Environmental Management*, *47*(1), 130–140.

Stapleton, K. R., & Huntley, D. A. (1995). Seabed stress determinations using the inertial dissipation method and the turbulent kinetic energy method. *Earth Surface Processes and Landforms*, *20*(9), 807–815.

Stern, E. M. (1978). *Effects of Turbidity and suspended materials in aquatic environments* (Technical Report D-7821).Chief of Engineers U.S. Army.

Surian, N., & Rinaldi, M. (2003). Morphological response to river engineering and management in alluvial channels in Italy. *Geomorphology*, *50*(4), 307–326.

Tachie, M. F., Bergstrom, D. J., & Balachandar, R. (2000). Rough wall turbulent boundary layers in shallow open channel flow. *J. Fluids Eng.*, *122*(3), 533–541.

Tachie, Mark F., Bergstrom, D. J., & Balachandar, R. (2004). Roughness effects on the mixing properties in open channel turbulent boundary layers. *Journal of Fluids Engineering, Transactions of the ASME*, *126*(6), 1025–1032.

Taylor, G. I. (1935). Statistical theory of turbulence. IV. Diffusion in a turbulent air stream. *Proceedings of the Royal Society of London. Series A-Mathematical and Physical Sciences*, *151*(873), 465–478.

Tejpal, J., and Chaudhary, B. S. (2014). Geo-Environmental Consequences of River Sand and Stone Mining: A Case Study of Narnaul Block, Haryana. *Transactions. Journal of the Institute of Indian Geographers*, *36*(1), 218–234.

Thomas, V. G. (1985). Experimentally determined impacts of a small, suction gold dredge on a Montana stream. *North American Journal of Fisheries Management*, *5*(3B), 480–488.

Thompson, C. E. L., Amos, C. L., Jones, T. E. R., & Chaplin, J. (2003). The manifestation of fluid-transmitted bed shear stress in a smooth annular flume-a comparison of methods. *Journal of Coastal Research*, 1094–1103.

Torres, A., Brandt, J., Lear, K., & Liu, J. (2017). A looming tragedy of the sand commons. *Science*, *357*(6355), 970–971.

Turner, L. M., & Erskine, W. D. (1997). Thermal, oxygen and salt stratification in three weir pools on the Nepean River, NSW. In *Science and Technology in the Environmental Management of the Hawkesbury--Nepean Catchment*, July 10-11, University of Western Sydney, Australia (pp. 87-92).

Unger, J., & Hager, W. H. (2007). Down-flow and horseshoe vortex characteristics of sediment embedded bridge piers. *Experiments in Fluids*, *42*(1), 1–19.

Wishart, D., Warburton, J., & Bracken, L. (2008). Gravel extraction and planform change in a wandering gravel-bed river: The River Wear, Northern England. *Geomorphology*, *94*(1–2), 131–152.

Yanmaz, A. M., & Cicekdag, O. (2000). Channel Mining induced stream bed instability around bridges. In *Watershed Management and Operations Management 2000*, ASCE, June 20-24, Colorado, United States (pp. 1–8).

Yeh, K.-C., & Tung, Y.-K. (1993). Uncertainty and sensitivity analyses of pit-migration model. *Journal of Hydraulic Engineering*, *119*(2), 262–283.

Zdravkovich, M. M. (1987). The effects of interference between circular cylinders in cross flow. *Journal of Fluids and Structures*, *1*(2), 239–261.

Zeng, C., & Li, C.-W. (2014). Measurements and modeling of open-channel flows with finite semi-rigid vegetation patches. *Environmental Fluid Mechanics*, *14*(1), 113–134.